Large-Eddy Simulation of the Flat-plate Turbulent Boundary Layer at High Reynolds numbers

Thesis by

Michio Inoue

In Partial Fulfillment of the Requirements
for the Degree of
Doctor of Philosophy

California Institute of Technology
Pasadena, California

2012
(Defended 27th April 2012)

To my family

Acknowledgements

I would like to first express my deepest gratitude to my advisor, Professor Dale Pullin, who provided a chance to work on exciting and fulfilling research projects. I sincerely appreciate his incredible patience in teaching me the fundamental process of research in the computational fluid dynamics of turbulence. I am also grateful for his understanding my pursuing a minor in Applied & Computational Mathematics, which helped me expand my intellectual horizon. Being honored to be one of his students, I could not have asked for a better advisor. I also gratefully acknowledge the helpful comments and suggestions on my thesis from the members of my thesis committee, Professors Beverley McKeon, Tim Colonius, and Anthony Leonard.

I was fortunate to participate in a fruitful collaborative effort on extending the capabilities of large-eddy simulations (Chapters 4 and 5) with Professor Ivan Marusic and Dr. Romain Mathis from the University of Melbourne. I learned much from our discussions, especially the nuances of experimental research. Thanks also go to Professor Andrew Ooi, who most generously provided computational resources at the Victorian Life Sciences Computation Initiative (VLSCI), and Zambri Harun who provided experimental measurements of the adverse-pressure-gradient turbulent boundary layer (Chapter 5).

Life at Caltech was fascinating, thanks to my fellow graduate students at GALCIT and former and current members in the Allen Puckett Laboratory of Computational Fluid Dynamics; I thank Andrew, Alejandro, Geoff, Jack, Manuel, Namiko, Richard, and Yue for their friendships and many research discussions. Special thanks goes to Daniel Chung, my predecessor in the work of the wall-model large-eddy simulation, for assisting me in understanding various numerical issues, and for providing me valuable guidance for getting off on the right foot.

Last, but not the least, I am deeply indebted to my parents, Yoshiaki and Kunie Inoue for their unconditional support and trust for what I intend to pursue. I am truly blessed to have them as my parents.

This research has been supported in part by the Ministry of Education, Culture, Sports, Science, and Technology of Japan, and the National Science Foundation under grant CBET 0651754.

Abstract

The near-wall, subgrid-scale (SGS) model [Chung and Pullin, "Large-eddy simulation and wall-modeling of turbulent channel flow", J. Fluid Mech. **631**, 281–309 (2009)] is used to perform large-eddy simulations (LES) of the incompressible developing, smooth-wall, flat-plate turbulent boundary layer. In this model, the stretched-vortex, SGS closure is utilized in conjunction with a tailored, near-wall model designed to incorporate anisotropic vorticity scales in the presence of the wall. The composite SGS-wall model is presently incorporated into a computer code suitable for the LES of developing flat-plate boundary layers. This is then used to study several aspects of zero- and adverse-pressure gradient turbulent boundary layers.

First, LES of the zero-pressure gradient turbulent boundary layer are performed at Reynolds numbers Re_θ based on the free-stream velocity and the momentum thickness in the range $Re_\theta = 10^3$–10^{12}. Results include the inverse skin friction coefficient, $\sqrt{2/C_f}$, velocity profiles, the shape factor H, the Kármán "constant", and the Coles wake factor as functions of Re_θ. Comparisons with some direct numerical simulation (DNS) and experiment are made, including turbulent intensity data from atmospheric-layer measurements at $Re_\theta = \mathcal{O}(10^6)$. At extremely large Re_θ, the empirical Coles-Fernholz relation for skin-friction coefficient provides a reasonable representation of the LES predictions. While the present LES methodology cannot of itself probe the structure of the near-wall region, the present results show turbulence intensities that scale on the wall-friction velocity and on the Clauser length scale over almost all of the outer boundary layer. It is argued that the LES is suggestive of the asymptotic, infinite Reynolds-number limit for the smooth-wall turbulent boundary layer and different ways in which this limit can be approached are discussed. The maximum Re_θ of the present simulations appears to be limited by machine precision and it is speculated, but not demonstrated, that even larger Re_θ could be achieved with quad- or higher-precision arithmetic.

Second, the time series velocity signals obtained from LES within the logarithmic region of the zero-pressure gradient turbulent boundary layer are used in combination with an empirical, predictive inner–outer wall model [Marusic et al., "Predictive model for wall-bounded turbulent flow", Science **329**, 193 (2010)] to calculate the statistics of the fluctuating streamwise velocity in the inner region of the zero-pressure gradient turbulent boundary layer. Results, including spectra and moments up to fourth order, are compared with equivalent predictions using experimental time series, as well as

with direct experimental measurements at Reynolds numbers Re_τ based on the friction velocity and the boundary layer thickness, $Re_\tau = 7,300$, $13,600$ and $19,000$. LES combined with the wall model are then used to extend the inner-layer predictions to Reynolds numbers $Re_\tau = 62,000$, $100,000$ and $200,000$ that lie within a gap in $\log(Re_\tau)$ space between laboratory measurements and surface-layer, atmospheric experiments. The present results support a log-like increase in the near-wall peak of the streamwise turbulence intensities with Re_τ and also provide a means of extending LES results at large Reynolds numbers to the near-wall region of wall-bounded turbulent flows.

Finally, we apply the wall model to LES of a turbulent boundary layer subject to an adverse pressure gradient. Computed statistics are found to be consistent with recent experiments and some Reynolds number similarity is observed over a range of two orders of magnitude.

Contents

Acknowledgements **iv**

Abstract **v**

List of Figures **x**

List of Tables **xii**

1 Introduction **1**

2 A numerical code to simulate wall-bounded turbulence **4**

2.1 Background 4

2.1.1 Inflow-generating method 4

2.1.2 The order of spatial approximation 6

2.2 Problem formulation 8

2.2.1 The temporal discretization; fractional step method 9

2.2.2 The spatial discretization; fourth-order finite difference 11

2.3 The Poisson-pressure equation 12

2.4 Boundary conditions 12

2.4.1 Outflow condition 13

2.4.2 Free-stream condition 13

2.5 Parallelization 16

2.6 Code validation 18

2.6.1 Method of manufactured solution 18

2.6.2 DNS of a zero-pressure gradient turbulent boundary layer 20

2.7 Discussion 20

3 LES of the zero-pressure gradient turbulent boundary layer **21**

3.1 Background 21

3.2 Subgrid-scale model for wall-bounded flow 22

3.2.1 The stretched-vortex subgrid-scale model 22

3.2.2 The wall-shear stress 23

3.2.3 Slip velocity at a raised or “virtual” wall 24

3.2.4 PDE model for wall-shear stress 26

3.2.5 Summary of SGS wall model 26

3.3 LES of the zero-pressure gradient turbulent boundary layer 27

3.3.1 Numerical method 27

3.3.2 Range of LES performed 28

3.3.3 Effect of resolution and domain length 29

3.3.4 Skin friction and H-factor 30

3.3.5 Mean velocity profiles and flow visualization 35

3.3.6 Kármán “constant” and the Coles wake-factor 36

3.3.7 Turbulence intensity profiles 38

3.4 Discussion 40

4 Inner-layer predictions for the flat-plate turbulent boundary layer combining a predictive wall-model with LES 46

4.1 Background 46

4.2 Wall-model description 48

4.2.1 Predictive inner–outer model 49

4.3 Simulation details 49

4.3.1 LES performed 51

4.3.2 Skin friction and mean velocity profiles 51

4.4 Results at intermediate Reynolds numbers 54

4.4.1 Streamwise turbulent intensity 54

4.4.2 Longitudinal spectra of streamwise velocity 58

4.4.3 Signal length and resolution effects 58

4.5 Results at larger Reynolds number 59

4.5.1 Turbulence intensity and spectra 59

4.5.2 Higher-order statistics 63

5 LES of the adverse-pressure gradient turbulent boundary layer 65

5.1 Background 65

5.2 Problem setting 67

5.3 LES performed 68

5.4 Results and discussion 69

5.4.1 APG parameters 70

5.4.2 Mean velocity profiles . . . 73
5.4.3 S-factors . . . 75
5.4.4 Turbulence intensities . . . 76

6 Conclusions **79**
6.1 LES of the zero-pressure gradient turbulent boundary layer . . . 79
6.2 Inner-layer predictions for the flat-plate turbulent boundary layer combining a predictive wall-model with LES . . . 80
6.3 LES of the adverse-pressure gradient turbulent boundary layer . . . 81

A Numerical Details **83**
A.1 SGS model implementation . . . 83
A.2 Morinishi's schemes . . . 83
A.3 Staggered-grid system in two directions and FFT in the other . . . 85
A.4 Discrete conservations and boundary conditions for the channel flow case . . . 86
A.4.1 Discrete conservation of mass . . . 87
A.4.1.1 Second-order-accurate scheme . . . 87
A.4.1.2 Fourth-order-accurate scheme . . . 87
A.4.2 Discrete conservation of momentum . . . 88
A.4.2.1 Second-order-accurate scheme . . . 88
A.4.2.2 Fourth-order-accurate scheme . . . 89
A.4.3 Other conditions for fourth-order-accurate schemes . . . 90
A.5 Helmholtz solver using discrete Fourier cosine transform . . . 92
A.5.1 Second-order-accurate scheme . . . 93
A.5.2 Fourth-order-accurate scheme . . . 94

B Parallelization; scaling performance **95**
B.1 Poisson-pressure solver . . . 95
B.1.1 Observations . . . 96
B.2 Navier-Stokes solver . . . 97
B.2.1 LES case . . . 97
B.2.2 DNS case . . . 97

Bibliography **103**

List of Figures

2.1 A schematic of the computational domains of Code-A and Code-B 6

2.2 A schematic of the computational Code-A domain showing the recycling region 7

2.3 The staggered-grid configuration 11

2.4 Parallelization scheme to distribute memory and computation 17

2.5 The order of convergence of the scheme 19

2.6 Comparison of present results with DNS 20

3.1 (a): U_e^+ versus Re_θ and Coles-Fernholz 2, (b): Mean streamwise velocity at $Re_\theta \approx 2.5 \times 10^4$ 31

3.2 (a): Streamwise, spanwise, and wall-normal intensities, (b): Reynolds shear stresses at $Re_\theta \approx 2.5 \times 10^4$ using three resolutions 32

3.3 $U_e^+ \equiv U_\infty/u_\tau$ versus Re_θ up to $Re_\theta \approx 10^5$ 33

3.4 $U_e^+ \equiv U_\infty/u_\tau$ versus Re_θ up to $Re_\theta \approx 10^{12}$ 33

3.5 $U_e^+ \equiv U_\infty/u_\tau$ versus Re_θ with longer streamwise domains 34

3.6 Shape factor versus Re_θ 36

3.7 Mean velocity profiles over a range of Re_θ 37

3.8 Mean velocity defect profiles over a range of Re_θ 38

3.9 Contour plot of instantaneous streamwise velocity. Effect of x_{ref} position, domain size and inflow generation method 39

3.10 Contour plot of instantaneous streamwise velocity. Effect of resolution 39

3.11 Contour plot of instantaneous streamwise velocity. Effect of Reynolds number 40

3.12 Contour plot of instantaneous velocity defect 41

3.13 (a): Kármán “constant” calculated dynamically, (b): Coles wake factor 41

3.14 Coles wake factor with experiments 42

3.15 Streamwise velocity fluctuation. (a): Outer scaling, (b): Mixed scaling 42

3.16 Streamwise and wall-normal velocity fluctuations in inner scaling 42

3.17 Streamwise root-mean square fluctuation at $Re_\tau \approx 10^6$ compared to SLTEST data . . 43

4.1 Schematic description of two “wall models” 48

4.2 Reynolds number dependency of the S-factor for cases 7.3k-θ, 13.6k-θ, and 19k-θH . . 52

4.3 Mean velocity profiles for cases 7.3k-θ, 13.6k-θ, 19k-θH, 62k-τ, 100k-τ, and 200k-τ . . 53

4.4 Prediction of predictions of streamwise turbulence intensity for cases (a) 7k-θ; (b) 13.6k-θ; (c) 19k-θH . . . 55

4.5 Premultiplied energy spectra of the streamwise velocity fluctuations at $z_O^+ \simeq \sqrt{15 Re_\tau}$ 56

4.6 Predicted premultiplied energy spectra map . . . 57

4.7 Example of predicted pre-multiplied energy spectra the streamwise velocity fluctuations at the inner-peak location . . . 57

4.8 The effect of resolution in LES-PIO predictions of streamwise turbulence intensity . . 59

4.9 Prediction of streamwise turbulence intensity for cases 62k-τ, 100k-τ, and 200k-τ. . . 60

4.10 Reynolds number dependency of the inner-peak intensity . . . 60

4.11 Prediction of streamwise turbulence intensity $\overline{u'^2}/u_\tau^2$ corrected to a hypothetical infinitesimally small sensor . . . 61

4.12 Reynolds number evolution of the predicted premultiplied energy spectra at the inner-peak location . . . 61

4.13 Reynolds number dependency of predicted skewness and kurtosis . . . 63

4.14 Skewness $\overline{u'^3}/(\overline{u'^2})^{3/2}$ and kurtosis $\overline{u'^4}/(\overline{u'^2})^2$ profile . . . 64

5.1 Profile of coefficient of pressure C_p . . . 67

5.2 Profile of coefficient of pressure C_p and the pressure gradient dp/dx . . . 70

5.3 LES results; β, K, and $(dp/dx)^+$ . . . 71

5.4 LES results; case D1 and corresponding experimental measurements of the mean velocity 73

5.5 LES results; mean velocity from case D1, D3, D5 . . . 74

5.6 LES results; mean velocity defect profiles from case D1, D2, D3, D4, and D5 . . . 74

5.7 LES results; $S(Re_\tau)$ . . . 75

5.8 LES results; $S(\beta) - S(\beta = 0)$ . . . 76

5.9 LES results; case D1 and corresponding experimental measurements of the streamwise turbulence intensity . . . 77

5.10 LES results; streamwise turbulence intensity and Reynolds shear stress from case D1, D2, D3, D4, and D5 . . . 78

A.1 Staggered-grid formulation for the subgrid-scale model . . . 84

A.2 The ghost-cell values for the fourth-order scheme . . . 86

List of Tables

2.1 Numerical methods in the simulation code 11

2.2 Convergence test run on both second- and fourth-order-accurate scheme 19

3.1 Simulation parameters 30

3.2 Effect of resolution at $Re_\theta \approx 2.5 \times 10^5$ 31

3.3 Effect of domain size and the location of the recycling plane at $Re_\theta \approx 2.5 \times 10^4$ 31

4.1 Simulation parameters and integral quantities 50

4.2 Reynolds number and S-factor for each LES and corresponding experiments 50

5.1 Experimental parameters for APGTBL 68

5.2 Simulation parameters for APGTBL 69

5.3 LES results; case D1, D3, and D5 72

5.4 LES results; case D1 and corresponding experimental parameters 72

B.1 The number of grid points in each direction. Case 1: $\mathbf{A}$ is 384×384 matrix. Case 2: $\mathbf{A}$ is 1024×1024 matrix 96

B.2 Computational time required to solve $\mathbf{Ax} = \mathbf{b}$ 96

B.3 Scaling test of Navier-Stokes solver, the number of grid points in each direction 97

B.4 Computational time required (seconds) at each stage. LES $384 \times 128 \times 64$ 98

B.5 Computational time required (percentile) at each stage. LES $384 \times 128 \times 64$ 99

B.6 Computational time required (seconds) at each stage. DNS case 256^3 100

B.7 Computational time required (percentile) at each stage. DNS case 256^3 101

B.8 Computational time required (seconds) at the slowest process and the fastest process. DNS case 256^3 102

Chapter 1

Introduction

Numerical resolution requirements limit applicability of direct numerical simulation (DNS) to turbulent flows at low-to-moderate Reynolds numbers. In DNS of incompressible flows, a wide range of dynamically important scales of motion must be resolved, including the smallest dissipative Kolmogorov scales. Large-eddy simulation (LES) is now a viable alternative to DNS and experiment (Jiménez 2003). Here, only the large scales of motion are resolved while the effects of small unresolved eddies are modeled; this enterprise is referred to as subgrid-scale modeling. In LES, this takes the form of closures for the subgrid contributions to the fluxes of momentum, energy and scalar transport insofar as these appear in the LES equations for the resolved scales. LES has had a significant impact on the development of turbulence prediction techniques, and many different approaches have been developed; see Lesieur and Metais (1996), Meneveau and Katz (2000), Sagaut (2006) for reviews.

The LES of wall-bounded flow at both laboratory and atmospheric-layer Reynolds numbers remains a significant challenge (e.g., Cabot and Moin 2000, Wang and Moin 2002, Piomelli and Balaras 2002, Templeton et al. 2005, Piomelli 2008) because close to the wall the paradigm of flow dominance by large scales fails (Pope 2004). Near wall motions are highly anisotropic and their spatial extent and structure are determined by complex near-wall dynamics conditioned by streamwise vortices streaks and possibly other structures. These scales probably dominate the transport dynamics but will tend to be underresolved at moderate grid resolution and large Re_θ. One approach is near-wall resolved LES where the LES grid extends into the viscous layer providing partial resolution of the viscous wall length in at least the wall-normal direction, while LES operates in the outer part of the boundary layer. This has been shown to work well at moderate Reynolds numbers (Schlatter et al. 2010) but the cost scales approximately as Reynolds number to the power 1.8 (see Pope 2000) which may limit application at large Re_θ. An alternative is near-wall modeling which attempts to eliminate the near-wall layer from the overall LES (Piomelli 2008). Some means is then required first, of providing boundary conditions for the LES that replace the usual no-slip condition used for the Navier-Stokes equations, and second, of accurately determining the wall shear stress, or equivalently, the wall friction velocity at the bottom of a region that is not resolved.

Wall modeling has also been used for LES of the atmospheric boundary layer using so-called "wall-stress boundary conditions" that relate a wall shear stress, sometimes determined from an assumed log law, to the velocity at the first grid point from the wall (Porté-Agel et al. 2000, Anderson and Meneveau 2011, Lu and Porté-Agel 2010). Wall-stress models appear in a variety of implementations, and since the present wall-model is not of this type, the reader is referred to a review (Piomelli 2008) for technical details. Using a specified wall roughness scale, these methods provide LES for effective rough-wall flow at nominally large but undetermined Reynolds numbers.

Wall-models based on either a table look-up using a universal mean-velocity profile to determine the friction velocity (Templeton et al. 2005) or on a wall-boundary condition using optimal control theory coupled to a Reynolds-averaged Navier-Stokes model (Templeton et al. 2008) have enabled LES of streamwise periodic, smooth-wall channel flow up to $Re_\tau = \mathcal{O}(10^4)$. These atmospheric and smooth-wall channel-flow LES provide reasonable representations of the mean log-like velocity profile at either unknown or at moderately large Reynolds number but do not appear to have yet been used to systematically study the spatially-developing, zero-pressure gradient boundary layer at either large laboratory Reynolds numbers (Österlund 1999, DeGraaff and Eaton 2000, Mathis et al. 2009) or at extreme Reynolds numbers typical of field experiments in the atmospheric surface layer (Metzger et al. 2007). Such LES must dynamically calculate the streamwise varying skin-friction velocity in relation to the free-stream velocity, while using a wall-model enabling resolution of quantities that may exhibit weak but definite Reynolds number dependence or perhaps Reynolds number independence. For smooth-wall flow examples of the former are the streamwise velocity-profile shape factor and the skin-friction coefficient while examples of the latter are the Coles wake factor and possibly the Kármán constant. This is a regime that, to date, has proven inaccessible to direct numerical simulation. It is the main focus of the present work.

Chung and Pullin (2009) developed an subgrid-scale (SGS) model tailored to smooth wall-bounded flow by attempting to incorporate widely accepted elements of near-wall vortices into a structure-based wall-model. Their approach begins by averaging the streamwise momentum equation over a thin layer adjacent to the wall. Using inner scaling for the unsteady term of the averaged equation while coupling other terms to the outer LES, they obtained an ordinary differential equation (ODE) for the local wall-normal velocity gradient, or equivalently, the wall-friction velocity. This is solved as an auxiliary equation for the main, outer flow LES and provides a direct calculation of the friction velocity. The boundary condition for the outer LES is applied at a raised or "virtual wall" by integrating, in the the wall-normal direction, the stretched-vortex SGS model expression for the wall-normal transport of streamwise momentum, under an assumption that there exists, in the near-wall layer, a hierarchy of streamwise vortices whose size scales with distance from the wall (see Nickels et al. 2007). This gives a log-like relation for the mean streamwise velocity that, in conjunction with the wall friction velocity obtained from the wall-layer ODE, provides a slip velocity for the outer LES. The model also gives a means of determining a Kármán-like constant dynamically. Chung and Pullin (2009) applied the model to LES of channel flow up to $Re_\tau = 2\times10^7$, while Chung and McKeon (2010) performed LES of large-scale structures in turbulent flow in long channels. Presently this model is extended to the LES of the flat-plate turbulent boundary layer under zero- and adverse-pressure gradient.

In Chapter 2, a computer code for the numerical method simulating spatially developing turbulent boundary layer flows is described. This is followed in Chapter 3 by the LES of the zero-pressure gradient, flat-plate turbulent boundary layer (ZPGFPTBL). The present wall model does not resolve the near wall region. In Chapter 4 we combine the present LES with an empirical inner–outer wall model which enables extension of the LES to the inner region of the turbulent boundary layer. The near wall statistics of the fluctuating streamwise velocity of ZPGFPTBL at up to $Re_\tau = 200,000$ are presented. Finally, we provide an application of the SGS wall model on the LES of the adverse-pressure gradient, flat-plate turbulent boundary layer in Chapter 5 before concluding in Chapter 6.

Chapter 2

A numerical code to simulate wall-bounded turbulence

2.1 Background

The DNS studies have addressed several important issues for the numerical simulation of the TBL including high-order nonspectral methods and boundary conditions suitable for spatially developing flows with only one, as opposed to two, homogeneous directions. Due to the additional inhomogeneity in the streamwise direction, progress in the DNS of turbulent boundary layers has been slower, in terms of the Reynolds numbers achieved, compared to the various numerical computations of canonical turbulent flows performed to date. In the case of the transitional flow whose state is laminar in the inflow region, the inflow velocity conditions can be specified relatively easily, but the computational domain needs to be sufficiently long to develop the flow into turbulence. To avoid using an exceeding long domain that includes full transition, it is necessary to provide inflow conditions with realistic turbulence properties at each time step of the simulation. The velocities specified at the inflow should represent the contribution of energy-containing eddies as reviewed by Keating et al. (2004). Previous works can be assessed on the basis of their methods designed to tackle this inflow issue. Readers are referred to Keating et al. (2004) for a brief history review of generating inflow conditions. For the purpose of completeness, a review is also provided here.

2.1.1 Inflow-generating method

An early approach to simulating spatially developing turbulent flows was to utilize modifications of the streamwise periodic conditions used to supply inflow conditions for streamwise periodic flows, so that a full Fourier pseudospectral method would be still applicable. Spalart (1988) proposed a systematic multiple-scale procedure to approximate the local effects of the streamwise growth of the flow (e.g., boundary layer thickness). This enabled transformation of the system of equations into a selfsimilar coordinate frame, in which the flow was periodic. Using streamwise periodicity, Spalart (1988) performed DNS of flat-plate boundary layers providing valuable data at Re_θ up to 1410. The main disadvantage, however, is the need to evaluate the growth terms that are numerous and complicated in form. Also, since such similarity does not always occur (Keating et al. 2004), the modification was made by adding the so-called fringe region downstream of the physical domain, where the boundary layer thickness is decreased and re-introduced as an inflow, that is, the periodic boundary condition, Fourier spectral method was used in the streamwise direction. The key assumption is that the nonphysical phenomena occurring in the fringe region do not invalidate the solution in the other, nonfringe, region. Detailed analysis and discussion on the fringe-region technique can be found in Nordström et al. (1999). A possible disadvantage is that, since the flow is forced back to a laminar state within the fringe region, then it requires a relatively long computational domain to achieve high-Reynolds-numbers flow. A further problem is that periodicity is difficult to reconcile with strong spatial inhomogeneity, such as strong pressure gradients, or with control strategies involving net mass injection (Simens et al. 2009). This fringe method is actively in use: the most recent published work is Schlatter et al. (2009). They conducted DNS of turbulent boundary layer up to $Re_\theta = 2500$ and showed excellent agreement in skin friction, mean velocity and turbulent fluctuations with experiments (Schlatter et al. 2009).

With the loss of one homogeneous direction, for developing boundary layer flow, Lund et al. (1998) (LWS) proposed a modification to Spalart's approach using a rescaling method, eliminating the need for the growth-terms by a more simple and flexible rescaling technique. Here the inflow velocity is generated in a first simulation (code-A) and used in second, TBL simulation (code-B). Code-A generates its own inflow conditions by rescaling the instantaneous velocity data of a downstream recycling plane, which are then reintroduced at the inlet; see Figure 2.1 styled after Ferrante and Elghobashi (2004). It rescales the inner and outer layers of the velocity profile separately to account for the different similarity laws observed. Inflow conditions for Code-B can then be taken directly from an interior plane of the code-A simulation. This method was successfully used in LES on a spatially developing boundary layer of $Re_\theta = 1530$ to 2150 (Lund et al. 1998).

Ferrante and Elghobashi (2004) were, however, unable to obtain a satisfactory development of the turbulent velocity correlations in DNS. Thus they proposed a more robust variant of the LWS method by introducing a set of additional steps before the rescaling process. These steps involves carefully prescribing both the Reynolds stress tensor and the energy spectra when initializing the flow field of Code-A, whereas in the original LWS method, only the mean streamwise velocity was prescribed and a random fluctuation added. This step successfully provides non-vanishing magnitude of a statistical correlation between the streamwise and wall-normal velocity fluctuation, thus sustaining the production rate of turbulence kinetic energy. They performed DNS with $Re_\theta = 800$–1430.

Inflow generating methodology remains an area of active research, (e.g., Simens et al. 2009, Keating et al. 2004, Liu and Pletcher 2006, Jewkes et al. 2011, Araya et al. 2011) and we will subsequently refer to "code-A only" and "code-A&B" methods. Simens et al. (2009) advocate a code-A only method (no code B) restricting the rescaling region to some fraction of the total streamwise domain; see Figure 2.2 styled after Simens et al. (2009).

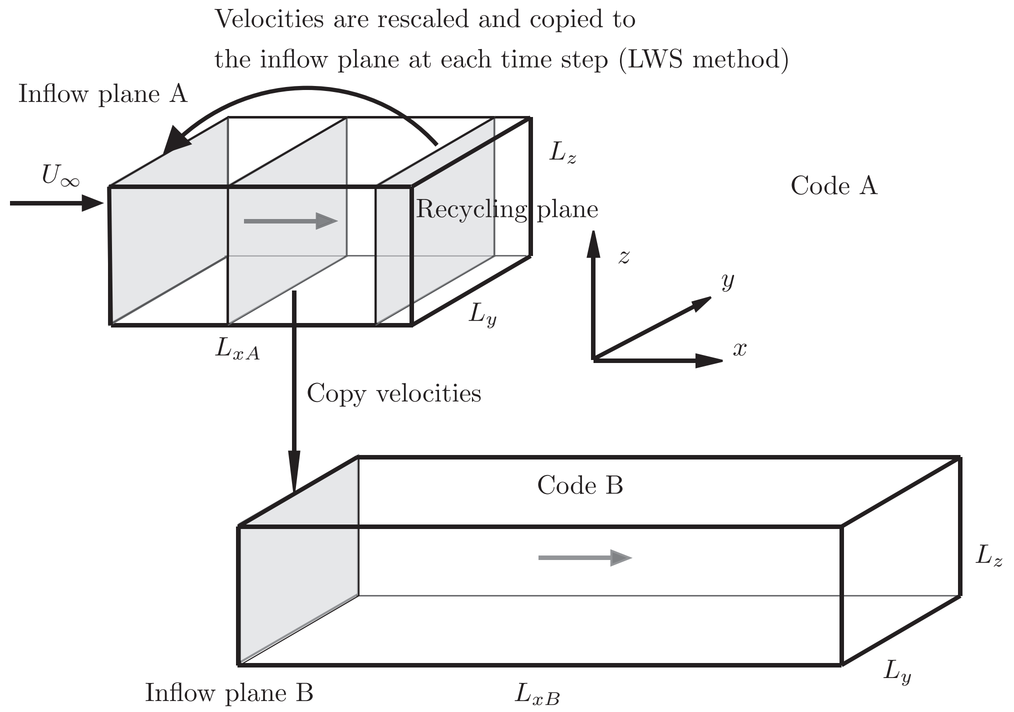

Figure 2.1. A schematic of the computational domains of Code-A and Code-B used by Lund et al. (1998) and Ferrante and Elghobashi (2004)

2.1.2 The order of spatial approximation

Although the fringe method is attractive with respect to the spectral accuracy, considering the possible disadvantages and somewhat artificial assumptions mentioned above, it is preferable to use numerical methods that can accommodate streamwise development of the boundary layer and, for this purpose, finite-difference schemes have been used by various authors (e.g., Lund et al. 1998, Ferrante and Elghobashi 2004, Simens et al. 2009, Wu and Moin 2009, Lee and Sung 2011). Except for Simens et al. (2009), the studies cited above use finite-difference schemes that are second-order central difference. Although they conserve mass, momentum and energy, their resolution properties are relatively poor. The use of a higher-order stencil is essential to limit the resources and required time for computation. Also a high-order scheme is recommended for LES owing to the interference of discretization errors with the SGS model terms (Chow and Moin 2003, Gullbrand and Chow 2003).

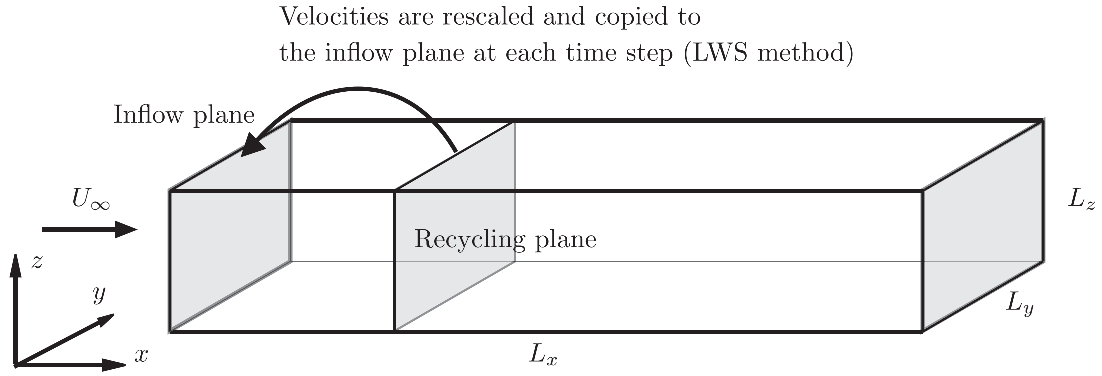

Figure 2.2. A schematic of the computational Code-A domain showing the recycling region

Fourth- or higher-order schemes have been proposed and implemented for wall-bounded flow (e.g., Knikker 2009, Boersma 2011) using a staggered-grid, compact finite-difference method. Solving the resulted discretized Poisson-pressure equations, however, is not straightforward (if not impossible) with the direct method. Also this usually requires iterative methods which need relatively longer CPU time to compute compared to a direct method. The amount of CPU time strongly depends on the required tolerance which should be at least the order of $\mathcal{O}(10^{-10})$ (Knikker 2009), otherwise the error will likely accumulate over time and will degrade the overall convergence. This has been the major obstacle to achieving a higher-order scheme. Thus to avoid a system of equations that cannot be solved by an efficient direct method, Simens et al. (2009) and Knikker (2009) mixed a second-order formulation for the pressure projection scheme with fourth or higher-order compact finite-difference schemes for approximating velocities derivatives in a fractional-step context. Their scheme is formally second-order and it shows second-order spatial convergence. The major advantage of using compact finite-difference schemes is that they require narrow stencils. Their high-resolution code, however, has issues when applied in our situation. For example, the compact finite-difference schemes do not conserve energy in the inviscid limit when solving the Navier-Stokes equation, which is not desirable for LES because it may lead to numerical instabilities (Kim and Moin 1985) when not all energy-containing scales are resolved.

Our choice is the following: A fully conservative fourth-order finite-difference scheme in two inhomogeneous directions and a pseudospectral method in the other direction with boundary treatments presented by Morinishi et al. (1998). This includes a small modification that leads to Poisson-pressure equations that are solvable by efficient direct methods, keeping the overall accuracy of fourth-order. This scheme was successfully implemented and shows a fourth-order of accuracy in convergence tests for both pressure and velocities. The fractional step, or time splitting, method is implemented for time advancement, a scheme where a third-order Runge-Kutta schemes is used for terms treated explicitly and a second-order Crank-Nicolson scheme for terms treated implicitly

(Spalart et al. 1991).

In this chapter, §2.2 describes the fractional-step method and the spatial discretization to solve the incompressible Navier-Stokes equations. Then, the resulting Poisson-pressure equations and their related issues are outlined in §2.3 with some details contained in Appendix A. Some discussion is given regarding the boundary conditions appropriate for boundary-layer simulation and the arrangement of parallel algorithm in §2.4 and §2.5. The discussion and summary concludes this chapter after verification of the code in §2.6.

2.2 Problem formulation

The incompressible Navier-Stokes equations in primitive variables are given by

$$\frac{\partial \mathbf{u}}{\partial t} + \mathbf{u} \cdot \nabla \mathbf{u} = -\nabla p + \frac{1}{Re} \nabla^2 \mathbf{u}, \tag{2.1}$$

$$\nabla \cdot \mathbf{u} = 0. \tag{2.2}$$

For illustrating the principal idea simply, the implicit Crank-Nicolson scheme is used for linear (viscous) terms, and second-order Adams-Bashforth scheme for nonlinear terms. The discrete form of the above equation can be written as

$$\frac{\mathbf{u}^{n+1} - \mathbf{u}^n}{\mathrm{dt}} = -\mathbf{G}p - \left(\frac{3}{2} \mathbf{N}\mathbf{u}^n - \frac{1}{2} \mathbf{N}\mathbf{u}^{n-1} \right) + \frac{1}{2Re} \left(\mathbf{L}\mathbf{u}^{n+1} + bc_1^{n+1} + \mathbf{L}\mathbf{u}^n + bc_1^n \right), \tag{2.3}$$

$$D\mathbf{u}^{n+1} = bc_2^{n+1}, \tag{2.4}$$

or in the matrix form, as

$$\begin{bmatrix} \mathbf{A} & \mathrm{dt}\mathbf{G} \\ \mathbf{D} & \mathbf{0} \end{bmatrix} \begin{bmatrix} \mathbf{u}^{n+1} \\ p \end{bmatrix} = \begin{bmatrix} \mathbf{r}^n \\ \mathbf{0} \end{bmatrix} + \begin{bmatrix} bc_1 \\ bc_2 \end{bmatrix}, \tag{2.5}$$

where $\mathbf{A}$ is the implicit operator for the advection-diffusion part of the momentum equation, $\mathbf{N}$ is the convective operator, $\mathbf{G}$ is the gradient operator, $\mathbf{D}$ is the divergence operator, $\mathbf{r}^n$ is the explicit right-hand side of the momentum equation, bc_1 is the boundary condition vector for the momentum equation and bc_2 is the boundary condition vector for the incompressibility constraint. Only the viscous term is treated implicitly here so that

$$\mathbf{A} = \mathbf{I} - \frac{\mathrm{dt}}{2Re} \mathbf{L}, \tag{2.6}$$

$$\mathbf{r^n} = \mathrm{dt}\left[\frac{3}{2}\mathbf{N}\mathbf{u}^n - \frac{1}{2}\mathbf{N}\mathbf{u}^{n-1} + \frac{1}{2}(bc_1^{n+1} + \mathbf{L}\mathbf{u}^n + bc_1^n)\right]. \tag{2.7}$$

2.2.1 The temporal discretization; fractional step method

First introduced by Chorin (1968), the fractional step, or time-splitting, method solves the unsteady Navier-Stokes equations in a segregated manner. At each time step, an incomplete form of the momentum equations integrated to obtain an approximate velocity field, which is in general not divergence free. Then, the velocity field is projected into the divergence-free field without changing its vorticity. This projection step is achieved by solving the Poisson equation for "pressure", which is not a thermodynamic variable but a Lagrange multiplier that constrains the velocity field to be divergence-free (Gresho and Sani 1987). As mentioned by Perot (1993), the fractional step method has been used in the past by numerous researchers. In general it is first-order accurate in time and there still exits some controversy and/or disagreement concerning boundary conditions and the details of implementation of the method (Kim and Moin 1985). Also, considerable effort has been spent to achieve higher-order accuracy in time integration (e.g., Gresho and Sani 1987, Armfield and Street 1999, Brown et al. 2001, Sani et al. 2006). On the one hand, the first-order behavior is attributed to the use of the physical velocity boundary condition and zero-normal-pressure gradient, and several modification on boundary conditions have been presented. On the other hand, the first-order accuracy is also claimed to be due to the commutation error shown by the LU factorization scheme (Perot 1993). Perot suggested that no boundary condition is required for obtaining the intermediate velocity and pressure.

The fractional step method is related to the block LU factorization of equation (2.5) in the form

$$\begin{bmatrix} \mathbf{A} & \mathbf{0} \\ \mathbf{D} & -\mathrm{dt}\mathbf{D}\mathbf{A}^{-1}\mathbf{G} \end{bmatrix} \begin{bmatrix} \mathbf{I} & \mathrm{dt}\mathbf{A}^{-1}\mathbf{G} \\ \mathbf{0} & \mathbf{I} \end{bmatrix} \begin{bmatrix} \mathbf{u}^{n+1} \\ p \end{bmatrix} = \begin{bmatrix} \mathbf{r}^n \\ \mathbf{0} \end{bmatrix} + \begin{bmatrix} bc_1 \\ bc_2 \end{bmatrix}. \tag{2.8}$$

Equation (2.8) is called the Uzawa method, which is exact but computationally very expensive since calculating the inverse of $\mathbf{A}$ is not practical. Hence equation (2.8) is usually solved approximating $\mathbf{A}^{-1}$. Different approximations to the inverse result in different classes of fractional step method. The classic fractional step method corresponds to using $\mathbf{A}^{-1} = \mathbf{I} + \mathcal{O}(\mathrm{dt})$, which results in a first-order error term. By choosing $\mathbf{A}^{-1} = \mathbf{I} + \frac{\mathrm{dt}}{2Re}\mathbf{L} + \mathcal{O}(\mathrm{dt}^2)$, the resulting error is $\mathcal{O}(\mathrm{dt}^2)$. In the case of $\mathbf{A}^{-1} = \mathbf{I}$, the single time step reduces to the following sequence of operations,

$$\mathbf{A}\mathbf{u}* = \mathbf{r}^n + bc_1, \tag{2.9}$$

$$\mathrm{dt}\mathbf{D}\mathbf{G}p = (\mathbf{D}\mathbf{u}* + bc_2), \tag{2.10}$$

$$\mathbf{u}^{n+1} = \mathbf{u}* - \mathrm{dt}\mathbf{G}p. \tag{2.11}$$

In the actual computation, the low-storage third-order semi-implicit Runge–Kutta method of Spalart et al. (1991) is used for temporal discretization to achieve higher order of temporal accuracy. The equations to be solved at each step then become

$$
\begin{aligned}
\mathbf{A}\mathbf{u}*^{n+1} &= \mathbf{r}^n + \beta_n bc_1, && (2.12)\\
\mathrm{dt}\,(\alpha_n+\beta_n)\,\mathbf{D}\mathbf{G}p &= \left(\mathbf{D}\mathbf{u}*^{n+1} + bc_2\right), && (2.13)\\
\mathbf{u}^{n+1} &= \mathbf{u}*^{n+1} - \mathrm{dt}\,(\alpha_n+\beta_n)\,\mathbf{G}p, && (2.14)
\end{aligned}
$$

where

$$
\mathbf{A} = \mathbf{I} - \frac{\beta_n \mathrm{dt}}{Re}\mathbf{L}, \tag{2.15}
$$

$$
\mathbf{r^n} = \mathrm{dt}\left[-\gamma_n \mathbf{N}\mathbf{u}^n - \zeta_n \mathbf{N}\mathbf{u}^{n-1} + \alpha_n\left(\mathbf{L}\mathbf{u}^n + bc_1^n\right)\right], \tag{2.16}
$$

for $n = 0, 1, 2$. For an arbitrary reference time, t_0, $\mathbf{u}^{(3)} = \mathbf{u}(t_0 + \mathrm{dt})$. The value of the constants α_n, β_n, γ_n and ζ_n are given in Spalart et al. (1991),

$$
\begin{array}{lll}
\alpha_1 = 4/15, & \alpha_2 = 1/15, & \alpha_3 = 1/6,\\
\beta_1 = 4/15, & \beta_2 = 1/15, & \beta_3 = 1/6,\\
\gamma_1 = 8/15, & \gamma_2 = 5/12, & \gamma_3 = 3/4,\\
\zeta_1 = 0, & \zeta_2 = -17/60, & \zeta_3 = -5/12.
\end{array} \tag{2.17}
$$

The implicit treatment of the viscous term allows large time steps to be taken in general, but in the context of a finite-difference method, it adds numerical complexity. It was shown in Simens (2008) (also see Akselvoll and Moin 1996), that the viscous time-step requirement can be more severe than the convective restriction only in the wall-normal direction in the case of a stretched grid that is usually employed in wall-bounded turbulence to resolve small-scale phenomena close to the wall. Although it may not be necessary to treat the viscous term implicitly (represented by the operator $\mathbf{L}$) at all for the purpose of our LES (using even-spaced grids in general), nevertheless the viscous terms in the wall-normal direction are treated implicitly presently in order for the code to be robust enough to deal with DNS of turbulent boundary layer flow. The nonlinear and wall-parallel viscous terms are treated explicitly (represented by the operator $\mathbf{N}$). The time-step size dt is determined by setting the CFL number

$$
\mathrm{dt}\max\left(\frac{|u|}{\Delta x}, \frac{|v|}{\Delta y}, \frac{|w|}{\Delta z}\right), \tag{2.18}
$$

to unity. In the following, see Table 2.1 for a summary of schemes. The spatial discretization schemes are discussed next.

Item		Contents
The equation system		Incompressible Navier-Stokes equation
Discretization	Streamwise (x)	fourth-order staggered FDM
	Spanwise (y)	Fourier spectral method
	Wall-normal (z)	fourth-order staggered FDM
Time integration		Semiimplicit three-step Runge-Kutta

Table 2.1. Numerical methods in the simulation code

2.2.2 The spatial discretization; fourth-order finite difference

A fourth-order numerical code has been implemented for LES (and some DNS) on a turbulent boundary layer flow. The governing equations are solved in a box with dimensions $L_x \times L_y \times L_z$, with periodic boundary condition in the spanwise or y-direction. The components of the velocity vector $\mathbf{u}$ are u, v and w in the streamwise (x-), spanwise (y-), and wall-normal (z-) directions, respectively.

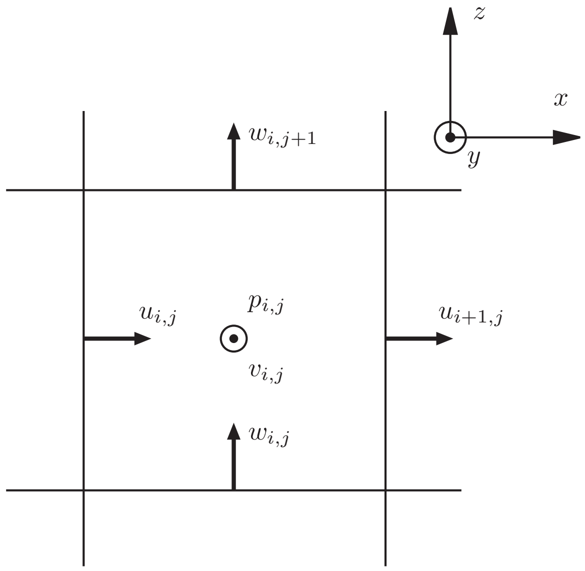

Figure 2.3. The staggered-grid configuration. The streamwise and wall-normal velocity component are stored on the cell faces and the spanwise velocity and pressure quantities at the cell center.

In our code the streamwise and wall-normal velocities are defined at the edge of each cell and spanwise velocity and the pressure are at the center. The staggered-grid cell configuration is sketched in Figure 2.3. Explicit, fourth-order finite differences on a staggered grid are used to approximate (x, z)-derivatives, while a pseudospectral method is utilized for y-derivatives. The convective terms are calculated using a fully conservative skew-symmetric form (Morinishi et al. 1998). Nonlinear terms are treated using a pseudospectral method with a p_1th-order Fourier exponential filter in

y-direction, which mimics the 2/3 rule, in order to prevent aliasing errors (Gottlieb and Shu 1997, Chung and Pullin 2009). At boundaries, a ghost-point scheme is employed where points are extended beyond boundaries so that a consistent stencil can be used as in the interior. This is, in effect, equivalent to a one-sided, finite-difference scheme at wall boundaries. Values at ghost points are designed to ensure global conservation of mass and momentum. The formulation in part follows Morinishi et al. (1998), which describes the scheme for the case of channel flow with solid walls. The generalization of scheme to the arbitrary Dirichlet velocity boundary conditions can be readily be made. For the detail formulation see Appendix A.

2.3 The Poisson-pressure equation

The Poisson-pressure equation (2.13), which reduces to a set of 2D Helmholtz equations owing to the Fourier expansion in the spanwise (y-) direction, is then expanded using a cosine transform in the streamwise (x-) direction. Then the problem reduces to a series of one-dimensional Helmholtz equations along the wall-normal (z-) direction, with a modified wavenumber for each cosine representing the finite-difference stencils in x. The septa-diagonal matrix solver (available from LAPACK) is used to solve the equations in the z-direction. This leads to efficient code parallelization (see the following §2.5 for details). FFTW libraries are utilized here. It has been reported in Simens et al. (2009) that "the Gibb's errors due to the implicit derivative discontinuities at the nonperiodic end points are of order Δx^2" and that "higher-order schemes in nonperiodic domains cannot be treated in this (be expanded in cosines series) way, because they require boundary schemes with different modified wave numbers than the interior operator". This is due to how the discrete cosine transform is performed. For example, in the case of FFTW libraries, the original array of data (say, {12345}) will be expanded in such a way that the extended array has an even symmetry (say, {1234554321}) and periodicity. Now because of the even symmetry, in performing the discrete Fourier transform, the sine terms all cancel and only the cosine terms remain. In prescribing the ghost-point values for the pressure, one needs to be careful to design the scheme so that the matrix to be solved should have boundary schemes that give the same modified wave number throughout the domain including the boundary, i.e., the data is even around the boundaries. Using the concept of the modified wave number, the incompressibility can be enforced up to the machine accuracy. See Appendix A.5 for details on the Helmholtz solver using discrete Fourier transform.

2.4 Boundary conditions

The boundary condition in the y-direction is periodic and it is required to specify boundary conditions at four other boundaries to solve the system of equations (2.12) to (2.14), namely inflow, outflow, bottom wall and in the free-stream in the context of boundary layer flow simulation. As discussed in §2.1.1, the inflow condition is specified by using the recycling method of Lund et al. (1998) for the fully-developed turbulent case or by using the Blasius profile for laminar or for transitional boundary layers. The convective boundary condition at the outflow plane has been the popular choice among researchers. In this section various types of free-stream boundary condition are discussed followed by the short description of the convective boundary condition.

2.4.1 Outflow condition

The velocities at the outflow are estimated by a convective boundary condition,

$$\frac{\partial \mathbf{u}}{\partial t} + U_c(z)\frac{\partial \mathbf{u}}{\partial x} = 0, \tag{2.19}$$

where $U_c(z)$ is the local mean streamwise velocity at the exit. Depending on a choice of free-stream boundary condition, small corrections to streamwise velocity might be required to ensure global mass conservation. See the following section regarding this issue.

2.4.2 Free-stream condition

In most past studies of ZPGTBL simulations, the desired pressure gradient is obtained through prescribing velocity at the top-boundary. Specification of boundary conditions at the top of the domain is not a trivial issue. That is because it is not known, in advance, which velocity boundary conditions would lead to a specified pressure gradient. Also, as stated in Na and Moin (1998), when both the streamwise velocity and the wall-normal velocity are simultaneously prescribed, numerical oscillations were observed away from the wall. Thus, most researchers prescribed Dirichlet boundary conditions for either streamwise or wall-normal velocity, and Neumann boundary conditions for the others justified by zero-vorticity or free-stress conditions. Although velocity boundary conditions are predominantly utilized, there are cases that the pressure gradient is achieved by directly prescribing a pressure distribution. Here three types of boundary conditions at the top of the domain were implemented and will be discussed in detail. A choice of boundary conditions used for cases in the later chapters will be specified for each case.

Pressure boundary condition

In principle, pressure boundary conditions can be enforced. However, velocity boundary conditions have been predominantly used in the literature. As far as the author knows, only two boundary layer simulations in which the pressure boundary is imposed have been reported. One is Ferrante and Elghobashi (2004), for DNS of a zero-pressure gradient turbulent boundary layer. The other is Simens (2008), where the pressure boundary condition was discussed in detail with respect to mass conservation and solving Helmholtz equations for pressure in the context of the fractional step method. But the results shown were only for a laminar boundary layer case. None have been found for an adverse-pressure gradient turbulent boundary layer. An important advantage is that by imposing pressure (if known), it is much easier to reproduce experiments (Simens 2008) because it is not necessary to estimate the boundary layer growth rate, nor to adjust the wall-normal velocity to achieve the required pressure gradient. The boundary conditions are

$$P_\infty(x) = f(x) \text{ and } \frac{\partial u}{\partial z} = \frac{\partial v}{\partial z} = 0. \tag{2.20}$$

It should be noted that the boundary condition for the wall-normal velocity at the top is not required, but follows directly from the projection step in the fractional step method context, so that mass is conserved in the computational domain. In contrast to the velocity boundary conditions, it is not required to adjust (small but no physical justification) the velocity field at the boundary, usually at the outflow condition, to satisfy mass conservation. It is expected that the pressure boundary condition will reduce the amount of potential perturbations in the free-stream (Simens 2008). In some cases, it might be also useful to utilize Dirichlet conditions for u by a prescribed velocity profile $U_{ref}(x)$ instead of the stress-free condition. However, one needs to be careful applying this boundary conditions since some authors observed oscillations at the domain top especially when the domain height is not large enough. The free-stream flow at the outer edge of the boundary layer is governed approximately by

$$U_\infty \frac{dU_\infty}{dx} = -\frac{1}{\rho}\frac{dP_\infty}{dx}. \tag{2.21}$$

Zero-vorticity condition

Fasel (1976) pointed out that the zero-vorticity condition at the top-boundary needs a relatively small integration domain in the wall-normal direction. This came from experimental evidence and linear stability theory according to which the perturbation vorticity decays very rapidly in the z-direction and is practically zero at about three boundary-layer thicknesses from the wall. Also the perturbation velocity components, on the other hand, decay rather slowly in the z-direction. Thus one possible choice of the top boundary would be,

$$w = W_{\text{ref}}, \quad \frac{\partial u}{\partial z} = \frac{\partial w}{\partial x} \quad \text{and} \quad \frac{\partial v}{\partial z} = \frac{\partial w}{\partial y}, \tag{2.22}$$

where the suction-blowing distribution of W_{ref} is a prescribed velocity profile that controls the pressure gradient. Variations of this type have been used by Lund et al. (1998), Simens et al. (2009) and Wu and Moin (2009) for a zero-pressure gradient turbulent boundary layer, and Na and Moin (1998) for a separated turbulent boundary layer.

The interesting practical question is how the normal velocity at the top-boundary, W_{ref}, should be chosen to realize the desired pressure gradient. Simens et al. (2009) estimated W_{ref} from the known experimental growth of the displacement thickness. Wu and Moin (2009) prescribe W_{ref} as the analytical profile of the Blasius solution. One way to adjust W_{ref} for known pressure gradient is the following. By an inviscid outer flow approximation, continuity gives

$$\frac{\partial U_\infty}{\partial x} + \frac{\partial W_\infty}{\partial z} = 0. \tag{2.23}$$

Here constant density ($\rho = \text{const}$) is assumed. Assuming potential flow down to the wall, integration in z, $0 \leq z < L_z$ with $z = 0$ at the wall gives,

$$W_\infty(L_z) = -L_z \frac{dU_\infty}{dx}. \tag{2.24}$$

Now in the boundary layer, averaging over the spanwise direction, in which case $\frac{\partial v}{\partial y} = 0$,

$$\frac{\partial u}{\partial x} + \frac{\partial w}{\partial z} = 0. \tag{2.25}$$

Equations (2.23) and (2.25) then give

$$\frac{\partial}{\partial x}\left(U_\infty - u\right) = \frac{\partial}{\partial z}\left(w - W_\infty\right). \tag{2.26}$$

Integrating in z, $0 \leq z < L_z$,

$$\frac{d}{dx}\left[U_\infty \delta^*\right] = w(L_z) - W_\infty(L_z), \tag{2.27}$$

where δ^* is the displacement thickness,

$$\delta^* = \int_0^{L_z} \left(1 - \frac{u}{U_\infty}\right) dz. \tag{2.28}$$

The difference $w(L_z) - W_\infty(L_z)$ is interpreted as a correction to the wall-normal velocity at L_z owing to the slope of δ^*. Therefore, assuming the height of the computational domain is sufficiently high so that the flow at the top is approximately inviscid outer flow,

$$W_{\text{ref}} = w(L_z) = (\delta^* - L_z)\frac{dU_\infty}{dx} + U_\infty \frac{d\delta^*}{dx}. \tag{2.29}$$

For the zero-pressure gradient case,

$$W_{\text{ref}} = U_\infty \frac{d\delta^*}{dx}. \tag{2.30}$$

Because δ^* grows almost linearly in the case of the zero-pressure gradient turbulent boundary layer, Lund et al. (1998) used the average value $d\delta^*/dx$ over the whole domain computed by a linear regression from the local value of δ^* obtained from the mean velocity field. In this case the boundary conditions are reduced to a stress-free condition for the velocity components u and v

$$w = W_{\text{ref}}, \quad \frac{\partial u}{\partial z} = \frac{\partial v}{\partial z} = 0 \text{ at } z = L_z, \tag{2.31}$$

where $W_{\text{ref}}(x)$ is obtained from equation (2.30).

Continuity condition

The normal derivative of the streamwise and spanwise velocity components are set to zero, while the normal component is set to

$$\frac{\partial w}{\partial z} = -\frac{\partial U_{\text{ref}}}{\partial x}. \tag{2.32}$$

In simulating an adverse-pressure gradient turbulent boundary layer, the streamwise velocity profile at the domain top is prescribed especially for flows with a constant pressure-gradient parameter. See Skote and Henningson (2002) and Lee and Sung (2008) for an example. This type of boundary condition is also adopted by Lee et al. (2010),

$$u = U_{\text{ref}}(x), \quad \frac{\partial w}{\partial z} = -\frac{\partial U_{\text{ref}}}{\partial x} \text{ and } \frac{\partial v}{\partial z} = 0. \tag{2.33}$$

2.5 Parallelization

Parallelization of the numerical code is required to perform a large scale simulation, such as DNS and LES of wall-bounded turbulence at high Reynolds numbers. The complete strategy for solving the incompressible Navier-Stokes equations numerically consists of a data decomposition method, a discretization scheme and an appropriate solution technique for the resulting system of linear equations. For an overview on an efficient parallel implementation for the incompressible Navier-Stokes equations we refer the reader to Luchini and Quadrio (2006) and Henniger et al. (2010) and references therein. Our code is designed for distributed-memory machines with the order of $\mathcal{O}(10)$ cores using a message passing interface (MPI). Data is distributed in a simple, slice-like form to break-up the vectors and matrices into smaller blocks considering the simple coordinate system and the number of available cores is about the same order of the grid points in one direction.

A key point to be considered is the nonlocality of the spectral differential operator involved in the pseudospectral method in evaluating the nonlinear terms and solving Poisson-pressure equations. The parallelization is achieved in such a way so as to avoid a Fourier-like transformation across the parallelized domain which requires essentially all-to-all communication, in the spirit of minimizing data exchange among the computing machines. All data along the direction to be transformed must belong to the same subdomain, and data is distributed in y-z sliced domain.

Another point to be considered is how to implement the cosine transform scheme to reduce the problem to one-dimensional Helmholtz equations for pressure. Note that prescribing boundary conditions for velocity at the top instead, allows cosine transformation in either the x- or the z-direction. The cosine transform is performed, however, in the x- not in the z-direction, to accommodate the use of a stretched grid in the wall-normal direction and use of various types of boundary conditions (see §2.4), especially that of Dirichlet boundary conditions for pressure at the domain top. Thus the data along the x-direction are preferred to be contained in the same plane so that the cosine transform can be performed. This is done by first transposing data and then redistributing in an x-z sliced domain followed by solving the system of equations in the z-direction using a serial matrix solver provided by LAPACK. See Figure 2.4 showing distribution of memory and computation.

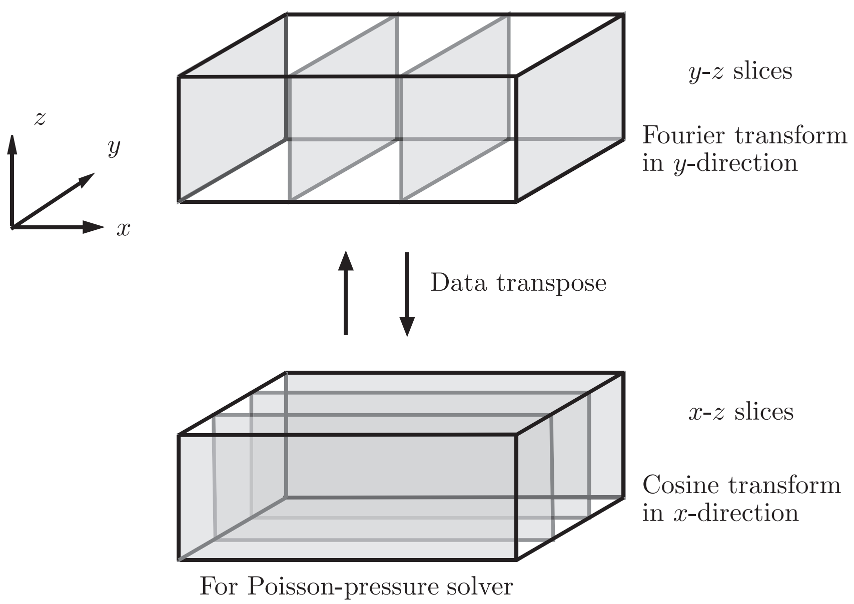

Figure 2.4. Parallelization scheme to distribute memory and computation. Arrangement of data for a parallel execution with four computing cores

All-to-all communication of data is, in general, time consuming and should be avoided. The distributed matrix solver provided by ScaLAPACK, however, turns out to be not suitable for our simulation code using MPI. The code performance including parallel scaling properties are discussed in Appendix B. It should be mentioned, however, that the one possible disadvantage of the choice is that it would limit the number of cores to be used up to the number of grid points to be used in the y-direction.

2.6 Code validation

2.6.1 Method of manufactured solution

In this section the results of spatial and temporal convergence tests are shown. Convergence tests are run using the method of manufactured solutions. The Navier-Stokes equations are forced so that the solution will be a prescribed time-dependent function. The grid points are uniformly spaced in all cases with the same numbers of grid points in x- and z-directions, i.e., $N_x = N_z = N$. An L_2 norm normalized by the exact values

$$L_2 = \sqrt{\frac{\sum_{i,k}(\text{analyticsol.} - \text{numericalsol.})^2}{\sum_{i,k}(\text{analyticsol.})^2}}, \tag{2.34}$$

is examined. The test case is the 2D decaying artificial vortex given by

$$u(x,z,t) = -\sin(ax)\cos(az)\exp\left(-\frac{2t}{Re}\right), \tag{2.35}$$

$$v(x,z,t) = \cos(ax)\sin(az)\exp\left(-\frac{2t}{Re}\right), \tag{2.36}$$

$$p(x,z,t) = \frac{1}{4}\left(\cos(2ax) + \sin(2az)\right)\exp\left(-\frac{4t}{Re}\right), \tag{2.37}$$

where $a = 4\pi$. The divergence of velocity is zero for this test flow. A 2D test case is used for simplicity since a pseudospectral method is employed in the other direction and presently we wish to test the error of finite-difference spatial discretization. When the Reynolds number is small the solution decays rapidly. The Reynolds number Re here is given as $Re = 100$ where the solution changes relatively slowly so that this checks the efficiency of spatial discretization. Also, the time step size is set to $dt = 0.001$ and CFL is the order of 10^{-3}, so that spatial discretization error dominates the overall error in the numerical solution. The numerical domain is $L_x = L_z = 1$. The errors are evaluated at the dimensionless time $t = 200$. The Dirichlet boundary conditions are specified for velocities. The appropriate forcing terms in x- and z-momentum equation in this test case are

$$f_x(x,z,t) = -\frac{1}{Re}\left\{2\left(1-a^2\right)\exp\left(-\frac{2t}{Re}\right)\cos(az)\sin(ax)\right\}, \tag{2.38}$$

$$\begin{aligned} f_z(x,z,t) &= \frac{1}{Re}\left\{2\left(1-a^2\right)\exp\left(-\frac{2t}{Re}\right)\cos(ax)\sin(az)\right\} \\ &+ \frac{a}{2}\exp\left(-\frac{4t}{Re}\right)\left\{\cos(2az)+\sin(2az)\right\}, \end{aligned} \tag{2.39}$$

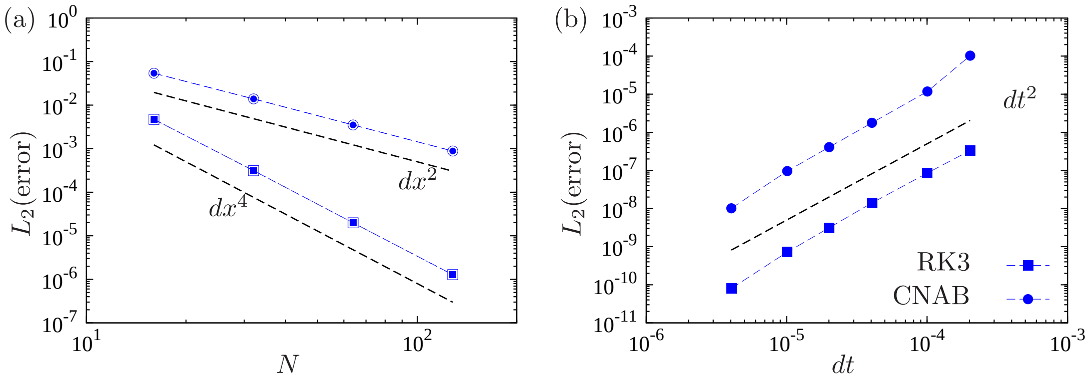

Figure 2.5. The order of convergence of the scheme. (a): Spatial and (b): Temporal

respectively. The order of convergence r is computed via the formula (Strikwerda 1997),

$$r = \frac{\ln\left(\mathrm{error}(h1)/\mathrm{error}(h2)\right)}{\ln\left(h1/h2\right)}, \tag{2.40}$$

using two successive values of the grid spacing $h1$ and $h2$ and the corresponding L_2 norm of error. The results are shown in Table 2.2 and Figure 2.5(a), and fourth-order convergence of the code is shown. The widely used explicit second-order finite-difference scheme is also shown for comparison.

scheme	N	$L_2(u)$	r	$L_2(v)$	r
2nd	16	5.38e-02		5.39e-02	
2nd	32	1.39e-02	1.95	1.39e-02	1.95
2nd	64	3.50e-03	1.98	3.50e-03	1.98
2nd	128	8.81e-04	1.99	8.81e-04	1.99
4th	16	4.71e-03		4.74e-03	
4th	32	3.13e-04	3.91	3.14e-04	3.92
4th	64	1.99e-05	3.98	1.99e-05	3.98
4th	128	1.28e-06	3.96	1.27e-06	3.97

Table 2.2. Convergence test run on both second- and fourth-order-accurate scheme. $Re = 100$, $dt = 0.001$, and the error is evaluated at $t = 200$.

In addition to a spatial convergence test, the order of convergence of two temporal schemes is examined. To determine the temporal order, the numerical solutions were compared to the exact solution and the norm is scaled with the number of steps so that the local order of convergence would be shown. The simulation is conducted using $N_x = N_z = 64$ grids and the error is evaluated at dimensionless time $t = 0.01$. Two temporal integration schemes, a second-order Crank-Nicolson and Adams-Bashforth (CNAB) and a three-order Runge-Kutta (RK3) scheme are examined. Figure 2.5(b) confirms the expected second-order convergence.

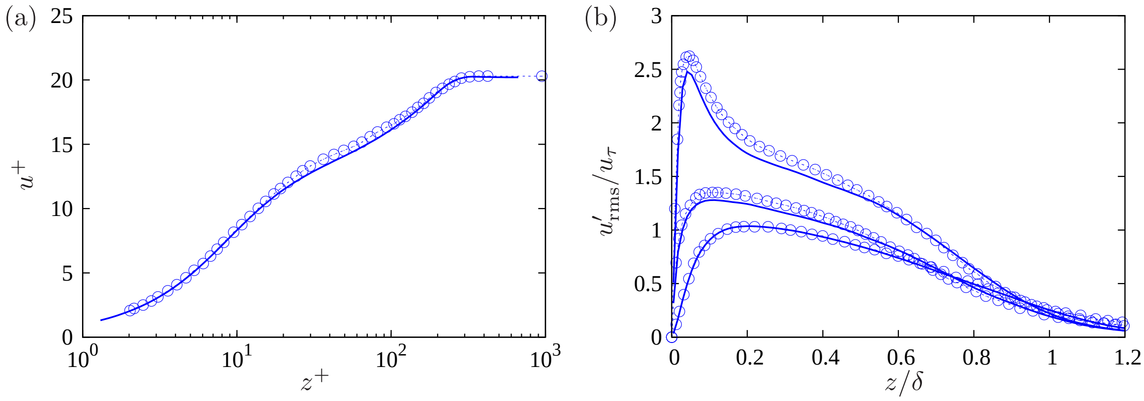

Figure 2.6. Comparison of present results with DNS. (a): Mean velocity profiles u/u_τ, (b): Root-mean square fluctuations. δ is the local 99% boundary layer thickness. ○; Spalart (1988) at $Re_\theta = 670$, the solid lines; current code at $Re_\theta = 666$.

2.6.2 DNS of a zero-pressure gradient turbulent boundary layer

Finally, DNS of a fully-developed turbulent boundary layer over a flat plate under a zero-pressure gradient is performed at moderate Re_θ. Inflow turbulence is generated by the recycling scheme. The pressure boundary conditions are applied:

$$P_\infty(x) = 0 \ \text{ and } \ \frac{\partial u}{\partial z} = \frac{\partial v}{\partial z} = 0 \ \text{ at } \ z = L_z. \tag{2.41}$$

The resolution and domain size are $N_x = N_y = N_z = 256$ and $L_x/\delta_0 = 20$, $L_y/\delta_0 = 4$ and $L_z/\delta_0 = 3$, respectively, with a uniform grid. Results for $Re_\theta = 666$ are shown in Figure 2.6 and they compare well with those of Spalart (1988).

2.7 Discussion

A fourth-order numerical code tailored to perform LES (and some DNS) on turbulent boundary layer flow was developed and implemented in C. Various choices for the boundary conditions are introduced and related issues in solving Navier-Stokes equations are discussed. One-dimensional Helmholtz equations resulting from the Poisson-pressure equation in combination with discrete Fourier- and cosine-transform are solved using an efficient direct method (Henniger et al. 2010). Parallelization using MPI with a data transpose scheme results in a good parallel performance using $\mathcal{O}(10)$ cores. The code implementation performed well in several test cases and the expected fourth-order convergence was obtained in space and time.

Chapter 3

LES of the zero-pressure gradient turbulent boundary layer

3.1 Background

Research on turbulent boundary layers (TBL) has a long history. There have been many classic experiments on both the low- and high-Reynolds-number developing equilibrium TBL varying from low, near transition (Erm and Joubert 1991) to large, laboratory scale Reynolds numbers, (Österlund 1999, Hutchins and Marusic 2007b, Klebanoff 1954, DeGraaff and Eaton 2000) and others, to huge values with Kármán number $Re_\tau \approx 10^6$ (Metzger et al. 2007) typical of atmospheric surface layer TBLs.

DNS of the Navier-Stokes equations has reached a stage of development where the TBL at the lower end of the Re_θ range, of order $Re_\theta = 1\text{–}5 \times 10^3$ have been successfully performed for both the transition (Wu and Moin 2009) and the fully developed TBL case (Spalart 1988, Spalart et al. 1991, Ferrante and Elghobashi 2004, 2005, Simens et al. 2009, Schlatter and Örlü 2010, Araya et al. 2011). See Schlatter and Örlü (2010) for an interesting compilation of recent DNS results. Unlike channel or pipe flow, the thickness of the turbulent zone, or TBL thickness $\delta(x)$ and the wall-shear stress $\tau_w(x)$ vary with streamwise distance and are not fixed in advance by the channel height or the applied, favorable pressure gradient. They must be computed as part of the simulation. Moreover the flow outside the TBL may be either smooth or contain free-stream turbulence and may also contain wall-normal transpiration velocities which are related to the pressure gradient and which must be accurately represented in any simulation. Nonetheless the near-wall regions of channel/pipe flow and that of the TBL are similar, even though the scaling may not be identical (e.g., Spalart 1988, DeGraaff and Eaton 2000), which suggests that the present near-wall SGS model, which is entirely local in character including its incorporation of local pressure gradients, should be applicable at least to spatially developing equilibrium boundary layers.

Presently this model is extended to the LES of the zero-pressure gradient, flat-plate turbulent boundary layer (ZPGFPTBL). In §3.2 the present SGS wall model is described. The results of the present LES over a wide range of Reynolds numbers are described in detail in §3.3 while some conclusions and scenarios suggested by the LES are discussed in §3.4.

3.2 Subgrid-scale model for wall-bounded flow

We now briefly describe the SGS model: for details see Chung and Pullin (2009). In the following x_1 or x is the streamwise coordinate, x_2 or y is the spanwise coordinate, and x_3 or z is the wall-normal coordinate. The generically filtered Navier–Stokes equations with filter scale Δ_c are

$$\frac{\partial \widetilde{u}_i}{\partial t} + \frac{\partial \widetilde{u}_i \widetilde{u}_j}{\partial x_j} = -\frac{\partial \widetilde{p}}{\partial x_i} + \nu \frac{\partial^2 \widetilde{u}_i}{\partial x_j^2} - \frac{\partial T_{ij}}{\partial x_j}, \quad \frac{\partial \widetilde{u}_i}{\partial x_i} = 0, \tag{3.1}$$

where $\widetilde{u}_i$ is the filtered velocity, $T_{ij} = \widetilde{u_i u_j} - \widetilde{u}_i \widetilde{u}_j = \widetilde{\widetilde{u}_i u_j'} + \widetilde{u_i' \widetilde{u}_j} + \widetilde{u_i' u_j'}$ is the subgrid stress tensor, ν is the kinematic viscosity and p is pressure divided by density.

3.2.1 The stretched-vortex subgrid-scale model

Embedded within each computational cell, it is assumed that there exists a superposition of stretched vortices, each having orientation taken from a delta-function probability density function (p.d.f.) that is either prescribed or dynamic (Misra and Pullin 1997). In the simplest version, used presently, a single active subgrid vortex is aligned with the unit vector $\boldsymbol{e}^v$, with resulting subgrid stress tensor

$$T_{ij} = (\delta_{ij} - e_i^v e_j^v) K, \qquad K = \int_{k_c}^{\infty} E(k)\, \mathrm{d}k, \tag{3.2}$$

where K is the subgrid kinetic energy. The cutoff wavenumber is $k_c = \pi/\Delta_c$, $\Delta_c = (\Delta_x\, \Delta_y\, \Delta_z)^{1/3}$, and $E(k)$ is the SGS energy spectrum. The latter is obtained by supposing that the SGS vortices are of the stretched-spiral type, which have energy spectra (Lundgren 1982)

$$E(k) = \mathcal{K}_0 \epsilon^{2/3} k^{-5/3} \exp\left[-2k^2 \nu/(3|\widetilde{a}|)\right], \tag{3.3}$$

where $\widetilde{a} = e_i^v e_j^v \widetilde{S}_{ij}$, the stretching felt along the subgrid vortex axis imposed by the resolved scales, and $\widetilde{S}_{ij} = (1/2)\,(\partial \widetilde{u}_i/\partial x_j + \partial \widetilde{u}_j/\partial x_i)$ is the resolved strain-rate tensor. Combining the second of (3.2) and (3.3) gives

$$K = \tfrac{1}{2}\, \mathcal{K}_0' \,\Gamma\left[-1/3, \kappa_c^2\right], \quad \mathcal{K}_0' = \mathcal{K}_0 \epsilon^{2/3} \lambda_v^{2/3}, \qquad \lambda_v = (2\nu/3|\widetilde{a}|)^{1/2}, \quad \kappa_c = k_c \lambda_v, \tag{3.4}$$

and Γ is the incomplete gamma function. Presently $\boldsymbol{e}^v$ is aligned with the principal extensional eigenvector of the resolved-scale rate-of-strain tensor except at the wall (see §3.2.3). We note that

$\boldsymbol{e}^v$ can be a discontinuous function of S_{ij} when the most extensional and intermediate eigenvalues exchange. Our experience is that the spatial measure of this is negligible and has no effect on the LES. The parameter $\mathcal{K}_0\epsilon^{2/3}$ is obtained dynamically by structure-function matching at the grid-scale cutoff (Voelkl et al. 2000, Chung and Pullin 2009).

Chung and Pullin (2009) extended (3.2) to incorporate transport of axial velocity, modeled as a passive scalar, by subgrid-scale vortices (Pullin 2000, Pullin and Lundgren 2001, O'Gorman and Pullin 2003, Chung and Pullin 2009),

$$\widetilde{v_i'\widetilde{v}_3} = -K_s \frac{\partial \widetilde{v}_3}{\partial y_i} \quad \text{for} \quad i = 1, 2, \tag{3.5}$$

and $\widetilde{v_3'\widetilde{v}_3} = 0$, where v_i and y_i are the vortex-frame velocity and spatial co-ordinates respectively. Note that y_3 coincides with the vortex axis, $2\,K_s = \gamma\,\Delta_c\,K^{1/2}$ and γ is a momentum mixing constant to be discussed subsequently. Adding this modeling of axial velocity transport to (3.2), and rotating back to the frame of computational domain, Chung and Pullin (2009) arrived at

$$T_{ij} \equiv \widetilde{u_i'u_j'} + \widetilde{u_i'\widetilde{u}_j} + \widetilde{\widetilde{u}_i u_j'} = K(\delta_{ij} - e_i^v e_j^v) - K_s \left[e_j^v e_k^v \frac{\partial \widetilde{u}_k}{\partial x_l}(\delta_{li} - e_l^v e_i^v) + e_i^v e_k^v \frac{\partial \widetilde{u}_k}{\partial x_l}(\delta_{lj} - e_l^v e_j^v) \right]. \tag{3.6}$$

The term in square brackets on the right-hand side represents the axial transport of the resolved-scale flow by a subgrid vortex. This term can be interpreted as a model of $\widetilde{u_i'\,\widetilde{u}_j} + \widetilde{u_j'\,\widetilde{u}_i}$ in the definition of T_{ij}. This will later be the dominant transport term in the near-wall model.

3.2.2 The wall-shear stress

The main idea is to integrate across the near-wall layer in a way that models the appropriate physics and recognizes anisotropy while providing a slip boundary condition at a raised virtual wall for the resolved-scale LES (Chung and Pullin 2009). With the physical wall at $z = 0$, we apply to the streamwise momentum equation an xy-plane filter "$\widetilde{\quad}$" and a top-hat, or averaging wall-normal filter

$$\langle \phi \rangle(x, y, t) \equiv \frac{1}{h} \int_0^h \widetilde{\phi}(x, y, z, t)\,\mathrm{d}z, \tag{3.7}$$

over a wall-adjacent layer of height h to obtain

$$\frac{\partial \langle u \rangle}{\partial t} + \frac{\partial \langle uu \rangle}{\partial x} + \frac{\partial \langle uv \rangle}{\partial y} = -\frac{1}{h}\,\widetilde{uw}|_h - \left.\frac{\partial \widetilde{p}}{\partial x}\right|_h + \frac{\nu}{h}\left(\left.\frac{\partial \widetilde{u}}{\partial z}\right|_h - \eta_0 \right), \tag{3.8}$$

where we have used the wall boundary condition $\widetilde{u}(x, y, 0, t) = 0$ and have neglected lateral diffusion. The local wall-normal velocity gradient is

$$\eta_0(x, y, t) \equiv \left(\frac{\partial \widetilde{u}}{\partial z} \right)_{z=0}. \tag{3.9}$$

The local wall shear stress is $\tau_0(x, y, t)/\rho = \nu\eta_0(x, y, t) \equiv u_\tau^2(x, y, t)$ where u_τ is the wall friction velocity and the viscous wall unit is $l^+ \equiv \nu/u_\tau$.

Equation (3.8) can be reduced to an ODE for the wall-normal velocity gradient η_0 by using a local inner-scaling ansatz of the form

$$\widetilde{u}(x, y, z, t) = (\nu\eta_0(x, y, t))^{1/2} F(z^+), \quad z^+ = z\,(\eta_0(x, y, t)/\nu)^{1/2} \equiv z/l^+, \tag{3.10}$$

applied to the unsteady term only, and by approximating the x and y convective terms by their value at the top of the integrated wall layer $z = h$ with the result (Chung and Pullin 2009)

$$\frac{\partial \eta_0}{\partial t} = \frac{2\eta_0}{\widetilde{u}|_h}\left[-\frac{1}{h}\,\widetilde{uw}|_h - \frac{\partial \widetilde{uu}|_h}{\partial x} - \frac{\partial \widetilde{uv}|_h}{\partial y} - \left.\frac{\partial \widetilde{p}}{\partial x}\right|_h + \frac{\nu}{h}\left(\left.\frac{\partial \widetilde{u}}{\partial z}\right|_h - \eta_0\right)\right]. \tag{3.11}$$

Owing to a cancelation of two integrals arising from the wall-normal integration, the specific form of $F(z^+)$ in $0 \le z < h$ does not appear in (3.11) .

In the LES, (3.11) is an auxiliary equation to determine the evolution of u_τ. For the present staggered-grid numerical method, we set $h = h_0 + \Delta_z/2$ where h_0 is the wall-normal distance of the virtual wall from the physical wall and Δ_z is the near-wall cell size. The first grid point for the streamwise velocity component within the LES domain is at $\Delta_z/2$. The quantities on the right-hand side are determined from resolved-scale LES quantities at $z = h$. This allows determination of u_τ without resolving the near-wall steep gradients. To close this coupling, appropriate boundary conditions for the LES are required.

3.2.3 Slip velocity at a raised or "virtual" wall

The LES takes place above a fixed, Reynolds-number-independent height, $h_0 = \alpha\,\Delta_z$, $\alpha < 1$. Chung and Pullin (2009) defined three regions near the wall (see their Figure 1): (I) $0 \le z \le h_\nu$, essentially the viscous sublayer, (II) $h_\nu < z \le h_0$, an overlap layer where the shear stress is approximately constant, and is modeled by the extended stretched-vortex SGS model consisting of attached vortices aligned with $\boldsymbol{e}_x$, and (III) $h_0 < z$, where nonuniversal outer flow features are computed with LES coupled with the original stretched-vortex SGS model of detached subgrid vortices aligned with $\boldsymbol{e}_{\widetilde{S}}$. The plane $z = h_0$ is a lifted virtual wall. In region (I) we use $\widetilde{u}^+ = z^+$, where $\widetilde{u}^+ = \widetilde{u}/u_\tau$, $z^+ = z/l^+$, and u_τ is known from (3.11). In particular, $\widetilde{u}^+|_{h_\nu} = h_\nu^+$, where $h_\nu^+ = h_\nu/l^+$. For a hydrodynamically smooth wall we use the empirical value $h_\nu^+ \approx 10.23$ based on the intercept between the linear and log component of the law of the wall. Hence $\widetilde{u}^+|_{h_\nu} = h_\nu^+ = 10.23$. This is the only empirical constant in the present model.

Chung and Pullin (2009) derived an effective slip-velocity at the top of region (II), $h_\nu < z \le h_0$ in a way that couples both (3.6) and (3.11). Briefly it is assumed that in region (II) the total shear stress is approximately constant (Townsend 1976) and that near-wall vortices are streamwise aligned (see, e.g., Head and Bandyopadhyay 1981, Robinson 1991) $(e_x^v, e_y^v, e_z^v) = (1, 0, 0) \Leftrightarrow \boldsymbol{e}^v = \boldsymbol{e}_x$. Substituting these into the stretched-spiral vortex extended model, (3.6), and noting that the only nonzero component of the mean velocity gradient tensor is $\mathrm{d}\widetilde{u}/\mathrm{d}z$ then gives

$$T_{xz} = -\frac{1}{2}\gamma_{\mathrm{II}} K^{1/2} \Delta_c \frac{\mathrm{d}\widetilde{u}}{\mathrm{d}z}. \tag{3.12}$$

The physical mechanism that produces this shear stress is the action of the spiraling streamwise vortices winding the local axial velocity, now identified as the mean streamwise velocity, thereby transporting higher momentum fluid towards the wall and transporting low momentum fluid away from the wall.

Assuming that SGS vortices in (II) are "attached to the wall" and that $\Delta_c = z$ (vortex size scales with wall distance (Townsend 1976, Perry and Chong 1982, Nickels et al. 2007)) then $\widetilde{u}$ can be integrated within region (II) to give (Chung and Pullin 2009)

$$\widetilde{u}|_{h_0} = u_\tau \left(\frac{1}{\mathcal{K}_1} \log\left(\frac{h_0}{h_\nu}\right) + h_\nu^+ \right), \qquad \mathcal{K}_1(x, y, t) = \frac{\gamma_{\mathrm{II}} K^{1/2}}{2\,(-T_{xz}/u_\tau)}, \tag{3.13}$$

where the constant of integration is chosen by putting $\widetilde{u}|_{h_\nu} = u_\tau\, h_\nu^+$. Equation (3.13) and $\widetilde{w}$ obtained from continuity give the Dirichlet boundary conditions at the lifted virtual wall h_0, where u_τ is obtained from the solution of (3.11). The parameter $\mathcal{K}_1(x, y, t)$ is an effective Kármán constant, κ. The vertical momentum mixing constant γ_{II} is estimated by matching Townsend's structure parameter $a_1 = T_{13}/T_{ii} = T_{13}/(2K)$ at the interface of regions (II) and (III), $z = h_0$, where both inner and outer layer modeling ideas are valid, giving $\gamma_{\mathrm{II}} = 2^{1/2}/\pi \approx 0.45$ (Chung and Pullin 2009). This value used presently for all LES.

The empirical log law is usually written as

$$\widetilde{u}(z) = u_\tau \left(\frac{1}{\kappa} \log\left(\frac{z}{l^+}\right) + B \right), \tag{3.14}$$

where B is a constant and κ the usual Kármán constant. Putting $h_0 = z$ in (3.13), identifying $\mathcal{K}_1$ with κ and comparing these equations gives

$$B = h_\nu^+ - \frac{\log h_\nu^+}{\mathcal{K}_1}. \tag{3.15}$$

Hence our specification of h_ν^+ is equivalent to specifying B. Even though in LES we calculate $\mathcal{K}_1$ dynamically, we illustrate this equivalence by the choice $\kappa = 0.4$, $h_\nu^+ = 10.23$ which gives $B \approx 4.42$. This is within the commonly accepted range of $4.0 - 5.0$.

3.2.4 PDE model for wall-shear stress

We refer to the above, with η_0 determined by (3.11) as our "ODE" model. For spatially developing flows improvements to equation (3.8), may be required. For channel flow the dominant terms in (3.11) are expected to be the driving pressure gradient balanced against the wall shear stress and the wall-normal Reynolds stress at the top of the layer. In particular, the streamwise inertial terms are expected to be small. For spatially developing flows this dominant balance will change and an alternative model of the inertial term $\partial < uu > /\partial x$, which in (3.8) is modeled from the outer LES, should be considered. We again use the idea of local inner scaling, but now applied to $\widetilde{u^2}(x, y, z, t)$ in (3.8) as

$$\widetilde{u^2}(x, y, z, t) = \nu\, \eta_0(x, y, t)\, G(z^+), \quad z^+ = z\, (\eta_0(x, y, t)/\nu)^{1/2} \equiv z/l^+, \tag{3.16}$$

from which it is easy to show that

$$\frac{\partial}{\partial x} < u^2 >= \frac{1}{2}\frac{1}{\eta_0}\frac{\partial \eta_0}{\partial x}\left(< u^2 > + \widetilde{u^2}|_h\right), \tag{3.17}$$

where $< ... >$ is defined prior to (3.8). This latter equation, which replaces (3.11), is then

$$\frac{\partial \eta_0}{\partial t} + \left(\widetilde{u}|_h + \frac{< u^2 >}{\widetilde{u}|_h}\right)\frac{\partial \eta_0}{\partial x} = \frac{2\eta_0}{\widetilde{u}|_h}\left[-\frac{1}{h}\,\widetilde{uw}|_h - \frac{\partial \widetilde{uv}|_h}{\partial y} - \left.\frac{\partial \widetilde{p}}{\partial x}\right|_h + \frac{\nu}{h}\left(\left.\frac{\partial \widetilde{u}}{\partial z}\right|_h - \eta_0\right)\right], \tag{3.18}$$

where we have put $\widetilde{u^2}|_h/\widetilde{u}|_h = \widetilde{u}|_h$ owing to the delta-function filter. This is a hyperbolic partial-differential equation (PDE) for the wall-normal velocity derivative η_0(x,t). Unlike the unsteady term, the profile function G in (3.16) does not vanish and $< u^2 >$ in (3.18) must be approximated. This coefficient can be evaluated using a combination of (3.13), (with h_0 replaced by z) and a linear relationship for $z^+ < 10.23$. All coefficients in (3.18) can then be evaluated dynamically and no new parameters are introduced. The coefficient $c \equiv \widetilde{u}|_h + < u^2 > /\widetilde{u}|_h$ can be interpreted as a local wavespeed for shear fluctuations at the wall. We will refer to LES with η_0 determined by (3.18) as a "PDE" model.

3.2.5 Summary of SGS wall model

The near-wall SGS model can be summarized as follows: for every cell adjacent to the bottom walls (3.11) is solved for η_0 with terms on the right-hand side provided by the LES at the first grid point for the streamwise velocity component. This provides $\eta_0(x, y, t)$ and thus $u_\tau(x, y, t)$. Equation (3.13) is then used to evaluate the streamwise slip velocity $\widetilde{u}|_{h_0}(x, y, t)$ at $z = h_0$, with $\mathcal{K}_1$ evaluated from the second of (3.13) with K and T_{xz} evaluated at $z = h$ from the LES structure-function-matching procedure. The other boundary conditions at $z = h_0$ are $\widetilde{v}|_{h_0}(x, y, t) = 0$, $\widetilde{w}|_{h_0}(x, y, t) = -2\, h_0\, \widetilde{u}|_{h_0}\, (\partial \eta_0/\partial x)/(2\, \eta_0)$ from wall-normal integration of continuity. This method couples the LES to the modeled, near-wall dynamics. Presently we use $h_0 = 0.18\,\Delta_z$ for the most cases, independent of the LES resolution, and consider this as part of the overall grid. A test to investigate sensitivity to h_0 is performed using $h_0 = 0.36\,\Delta_z$, and further tests can be found in (Chung and Pullin 2009) for LES of channel flow. The near-wall SGS model provides a means of dynamically calculating the instantaneous local "Kármán constant", $\mathcal{K}_1$, as part of the integrated SGS-model coupled to the LES.

3.3 LES of the zero-pressure gradient turbulent boundary layer

3.3.1 Numerical method

The numerical method has been described in details in Chapter 2. Only a short summary and description in the context of LES of the zero-pressure gradient turbulent boundary layer are provided here. The governing equations are solved in a box with dimensions $L_x \times L_y \times L_z$, with periodic boundary condition in the spanwise or y-direction. The components of the velocity vector $\mathbf{u}$ are u, v and w in the streamwise (x-), spanwise (y-), and wall-normal (z-) directions, respectively. A convective boundary condition (2.19) has been implemented at the outflow boundary. At the upper/free-stream boundary we presently use stress-free conditions for u and v and a Dirichlet condition for w (2.31), where, δ^*, the boundary layer displacement thickness computed from the mean velocity field. Inflow-boundary conditions suitable for the fully developed ZPGFPTBL have been implemented for LES as described below.

For the fully developed ZPGFPTBL a code-A only, recycling flow method shown in Figure 2.2, is used for the LES. For inflow we use the method of Lund et al. (1998). Briefly the velocity data at a downstream location, referred to as the "recycling plane" (Figure 2.2), is rescaled to account for the growth of the thickness of the boundary layer in the x-direction. It is then reintroduced at the inlet of the computational domain. The velocity is decomposed into a mean and fluctuating part and the appropriate empirical similarity scaling laws are then applied to each component separately. The rescaling technique is based on the assumption that the velocity profile at both the recycling and inlet planes satisfy the similarity law of the boundary layer, namely, the law of the wall in the inner part and the defect law in the outer part. Also u_τ (we actually use η_0) at the inlet is estimated by the scaling relationship

$$u_{\tau,\text{inlet}} = u_{\tau,\text{recycle}} \left(\theta_{\text{recycle}}/\theta_{\text{inlet}}\right)^{1/[2(n-1)]}, \tag{3.19}$$

which can be derived using a standard power-law approximation, presently with $n = 7$. The recycling plane is generally at $0.8\,L_x$ although, as discussed subsequently, other values are also used.

The present code is optimized for parallel simulation of the boundary-layer flow, and the overhead for the implementation of stretched-vortex model, including the wall model is of order 80% when the model is implemented at every grid point. This includes solving a cubic analytically for the eigenvector directions, the structure function calculations per grid point, the calculation of the SGS kinetic energy and the SGS stresses and the solution of the wall model ODEs. In practice the SGS model is switched off in the free-stream and so the total SGS overhead is of order 30–40%. While this is not small it will be seen that the LES can be run with uniform grids, with no near-wall refinement required, to essentially arbitrarily large Reynolds number, and at a cost independent of Reynolds number. The implementation of both the interior SGS model and the wall model are local.

3.3.2 Range of LES performed

The near-wall SGS model was implemented for the purpose of performing LES of the ZPGFPTBL over a range of Re_θ. Equation (3.11) was solved by the same third-order Runge-Kutta scheme as the main part of the flow simulation. LES have been performed at several different resolutions (N_x,N_y,N_z) and for several domain sizes (L_x/δ_0,L_y/δ_0,L_z/δ_0) summarized in Table 3.1. For all LES the grid size in each direction was uniform with no stretching in the wall-normal direction. In total the results of some 32 different LES are reported in detail presently and additional LES are also mentioned briefly. Typically an individual LES is done by fixing a nominal Reynolds number $Re_0 = U_\infty \delta_0/\nu$ where δ_0 is the inlet boundary-layer thickness. This will then span a range of Reynolds number Re_θ, which is an output of the LES. The parameter x_{ref}/L_x gives the position of the recycling plane as a fraction of the streamwise domain L_x and it is noted that two different values were used with little effect on the present results shown. The inflow generation scheme of Lund et al. (1998) was used for all LES except for case B4a, where the mirroring method proposed by Jewkes et al. (2011) was implemented. This will be discussed subsequently.

Some physical parameters of interest are the displacement and momentum thicknesses δ^* and θ, respectively and the Rotta-Clauser length scale $\Delta \equiv U_e^+\,\delta^*$ where U_e^+ and the skin-friction coefficient C_f are given by

$$U_e^+ \equiv \frac{U_\infty}{u_\tau} = \sqrt{\frac{2}{C_f}}, \qquad C_f \equiv \frac{\tau_w}{\frac{1}{2}\,\rho\,U_\infty^2}. \tag{3.20}$$

All results shown presently are obtained as spanwise/time averages as a function of streamwise distance. Owing to the large range of Re_θ explored, LES results were obtained using many different Re_0. In what follows we will distinguish between our SGS/LES estimate of the Kármán constant $\mathcal{K}_1$ and experimental estimates which will be denoted by κ.

3.3.3 Effect of resolution and domain length

The effect of LES resolution at $Re_\theta \approx 2.5 \times 10^4$ from case A4, A4L and A4H, is shown in Figures 3.1 and 3.2, respectively, and also in Table 3.2, which also shows the effect of resolution using cases A16, A16L and A16H at $Re_0 = 100G$. Case A4a is to investigate the sensitivity to h_0 using $h_0/\Delta_z = 0.36$. For the other cases $h_0/\Delta_z = 0.18$ is fixed for each of the three resolutions so that h_0/δ_{99} reduces with increasing resolution. In Figure 3.1(a) the plots of U_e^+ versus Re_θ show a hill or bump after the inlet, also seen in DNS studies (Simens et al. 2009), which is perhaps the effect of nonequilibrium, or transition, following inlet as a result of the recycling procedure with fixed $n = 7$ in (3.19). The wall-normal profiles discussed subsequently were always downstream of the hill. Further, apart from the small rise in U_e^+, we find negligible effect of transition on profiles of mean streamwise velocity and turbulent intensities when wall-normal profiles are plotted at various streamwise stations down the whole simulation domain for a given LES. A dynamic recycling method that eliminates the need for (3.19) has been proposed by Araya et al. (2011), which may alleviate this effect, and which may allow shorter domain sizes in both DNS and LES of spatially developing boundary-layer flows. This has not been used presently.

Comparisons are also made in Figure 3.1(a) with the experiments of Österlund (1999). The lowest resolution LES contains only 15–20 points in the turbulent boundary layer but still captures the the skin friction characterized as U_e^+, the shape factor H and the mean velocity profile reasonably accurately. Table 3.2 shows only a small variation in the calculated Kármán constant with different resolution, at each of the two Re_θ. Some small effects of doubling the grid size ratio, h_0/Δ_z, of the height of the virtual wall to the grid size in the z-direction from $h_0/\Delta_z = 0.18$ to 0.36, are observed. These are about 1% deviation on $\mathcal{K}_1$ and H, 5% on Re_θ and U_e^+. Chung and Pullin (2009) performed similar tests and found that the deviations on u_τ to be from 1% to 4%. We remark that h_0 is always a fixed fraction of the uniform wall-normal cell size Δ_z. It follows that increasing the vertical resolution by a factor say M then decreases h_0 as a fraction of any measure of the boundary layer thickness, say δ, by a factor $1/M$. Hence increasing the resolution by a factor of two, with h_0/Δ_z fixed, may be interpreted as testing the effect of decreasing h_0/δ by a factor 1/2.

It can be seen in Figure 3.1(b) (also see Figure 4.3 in the next Chapter) that there is a drop off in u^+ towards the virtual wall. We interpret this as the influence of a near-wall length-scale of order the cell size as analyzed by Brasseur and Wei (2010). They argue that this is a logarithmic-layer mismatch and discuss in detail the simulation conditions under which this effect can be minimized by placing parameters into a domain referred to as the “high-accuracy zone”. One condition, namely the number of points in the boundary layer of order 50–60 is approximately satisfied by our highest vertical resolution $N_z = 256$ (Case A4H and A16H) but not by the wall-normal resolution $N_z = 128$ used in the majority of the present LES. While the Brasseur-Wei effect is certainly seen in the present LES we remark that we do not obtain estimates of the Kármán constant from the mean

Case	Re_0	L_x/δ_0	L_y/δ_0	L_z/δ_0	N_x	N_y	N_z	h_0/δ_0	x_{ref}/L_x
A1-A20	16k - 10T	36	6	4	384	64	128	5.6e-3	80%
A4a	200k	36	6	4	384	64	128	1.1e-2	80%
A4L	200k	36	6	4	192	32	64	1.1e-3	80%
A4H	200k	36	6	4	768	128	256	2.8e-3	80%
A16L	100G	36	6	4	192	32	64	1.1e-3	80%
A16H	100G	36	6	4	768	128	256	2.8e-3	80%
B4	200k	72	6	4	768	64	128	5.6e-3	40%
B4a*	200k	72	6	4	768	64	128	5.6e-3	40%
B4b	200k	72	6	4	768	64	128	5.6e-3	80%
B16	100G	72	6	4	768	64	128	5.6e-3	40%
B18	1T	72	6	4	768	64	128	5.6e-3	40%
C16	100G	144	6	4	1536	64	128	5.6e-3	20%
C18	1T	144	6	4	1536	64	128	5.6e-3	20%

Table 3.1. Simulation parameters: $k \equiv 10^3$, $M \equiv 10^6$, $G \equiv 10^9$, $T \equiv 10^{12}$; $Re_0 = U_\infty \delta_0/\nu$; U_∞ is the free-stream velocity, δ_0 is the 99% boundary layer thickness at the inlet of the domain. $\Delta_x = \Delta_y = 3\Delta_z$. $h_0 = 0.18\Delta_z$, except for case A4a where $h_0 = 0.36\Delta_z$. Re_0 for each case A is, A1: 16k, A2: 64k, A3: 160k, A4: 200k, A5: 640k, A6: 1M, A7: 4M, A8: 10M, A9: 40M, A10: 100M, A11: 400M, A12: 1G, A13: 4G, A14: 10G, A15: 40G, A16: 100G, A17: 400G, A18: 1T, A19: 4T, A20: 10T. *: The mirroring method is employed for inflow generation scheme.

velocity profile but rather direct from the SGS model (see equation (3.13)).

In Figure 3.2(a–b), the streamwise turbulent intensities and the Reynolds stress contain SGS corrections to the resolved-flow calculated as $\overline{u_i' u_j'} = \overline{\widetilde{u}_i{}' \widetilde{u}_j{}'} + \overline{T_{ij}}$. The higher resolution LES results for the streamwise intensity $\overline{u_i'^{2+}}$ in Figure 3.2(a) show a somewhat more flattened shape than the measurements of Marusic et al. (2010a), underestimating the experiment nearer the wall by 15%. In Figure 3.2(b), the Reynolds stress $\overline{u'w'^+}$ is essentially independent of resolution.

Some LES were also performed for a longer domain using the intermediate resolution (Case Bs, Cs). Table 3.3 indicates that the effect of doubling the domain length in the streamwise direction on some of the principal parameters is small. A similar sensitivity on the mean velocity and turbulence intensity profiles (not shown) was also found. Longer domains are, however, expected to be required to better capture the dynamics of long structures of, order 15–20 boundary layer thicknesses observed in the logarithmic region of the TBL (Kim and Adrian 1999, Hutchins and Marusic 2007a,b). This issue is not addressed presently. Additionally, many LES not reported presently were performed to explore the effect of using both the A&B code approach and also the alternative, stress-free boundary conditions at the upper boundary. These variations did not produce LES results that were significantly different from those discussed below.

3.3.4 Skin friction and H-factor

Most of the LES discussed subsequently were performed with our intermediate resolution and correspond to cases A1–A20 of Table 3.1. Figures 3.3 and 3.4 plot the outer velocity normalized by the

Case	$N_x,\ N_y,\ N_z$	Re_θ	U_e^+	$\overline{\mathcal{K}_1}$	H
A4L	192, 32, 64	2.53×10^4	30.4	0.382	1.30
A4	384, 64, 128	2.51×10^4	30.2	0.387	1.27
A4a	384, 64, 128	2.39×10^4	31.8	0.382	1.29
A4H	768, 128, 256	2.51×10^4	30.2	0.397	1.27
Experiment	n/a	2.58×10^4	30.5	0.384	1.30
A16L	192, 32, 64	6.13×10^9	61.4	0.371	1.18
A16	384, 64, 128	6.12×10^9	61.5	0.371	1.14
A16H	768, 128, 256	6.12×10^9	61.8	0.370	1.12

Table 3.2. Effect of resolution. Domain size fixed to $(L_x/\delta_0,\ L_y/\delta_0, L_z/\delta_0) = (36, 6, 4)$. Experimental data; Österlund (1999), $Re_\theta = 25767.5$. Data are taken at $x/\delta_0 \approx 28$.

Case	L_x/δ_0	x_{ref}/δ_0	Re_θ	U_e^+	$\overline{\mathcal{K}_1}$	H
A4	36	28.8	2.51×10^4	30.2	0.388	1.27
B4	72	28.8	2.52×10^4	30.2	0.387	1.27
B4a	72	28.8	2.52×10^4	30.2	0.388	1.27
B4b	72	57.6	2.51×10^4	30.1	0.390	1.27

Table 3.3. Effect of domain size and the location of the recycling plane at $Re_\theta \approx 2.5\times10^4$. Data are taken at $x/\delta_0 \approx 28$.

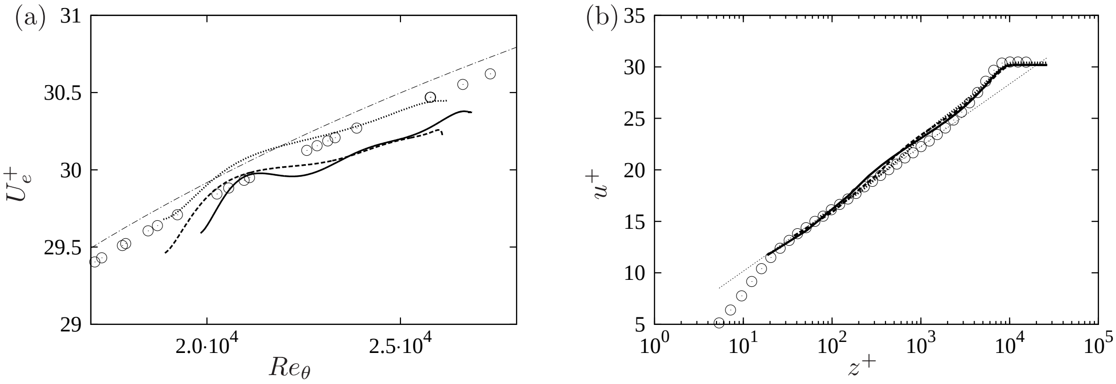

Figure 3.1. (a): U_e^+ versus Re_θ and Coles-Fernholz 2 (Nagib et al. 2007), (b): Mean streamwise velocity $u^+ \equiv \overline{u}/u_\tau$ and a log relationship with $\kappa = 0.384$ and $B = 4.127$ suggested by the experiment of Österlund (1999), $Re_\theta \approx 2.5\times10^4$. Open symbols: experiment (Österlund 1999). Lines are LES; dotted: lowest resolution ($192\times32\times64$) (case A4L), dashed: intermediate resolution ($384\times64\times128$) (case A4), solid: highest resolution ($764\times128\times256$) (case A4H)

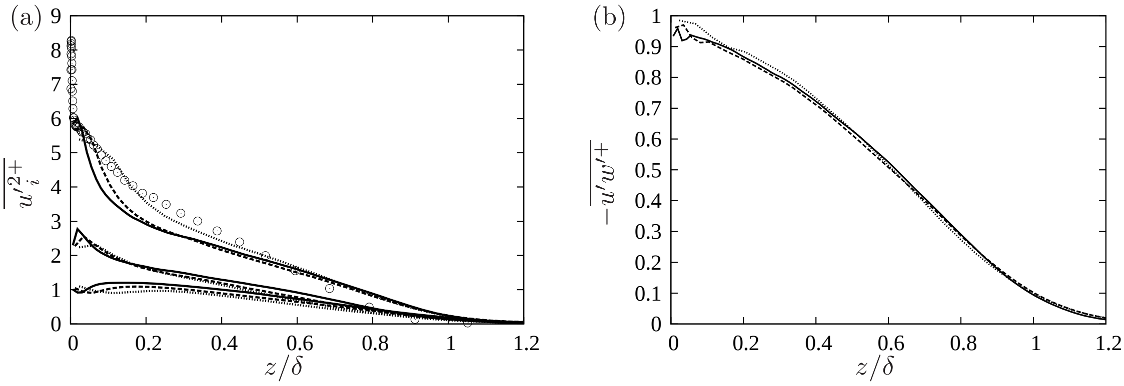

Figure 3.2. $Re_\theta \approx 2.5 \times 10^4$. (a): Streamwise (top), spanwise (middle), and wall-normal (bottom) intensities $\overline{u_i'^{2+}} \equiv \overline{u_i'^2}/u_\tau^2$, (b): Reynolds shear stresses $\overline{u'w'^+} \equiv \overline{u'w'}/u_\tau^2$. Open symbols: experiment at $Re_\theta = 2.0 \times 10^4$ (Marusic et al. 2010a). Lines are LES; dotted: lowest resolution ($192 \times 32 \times 64$) (case A4L), dashed: intermediate resolution ($384 \times 64 \times 128$) (case A4), solid: highest resolution ($764 \times 128 \times 256$) (case A4H). δ is the local 99% boundary layer thickness.

friction velocity U_e^+ over lower and higher ranges of Re_θ, respectively. Also shown are experimental measurements (Österlund 1999), a compendium of results from DNS (see Schlatter and Örlü 2010) and the semi-empirical relation given by Nagib et al. (2007) as "Coles-Fernholz 2"

$$\left(U_e^+\right)_{CF} = \frac{1}{\kappa} \log\left(Re_\theta\right) + C, \qquad \kappa = 0.384, \quad C = 4.127. \tag{3.21}$$

In Figure 3.3, U_e^+ at our lowest $Re_0 = 16 \times 10^3$ ($Re_\theta \approx 10^3$) agrees reasonably well with both experiment and DNS despite the fact that in this range our first grid point is inside or close to the viscous sublayer where our wall model in region II is probably least accurate. Across our whole Re_θ range Coles-Fernholz 2 gives a reasonable representation of our LES results, which can be considered predictions past the largest experimental value of Figure 3.4, $Re_\theta = 4 \times 10^4$. We remark that the small but systematic discrepancy in U_e^+ between the present LES and experiment evident in Figure 3.3 is in fact rather smaller than the spread in the Schlatter and Örlü (2010) compilation of DNS at somewhat lower Re_θ.

It is evident from Figure 3.4 that for some LES with Re_θ greater than about 10^8, the slope of U_e^+ versus $\log Re_\theta$ does not appear continuous with LES at other Re_θ and does not match the slope of the Coles-Fernholz 2 curve. This effect can also be seen in the Schlatter and Örlü (2010) DNS compilation of Figure 3.3. To investigate this, some LES at large Re_θ were done with longer domains (cases B16, C16, B18, and C18) as indicated by the small boxes in Figure 3.4. Some results are shown in Figure 3.5 where it can be seen that substantially longer domains, up to $L_x = 144\delta_0$, appear to give an averaged slope consistent with the continuous curve of (3.21). We remark that the slope of the continuous function $U_e^+(Re_\theta)$ is Re_θ^{-1} times the slope of U_e^+ versus $\log(Re_\theta)$ shown in the graphs, so that the discrepancy refers to a function $U_e^+(Re_\theta)$ with slope magnitude $\mathcal{O}(10^{-8}\text{–}10^{-12})$

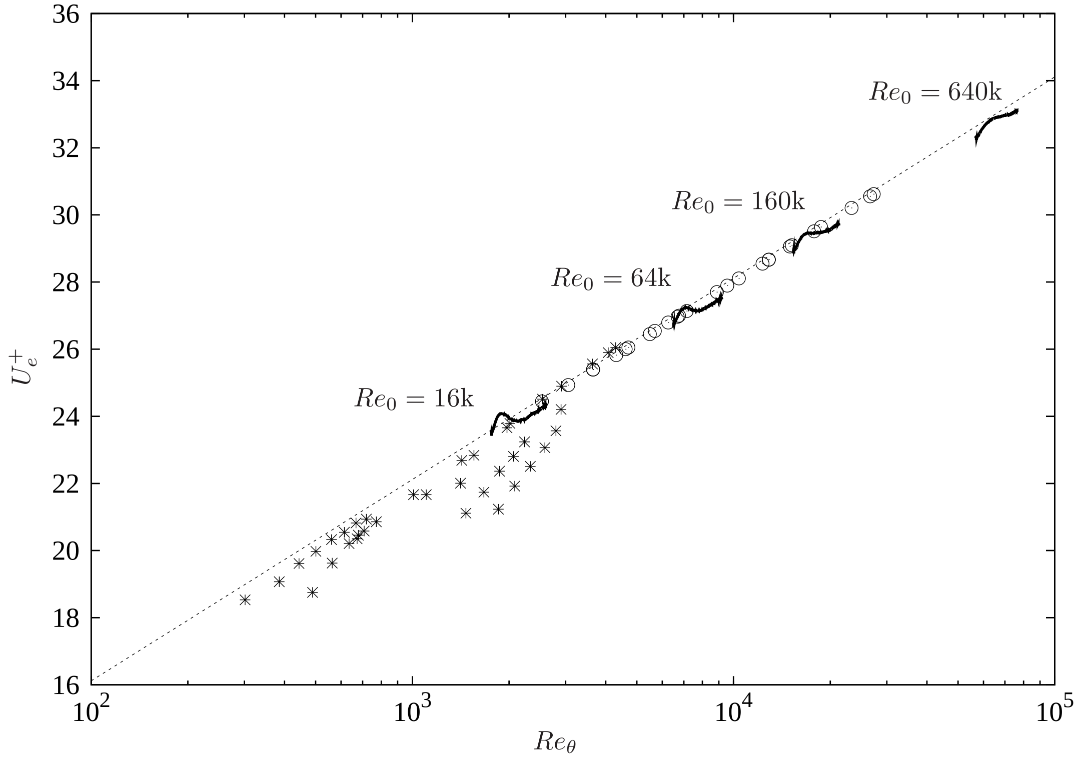

Figure 3.3. $U_e^+ \equiv U_\infty/u_\tau$ versus Re_θ up to $Re_\theta \approx 10^5$. Solid lines; current LES (cases; A1–A3 and A5), ○; Experiment (Österlund 1999). ∗; DNS compilation (Schlatter and Örlü 2010). Dashed-line; Coles-Fernholz 2 (Nagib et al. 2007)

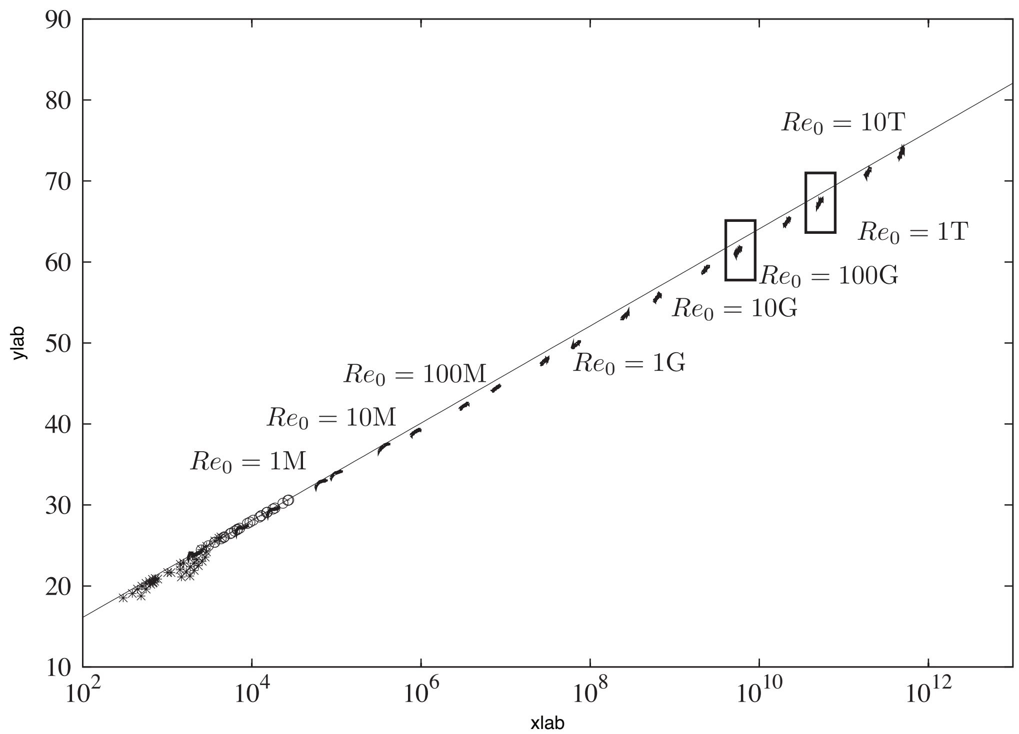

Figure 3.4. $U_e^+ \equiv U_\infty/u_\tau$ versus Re_θ up to $Re_\theta \approx 10^{12}$. Solid lines; current LES (cases; A1–A20), ○; Experiment (Österlund 1999). ∗; DNS compilation (Schlatter and Örlü 2010). Dashed-line; Coles-Fernholz 2 (Nagib et al. 2007)

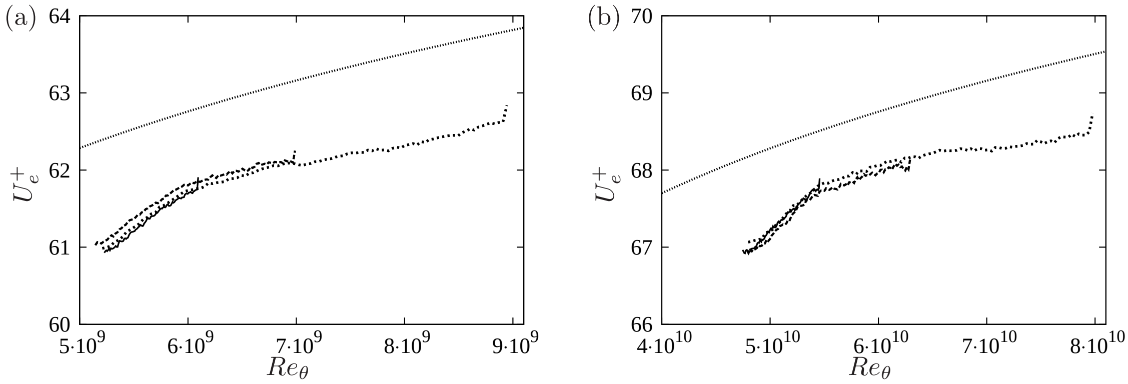

Figure 3.5. $U_e^+ \equiv U_\infty/u_\tau$ versus Re_θ with longer streamwise domains. Left(a): $Re_0 = 100$G, cases; A16, B16, and C16. (b) $Re_0 = 1$T, cases; A18, B18, and C18. Solid lines; $L_x/\delta_0 = 36$ (A16, A18), Dashed lines; $L_x/\delta_0 = 72$ (B16, B18), Doted lines; $L_x/\delta_0 = 144$ (C16, C18), thin dashed-lines; Coles-Fernholz 2 (Nagib et al. 2007)

over our large Re_θ range. In fact our maximum $Re_\theta = \mathcal{O}(10^{12})$ is perhaps too large for practical applications but illustrates the capability of the present wall-model LES. At our largest Re_θ the kinematic viscosity ν is approaching machine round off error. We expect that even larger Re_θ could be achieved with quad-precision arithmetic.

In addition to the A1–A20 LES at $(N_x, N_y, N_z) = (384, 64, 128)$, a set of 20 LES were done over the full Re_θ range of Figure 3.4 but at our lower resolution $(N_x, N_y, N_z) = (192, 32, 64)$. While these are not reported presently in detail we comment that these LES showed comparison with each matching A1–A20 LES similar to that depicted in Figures 3.1 and 3.2, and in Table 3.2.

Nagib et al. (2007) obtain a large Re_θ, $H - Re_\theta$ relation by combining the exact result

$$H = \frac{1}{1 - (C'/U_e^+)}, \qquad C' = \int_0^\infty \left(U_e^+ - u^+(z)\right)^2 d\left(\frac{z}{\Delta}\right), \tag{3.22}$$

with the empirical approximation $C' = 7.135 + \mathcal{O}(1/Re_\theta)$. This is shown in Figure 3.6 compared with the Schlatter and Örlü (2010) DNS compendium and with the present LES. Also shown are 3% deviation from (3.22). Given the dependence of the first of (3.22) on U_e^+, agreement between the LES and the asymptotic relation with the given C' is as expected. Nagib et al. (2007) point out that H does not appear to approach the traditional value $H = 1.3$ at large Re_θ. The shape factor may be viewed as the ratio of δ^*/δ_{99} to θ/δ_{99}, both of which decrease approximately as $1/\log(Re_\theta)$ when Re_θ increases. As the ratio of two small quantities, convergence in H from LES with increasing resolution can be expected to be slow at large Re_θ and this is reflected both Table 3.2, where the effect of resolution on H is larger than for other tabulated quantities and also in Figure 3.6. In particular the difference between case A16 and A16H is about 2% and it is clear that case A16H shows better agreement in both value and slope with the semi-empirical curve. The present LES may thus indicate approach to $H \to 1$ at gigantic Re_θ, but this is extremely slow.

3.3.5 Mean velocity profiles and flow visualization

Figure 3.7 shows mean velocity profiles in inner-scaling as $u^+ = \overline{u}(z^+)/u_\tau$ over a range of Re_θ. The log-relationship shown uses a value of the Kármán constant $(\overline{\mathcal{K}_1})_{\text{ave}} = 0.378$ which is the average of the dynamic values obtained over cases A1–A20. An additive constant $B = 4.08$ is from equation (3.15). It can be seen in Figure 3.7 that there is a drop off in u^+ near the virtual wall for the lower values of Re_θ. This is again the influence of a near-wall length-scale of order the cell size as discussed by Brasseur and Wei (2010). This effect is weaker at our larger Re_θ. Figure 3.8 shows mean velocity defect profiles, $U_e^+ - u^+$ in the outer coordinates, indicating good collapse across the boundary layer. The profiles are in good agreement with that of DeGraaff and Eaton (2000) at $Re_\theta = 31,000$. Taken together, Figures 3.3–3.8 show that the wall-model combined with the outer-scale LES captures the principal features of the ZPGFPTBL, in particular the wall-friction velocity u_τ and therefore the wall shear stress. This is despite the fact that both h_0^+ and the first LES point containing resolved-scale velocities, $h^+ = h_0^+ + \Delta_z^+/2$ for the staggered grid, may take extremely large values, for example, $h_0^+ \approx 3 \times 10^9$ and $h^+ \approx 3 \times 10^{10}$ at $Re_\theta = \mathcal{O}(10^{12})$. This could indicate that adequate modeling of the main physics of the log-layer is the key to successful LES of wall-bounded flows at very large Reynolds numbers.

Figures 3.9, 3.10 and 3.11 show contour plots of streamwise velocity, each plotted as u/U_∞ and each at a time instant during the particular LES indicated. The figures are not in proportion in x and z and each does not display the full domain height in the wall-normal direction. In Figure 3.9(a), (b) and perhaps (c) it can be observed that the large-scale structures at the inflow and after just downstream of the recycling plane show some degree of correlation, suggesting quasi-periodic behavior. For the LES case B4a shown in Figure 3.9(c), the recycling technique of Jewkes et al. (2011) was used in which the inlet velocity field that is generated as a rescaled version of the instantaneous velocity field at the recycling plane, is also subject to mirror-imaging about the wall-normal centerline of the inlet flow plane. This almost completely removes the spatially quasi-periodic effect in the overall LES. As shown in Table 3.3 for $Re_\theta \approx 2.5 \times 10^4$, one-point statistics show almost no discernible effect from either the use or non-use of mirror imaging in the recycling method or the recycling domain length. This, however, may not be the case for two-point or other correlation statistics not discussed presently.

Figure 3.10 shows the effect of resolution at $Re_\theta \approx 2.5 \times 10^4$. The three LES correspond to Table 3.2 and to Figures 3.1 and 3.2. The plots illustrate the dramatic effect of resolution in resolving turbulent scales yet the computed skin-friction and other parameters displayed in Table 3.2 are little different for the three different resolutions. The effect of Reynolds number over a large range is shown in Figure 3.11 where it is evident that, at a given distance from the wall as a fraction of the boundary-layer thickness, the velocity fluctuations decrease when scaled on U_∞. Contour plots of the instantaneous velocity defect $U_e^+ - u^+ \equiv (U_\infty - u)/u_\tau$ in an $x - z$ plane are shown in Figure

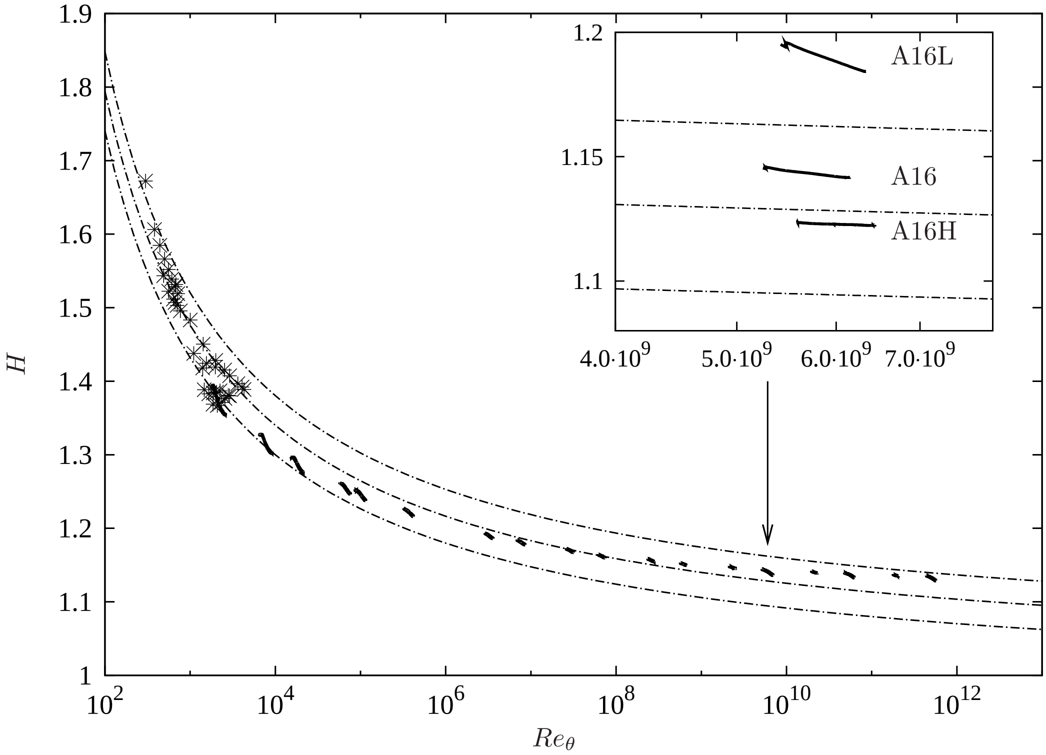

Figure 3.6. Shape factor $H = \delta^*/\theta$ versus Re_θ. Cases; A1 to A20 and A16L, A16H shown in inner plot. Solid lines; current LES, $*$; DNS compilation (Schlatter and Örlü 2010). Dashed-line; equation (3.22) with 3% error ranges (Nagib et al. 2007)

3.12. This corresponds to an instantaneous version of Figure 3.8. It may be observed that, unlike Figure 3.11, all four plots show somewhat similar color coverage suggesting that fluctuations, as well as the mean of Figure 3.8, show selfsimilarity in this scaling. There is, however, the impression that as Re_θ increases bottom to top in Figure 3.12, the spatial scale of the fluctuation changes somewhat. This is probably a result of two effects, first that the contour plot shows only the resolved and not the subgrid velocity field and second owing to the possible presence of long outer structures whose activity may be a function of Reynolds number. A study of the latter for the turbulent boundary layer is beyond the scope of the present work.

3.3.6 Kármán "constant" and the Coles wake-factor

The parameter $\mathcal{K}_1(x, y, t)$ defined in (3.13) can be interpreted as a Kármán-like constant. For plane channel flow Chung and Pullin (2009) found average values of $(\overline{\mathcal{K}_1})_{\text{ave}} \approx 0.37$ broadly independent of Re_τ. The present variation of the spanwise/time averaged values of $\mathcal{K}_1(x, y, t)$ as a function of Re_θ is depicted in Figure 3.13(a) which show a weak dependence on Re_θ over many decades. The results appear as "blobs" because each LES spans a range of Re_θ. We emphasize again that $\mathcal{K}_1(x, y, t)$ is calculated directly from the subgrid model near the wall and not from fitting a log-relationship to

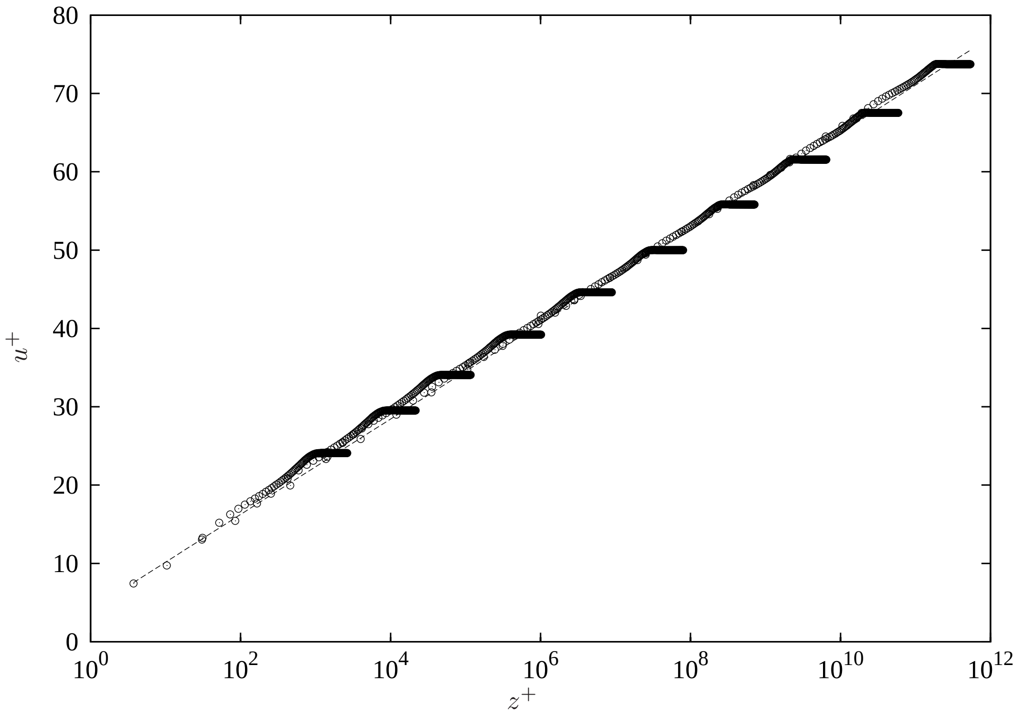

Figure 3.7. Mean velocity profiles $u^+ \equiv \overline{u}/u_\tau$ over a range of Re_θ taken at $x/\delta_0 \approx 24$; Cases shown are A1, A3, A6, A8, A10, A12, A14, A16, A18, and A20. Solid line; log relationship with $(\overline{\mathcal{K}_1})_{\text{ave}} = 0.378$, $B = 4.08$ (see equation (3.15))

mean-velocity profiles.

The Coles wake factor is a useful parameter characterizing the outer velocity profile. The wake parameter Π is defined from a universal profile fitted to the difference between the mean velocity and the logarithmic law (Coles 1956). Presently we calculate Π_{99} using (Nagib et al. 2007)

$$u^+ = \frac{1}{\kappa}\,\log y^+ + B + \frac{\Pi}{\kappa}\,\mathcal{W}\left(\frac{y}{\delta}\right), \tag{3.23}$$

where δ is the boundary layer thickness and κ is the Kármán constant. The function $\mathcal{W}(\xi)$ is a universal wake profile defined such that $\mathcal{W}(1) = 2$. We follow Nagib et al. (2007) and identify δ as the 99% boundary layer thickness δ_{99} obtained from the spanwise/time averaged mean velocity profile, approximate $\mathcal{W}(\delta_{99}/\delta) = 2$ and identify $\kappa = \overline{\mathcal{K}_1}$. Then a parameter Π_{99} can be calculated as

$$\Pi_{99} = \frac{\overline{\mathcal{K}_1}}{2}\left(0.99\,U_e^+ - \frac{1}{\overline{\mathcal{K}_1}}\,\log\delta_{99}^+ - B\right), \tag{3.24}$$

where, from (3.13), our effective value for B is given by (3.15). Values of Π_{99} calculated from the LES are shown on Figure 3.13(b) plotted versus Re_θ. At our "lower" Re_θ in the range 10^4–10^6 we find Π_{99} increases slowly (see also Figure 3.14 where the LES results are compared to experimental measurements) perhaps toward the asymptotic value $\Pi_{99} = 0.55$ recommended by Nagib et al. (2007)

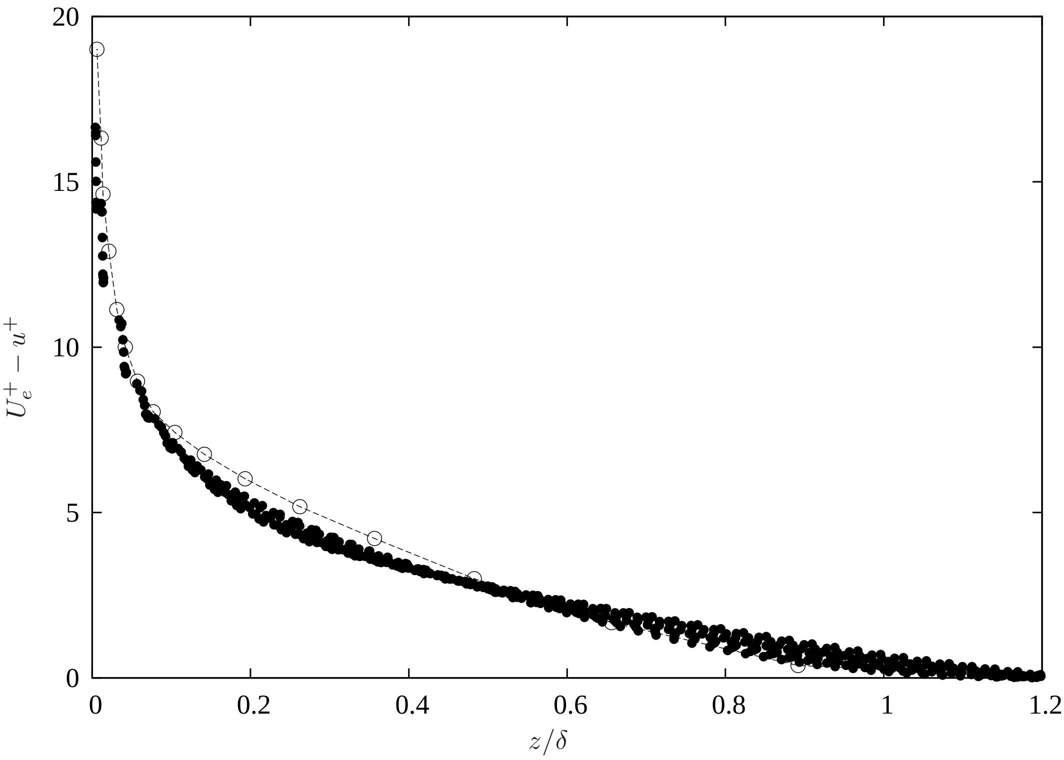

Figure 3.8. Mean velocity defect profiles over the same range of Re_θ as Figure 3.7. ○; Experiment at $Re_\theta = 3.1 \times 10^4$ (DeGraaff and Eaton 2000)

while remaining just below the statistical scatter of the experimental results shown in their Figure 8. At our larger Re_θ we find $\Pi_{99} \approx 0.5$ with a weak Re_θ dependence.

3.3.7 Turbulence intensity profiles

The turbulence intensity profiles for $\overline{u'^2}$ with three different scalings are shown in Figures 3.15 and 3.16 plotted against $\eta = z/\Delta$ where Δ is the Rotta-Clauser parameter. Figure 3.16 also shows $\overline{w'^2}$ with inner scaling. It seems clear that neither outer scaling (Figure 3.15(a)) nor mixed scaling (Figure 3.15(b)) provide satisfactory collapse. Inner scaling, however, provides reasonable collapse for both turbulence intensities across almost the whole plotted range of η in Figure 3.16. The collapse is not as good over the two grid points nearest the wall and we interpret this as a near-wall effect of the composite LES-wall model.

The outer collapse is consistent with a similarity model for the streamwise turbulence intensity in the ZPGFPTBL (Marusic et al. 1997, Marusic and Kunkel 2003). This model takes the form $u'^2/u_\tau^2 = F(z^+, Re_\tau)$ where $Re_\tau = \delta\, u_\infty/\nu$ is the Kármán number and δ, interpreted here as $\delta = \delta_{99}$ is the boundary layer thickness. This is related to Δ as $\Delta/\delta = H\, Re_\theta/Re_\tau$ which ratio is nearly constant as a function of Re_θ (not shown presently). In the outer part of the boundary layer the model becomes asymptotic to $u'^2/u_\tau^2 \sim -\log(z/\delta) \sim -\log(z/\Delta)$ consistent with the outer-length

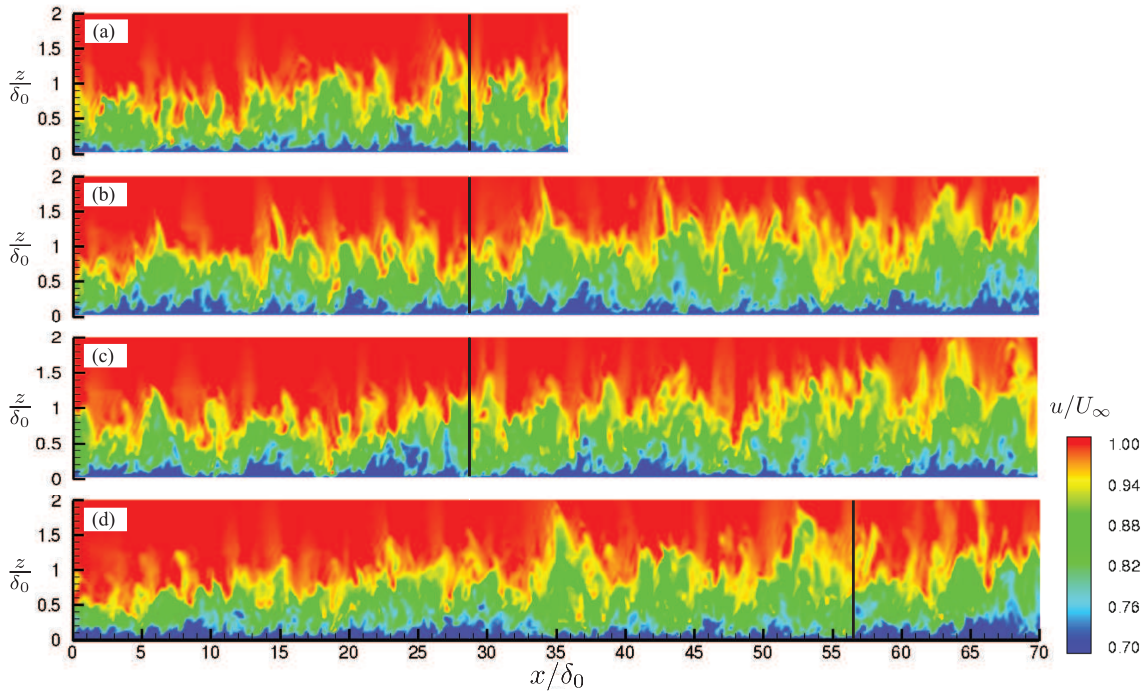

Figure 3.9. Contour plot of instantaneous streamwise velocity. Effect of x_{ref} position, domain size and inflow generation method. (a) case A4, (b) case B4, (c) case B4a, (d) case B4b. The vertical solid lines indicate the position of recycling plane. $Re_\theta = 1.9$–2.6×10^4 (short domain), –3.3×10^4 (long domains). Note that case B4a uses a mirror-image recycling technique (Jewkes et al. 2011).

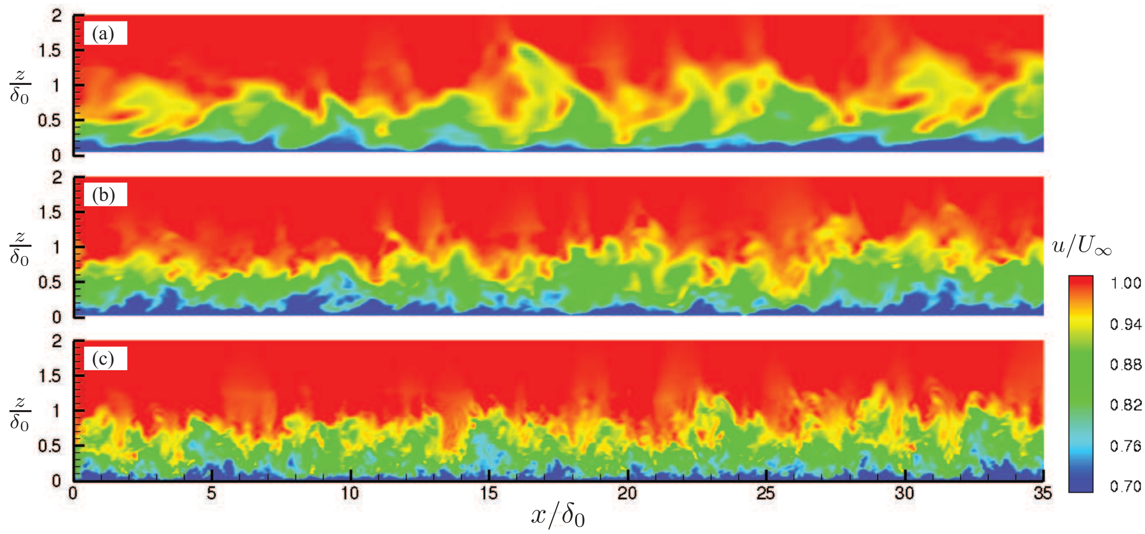

Figure 3.10. Contour plot of instantaneous streamwise velocity. Effect of resolution. (a) case A4L, (b) case A4, (c) case A4H. $Re_\theta = 1.9$–2.6×10^4. These plots correspond to Table 3.2.

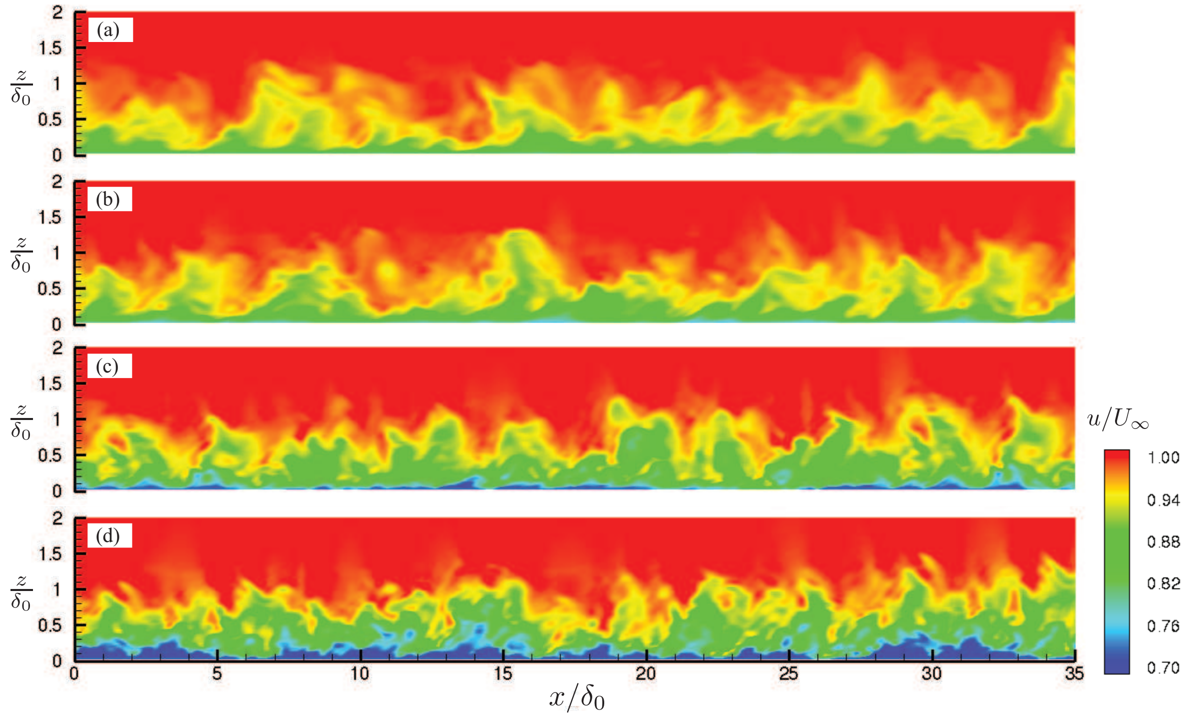

Figure 3.11. Contour plot of instantaneous streamwise velocity. Effect of Reynolds number. (a) A18:$Re_0 = 1T$, (b) A14:$Re_0 = 10G$, (c) A8:$Re_0 = 10M$ and (d) A3:$Re_0 = 160k$. Range of Re_θ; A18: 4.8–5.6 $\times 10^{10}$, A14: 5.6–6.8 $\times 10^8$, A8: 7.5–9.8 $\times 10^5$ and A3: 1.5–2.1 $\times 10^4$

scaling suggested by the present LES. In Figure 3.16(b) the LES collapse for $\overline{u'^2}/u_\tau^2$ is somewhat steeper than $-\log(z/\Delta)$. A specific comparison is shown in Figure 3.17 at the LES $Re_\tau = 1.1 \times 10^6$. Except for the two LES grid-points nearest the wall, the LES and the full similarity model show reasonable agreement. Also shown is data from the Surface Layer Turbulence and Environmental Science Test (SLTEST) site in the western desert of Utah (Metzger et al. 2007). The LES results falls within the error bars of the data over most of the region of overlap save the two nearest wall points.

3.4 Discussion

Experimental and semi-empirical, asymptotic scenarios for high-Reynolds-number, wall-bounded flows (Nagib et al. 2007, Monkewitz et al. 2007, Marusic et al. 2010b) appear to provide a reasonable representation of the present LES predictions of the skin-friction and shape factor at extremely large Reynolds numbers. For the mean velocity profile, the present LES reveals no selfsimilar state at very large Re_θ: two length scales, ν/u_τ and δ and two velocity scales, u_τ and U_∞ are always required to describe the streamwise velocity profile. Even though there exist quantitative discrepancies compared to experiment for the streamwise turbulence intensity (Figure 3.2(a)) one-

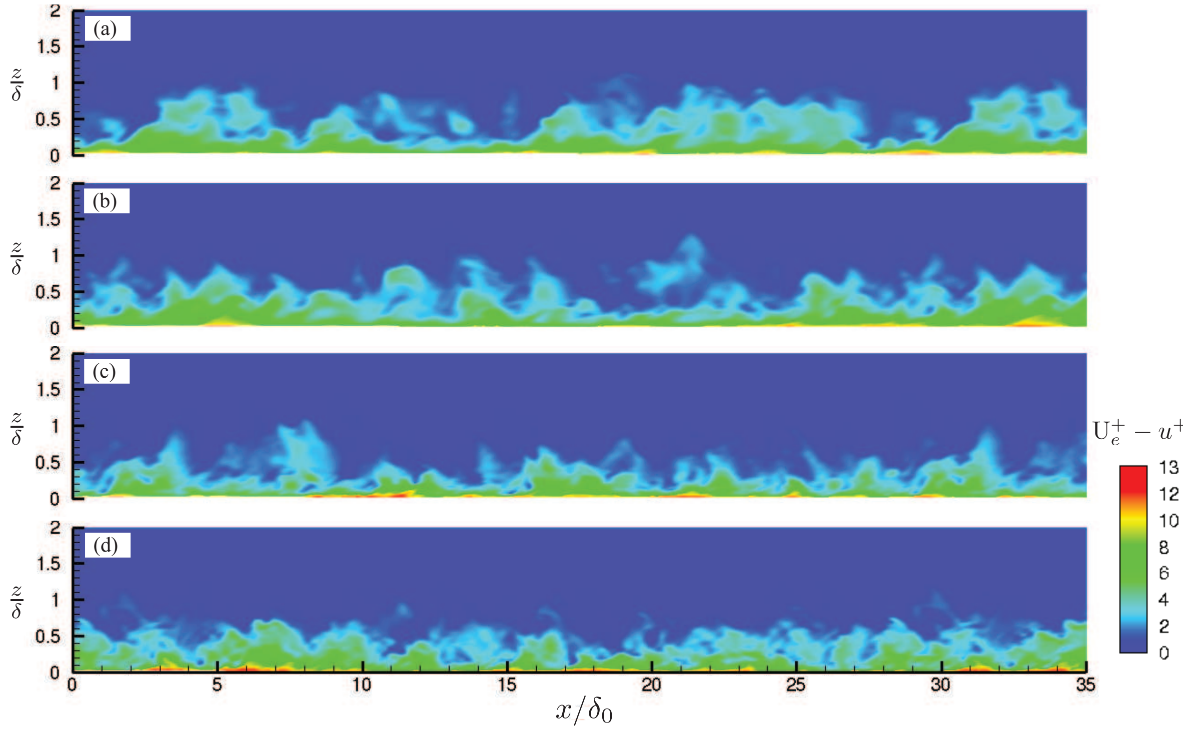

Figure 3.12. Contour plot of instantaneous velocity defect $U_e^+ - u^+$. Effect of Reynolds number. (a) A18:$Re_0 = 1T$, (b) A14:$Re_0 = 10G$, (c) A8:$Re_0 = 10M$, and (d) A3:$Re_0 = 160k$

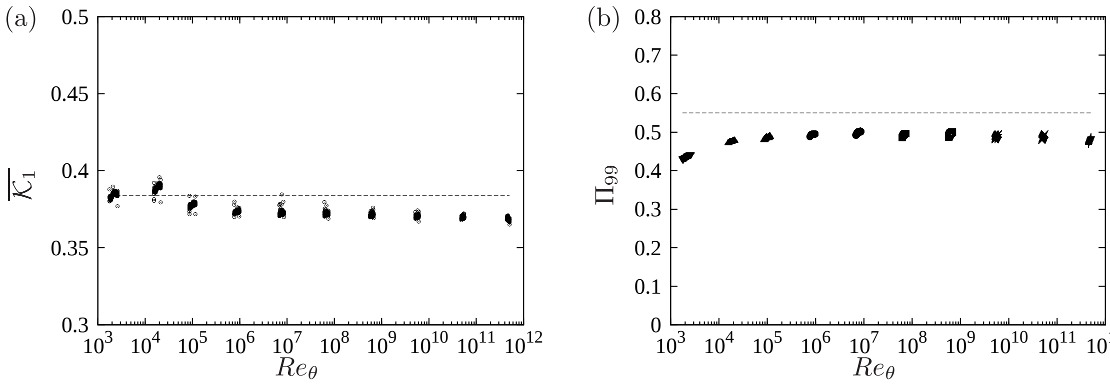

Figure 3.13. (a): Kármán "constant" $\overline{\mathcal{K}_1}$ calculated dynamically, (b): Coles wake factor Π_{99}. Horizontal lines are recommended values by Nagib et al. (2007), $\kappa = 0.384$, and $\Pi_{99} = 0.55$, respectively. Cases shown are A1, A3, A6, A8, A10, A12, A14, A16, A18, and A20.

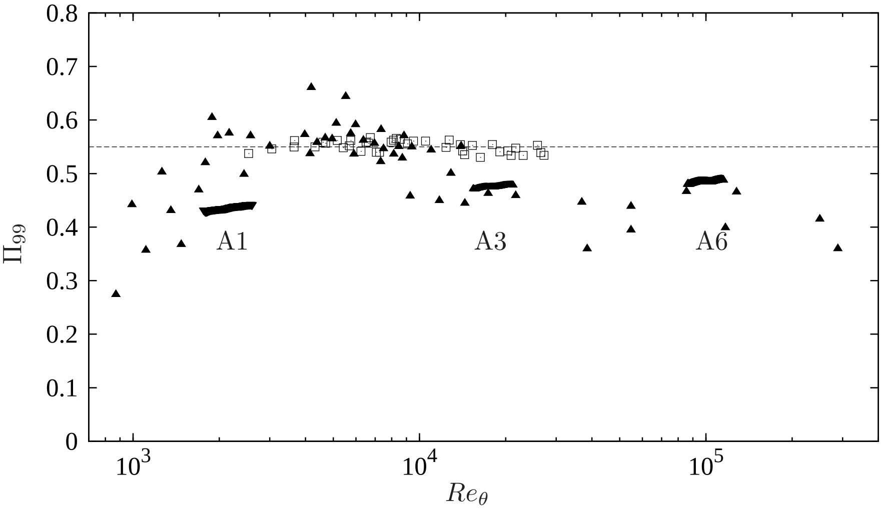

Figure 3.14. Coles wake factor Π_{99}. Horizontal line: $\Pi_{99} = 0.55$. Cases shown are A1, A3, and A6. Experiments: □; Österlund (1999), ▲; Cole (private communication)

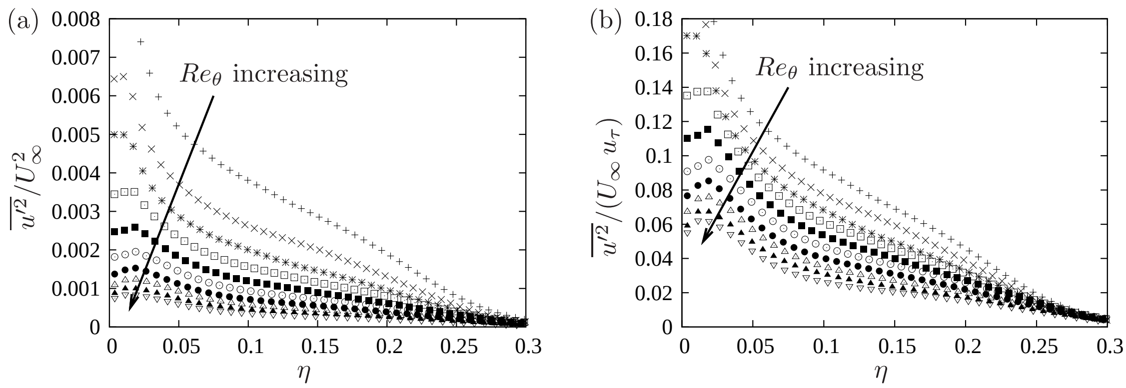

Figure 3.15. Streamwise velocity fluctuation. (a) Outer scaling, $\overline{u'^2}/U_\infty^2$ versus $\eta \equiv z/\Delta$. (b) Mixed scaling, $\overline{u'^2}/(U_\infty\, u_\tau)$ versus η. Arrows indicate increasing Re_θ. +; A1, ×; A3, ∗; A6, □; A8, ■; A10, ○; A12, ●; A14, △; A16, ▲; A18, ▽; A20. Data are taken at $x/\delta_0 \approx 24$ for each case.

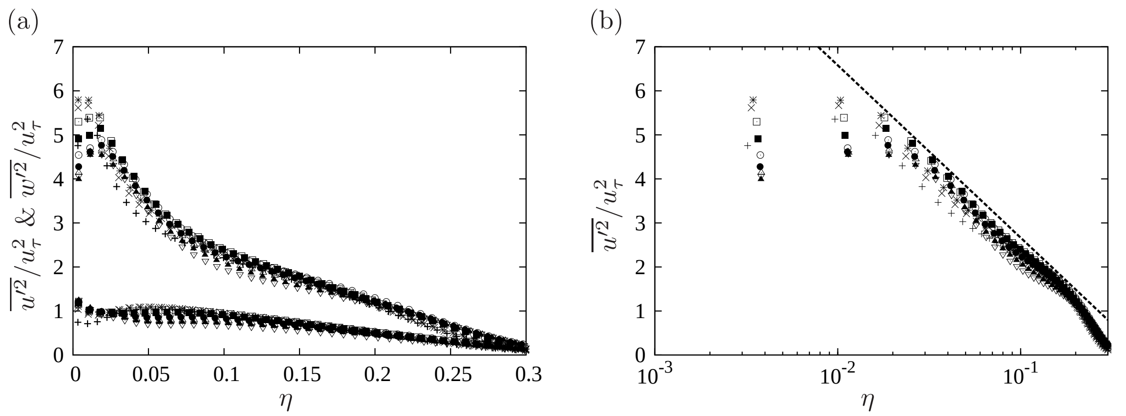

Figure 3.16. Streamwise and wall-normal velocity fluctuation. Inner scaling (a) $\overline{u'^2}/u_\tau^2$ and $\overline{w'^2}/u_\tau^2$ versus $\eta \equiv z/\Delta$. (b) $\overline{u'^2}/u_\tau^2$ in linear-log coordinates. Dotted line; $-\log(z/\Delta)$. Symbols for streamwise velocity fluctuation are as in Figure 3.15.

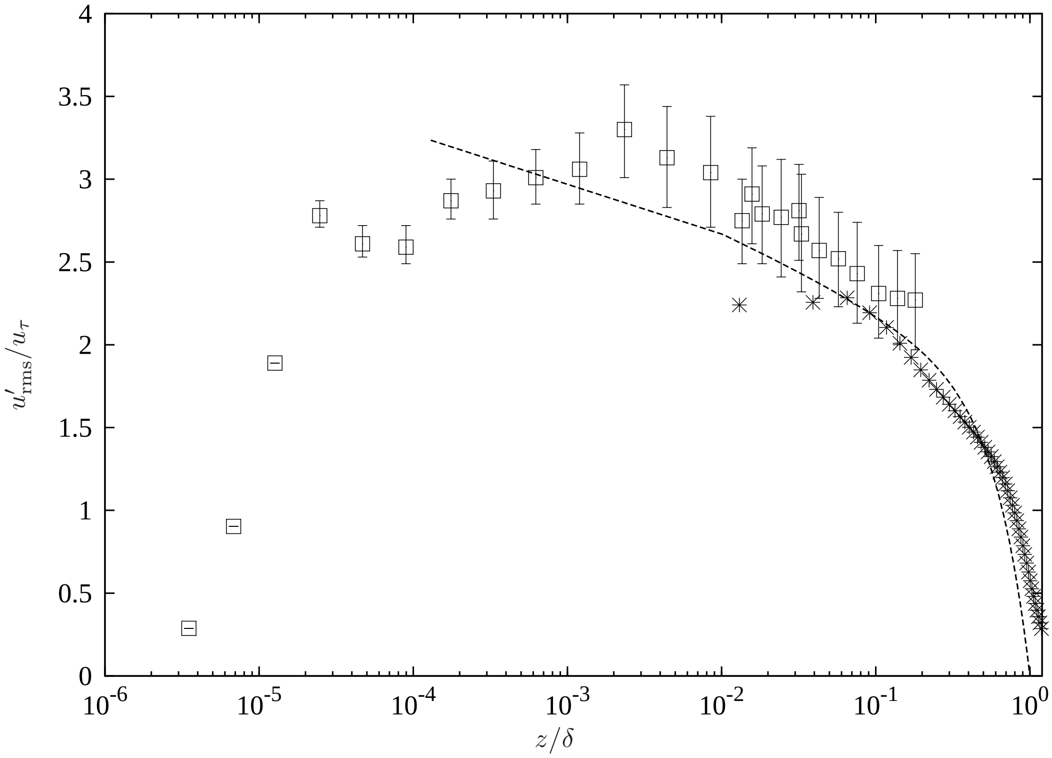

Figure 3.17. Streamwise root-mean square fluctuation. $*$; Case A9: $Re_0 = 40M$ at $Re_\tau = 1.1 \times 10^6$ ($Re_\theta = 3.4 \times 10^6$). $\Box$ with error bar; SLTEST data at $Re_\tau = 7.8 \times 10^5$ (Metzger et al. 2007). Dashed line: similarity model (Marusic et al. 1997, Marusic and Kunkel 2003)

point, second-order turbulence statistics obtained from the LES, nonetheless appear to collapse reasonably over almost all of the boundary layer thickness δ represented in the LES on one velocity scale, u_τ, and one length scale either δ or the Rotta-Clauser parameter Δ. This collapse, however, is not expected to be valid very near the wall, perhaps $z/\Delta < 0.01$, which is inaccessible to the present LES.

This last result has interesting implications for what is traditionally viewed as the smooth-wall ZPGFPTBL. Consider $Re_\theta \to \infty$ in each of three conceptual limits

(a) the streamwise distance x and U_∞ are fixed and $\nu \to 0$,

(b) $x \to \infty$ while U_∞ and ν are fixed,

(c) x and ν are fixed while $U_\infty \to \infty$ but the flow remains incompressible.

Assuming that the LES trend, that turbulence intensities over the outer boundary layer scale on u_τ, continues for $Re_\theta > 10^{12}$, then since $1/U_e^+$ decreases monotonically, this indicates that the turbulence intensity as a fraction of U_∞ expires in the limit $Re_\theta \to \infty$ over almost all the boundary layer. In other words, the outer part of the smooth-wall ZPGFPTBL asymptotically relaminarizes at sufficiently large Re_θ. This is consistent with the similarity model where it can be shown that the wall-normal integral of equation (8) of Marusic et al. (1997), expressed as the the average u'^2/u_τ^2 over the boundary layer thickness, approaches a finite value when $Re_\tau \to \infty$.

The preceding discussion does not include the effect of the near-wall peak in u' and a possible second outer peak. While there is some evidence for the presence of a second or outer peak, for example, in the SLTEST data shown in Figure 3.17 and in superpipe experimental data (Morrison et al. 2004), its wall-normal position appears to be a decreasing fraction of δ with increasing Reynolds number. For pipe flow Morrison et al. (2004) find $y_p/R \sim Re_\tau^{-1/2}$ where y_p is the wall-normal position of the second peak and R_τ is the Kármán number based on the pipe radius R. The inner peak appears to remain within the buffer-layer at $z^+ \sim 15$. Two estimates for the magnitude of the inner peak are $u'_{\max}/u_\tau = 1.86 + 0.12 \log Re_\theta$ (Metzger and Klewicki 2001) and $(u'_{\max}/u_\tau)^2 = 4.84 + 0.467 \log Re_\tau$ (Hutchins et al. 2009) (natural logs). If one uses (3.21), then the first of these gives $u'_{\max}/U_\infty \to 0.047$, $Re_\theta \to \infty$. If it is further assumed that $\Delta/(H\,\delta)$ approaches a finite limit when $Re_\theta \to \infty$, then the second expression, together with (3.21) gives $u'_{\max}/U_\infty \to 1/(\log Re_\theta)^{1/2}$ and is asymptotically zero.

The above suggests two turbulent boundary layers. The first is an inner, near-wall layer containing one and perhaps two peaks in streamwise turbulence intensity, whose thickness is unknown but probably decreases as a fraction of δ when Re_θ increases. The second is an outer layer which is perhaps no more than the free-stream shadow of the inner layer, in which the turbulence decays asymptotically. This is consistent with the composite inner–outer model of Marusic and Kunkel (2003) and Marusic et al. (1997). The infinite Re_θ limit would then be effective slip flow in the sense that, at fixed finite $z/\delta(x)$, $0 < z/\delta(x) \leq 1$, $\overline{u}/U_\infty \to 1$ while for any fixed $z/\delta(x)$, $z_p/\delta(x) < z/\delta(x) \leq 1$, where z_p/δ is the location of a possible outer peak or plateau in $\overline{u'^2}/u_\tau^2$, then $\overline{u'^2}/U_\infty^2 \to 0$. This limit would not preclude finite dissipation when $Re_\theta \to \infty$. This is strictly for the smooth-wall case with zero-pressure gradient. The limits (a) and (c) would be affected by surface roughness of a given length scale, but perhaps not the limit (b) since $l^+ \equiv \nu/u_\tau$ increases with increasing x. For a strictly smooth wall, a straightforward calculation using (3.21) shows that the drag on a flat plate of length x is zero for limit (a) but unbounded for limits (b) and (c).

A further estimate of interest is the scaling of some norm $||u'||$ of the streamwise turbulence intensity with Re_θ. Again we consider a smooth wall (in the limit (b) to avoid the effect of roughness) and will take a nominal norm $||u'||/u_\tau \approx 2.5$ as the streamwise turbulence intensity at 1% boundary layer thickness suggested by Figure 3.16. An alternative estimate based on an average over the whole boundary layer thickness could also be used (e.g., equation (8) of Marusic et al. (1997)). This would affect the quantitative but not the qualitative character of the following argument. Again using the Nagib et al. (2007) expression (3.21) gives, together with $||u'||/u_\tau = 2.5$,

$$Re_\theta = 10^\beta, \qquad \beta = 0.4343\,\kappa\left(\frac{2.5}{||u'||/U_\infty} - C\right), \tag{3.25}$$

for the value of Re_θ corresponding to a given boundary-layer intensity norm $||u'||/U_\infty$. For $||u'||/U_\infty \approx 0.033$, (3.25) gives $Re_\theta \approx 10^{12}$. Assuming terrestrial conditions and $U_\infty = 40\mathrm{ms}^{-1}$ in air at room temperature this would require a plate length of about $10^{8.5}$m at which station $\theta \approx 10^{4.7}$ m and viscous length scale $l^+ \approx 10^{-5}$ m.

Chapter 4

Inner-layer predictions for the flat-plate turbulent boundary layer combining a predictive wall-model with LES

4.1 Background

It has long been known that wall-bounded turbulent flows at moderate to large Reynolds number contain an extremely large range of eddy length scales. For the flat plate turbulent boundary layer, one measure of this is the friction Reynolds number $Re_\tau \equiv u_\tau\, \delta/\nu$ where $u_\tau \equiv \sqrt{\tau_w/\rho}$ is the friction or inner velocity scale and $\delta, \tau_w, \nu, \rho$ are the boundary layer thickness, wall shear stress, fluid kinematic viscosity and density, respectively. Recent experimental studies at large Re_τ, however, have suggested that δ is not itself the largest dynamically active length scale in the zero-pressure gradient turbulent boundary layer. Convincing evidence (Ganapathisubramani et al. 2003, del Álamo and Jiménez 2003, Tomkins and Adrian 2003, Kim and Adrian 1999, Hutchins and Marusic 2007b,a) indicates that there exists very large scale motions (VSLMs) or "superstructures" with scales of order 15–20δ within the outer logarithmic part of the turbulent boundary layer. It is hypothesized that these elongated structures are slightly inclined to the horizontal and may be accompanied by large-scale, counterrotating, roll-like modes; see Mathis et al. (2011) for a summary and discussion.

It has also been highlighted that the dynamical influence of the large-scale events extends to the wall where they affect the small-scale, near-wall fluctuations, in a significant way. The studies of Abe et al. (2004) and Hutchins and Marusic (2007a) have clearly indicated that the large-scale motions are felt all the way down to the wall, as a strong imprint (consistent with the attached eddy hypothesis of Townsend (1976)). Mathis et al. (2009) have shown that their influence is not simply a superposition, but also that these large-scale motions, associated with the log-region, substantially amplitude modulate the near-wall small-scale structures. In their work Mathis et al.

(2009) developed a mathematical tool to quantify the degree of modulation.

Marusic et al. (2010a) and Mathis et al. (2011) incorporated these ideas into an algebraic model that enables the prediction of near-wall statistics of turbulent streamwise velocity fluctuations using a single-point log-layer time-series signal as an input. Further details on this model are given in §4.2.1.

Investigations using either direct numerical simulation (DNS) or large-eddy simulations (LES) of near-wall turbulence – for long-domain boundary layers at the largest laboratory Reynolds numbers presently achievable or for atmospheric boundary layers – have been hampered owing to the presence of small yet dynamically important anisotropic near-wall structures. The requirements for resolving both near-wall small eddies and large-scale structures severely limit the range of Re_τ accessible by both DNS and wall-resolved LES (in which near-wall structures are at least partially resolved). A further requirement is the capability of capturing variations $\sim \mathcal{O}(\log(Re_\tau))$ in some important quantities, such as the wall skin-friction coefficient for smooth-wall flow. An alternative to wall-resolved LES is the use of wall-models specifically constructed to represent the effect of near-wall anisotropic eddies (see Piomelli (2008) for a review). Whilst a principal objective of wall-modeled LES is to avoid the necessity of explicit resolution of near-wall turbulent structures, this comes with the price that some flow properties — such as the detailed near-wall statistics and their dependence on the presence of large-scales in the outer flow — cannot be investigated directly. We address this issue presently.

The main purpose of the work described in this chapter is to examine the near-wall region of zero-pressure gradient turbulent boundary layer (ZPGTBL) using a combination of wall-modeled LES coupled to a predictive wall model (Marusic et al. 2010a, Mathis et al. 2011) at Reynolds numbers which have been not yet accessible, by either numerical simulation or laboratory experiment. Specifically we use the LES/wall-model described in previous chapters (see also Inoue and Pullin 2011) to provide the large-scale log-region velocity time series as the input to the predictive near-wall model of Marusic et al. (2010a) and Mathis et al. (2011). The combined LES and predictive inner–outer model potentially extends the LES capability to high Reynolds numbers, spanning the gap between laboratory turbulent boundary-layers and atmospheric surface-layers. This allows us to address some open questions regarding the large-scale effects on the near-wall statistics and their dependency on Reynolds number. For instance, the existence of an outer peak in the turbulent fluctuations profile remains controversial, and it would be only evident at very high Reynolds number (Alfredsson et al. 2011).

Brief accounts of both the predictive inner–outer model and subgrid-scale model employed in the current LES are described in §4.2. This is followed by an account of the LES in §4.3. Discussion of results is found in §4.4 and §4.5.

4.2 Wall-model description

From the preceding discussions it should be clear that two different "wall models" are being considered here. Since these models are independent and have different functions, for the purposes of clarity we distinguish these as follows. Also see Figure 4.1. The first is the predictive inner–outer wall model of Mathis et al. (2011), described in §4.2.1. We will refer to this as the "PIO wall model". The second is the "LES wall model", described and demonstrated in §3.2. The purposes of this LES model is to avoid the necessity of resolving the inner wall layer while still providing an estimation of the wall friction velocity. Also, it gives a boundary condition for the outer-flow LES at a "virtual" wall located at a fixed height from the actual wall. In the present work, the LES provides a velocity signal as an input to the PIO wall model. It should be emphasized that the LES wall-model is independent of and does not require feedback from the PIO wall model, and vice versa.

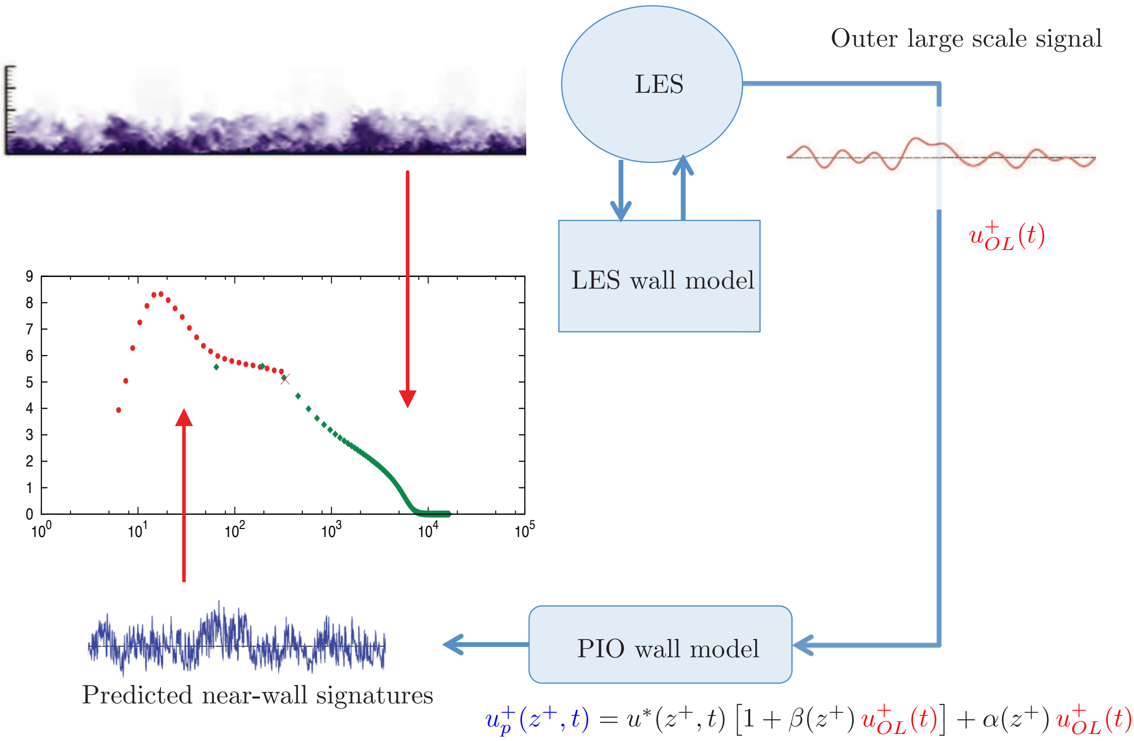

Figure 4.1. Schematic description of two "wall models"

4.2.1 Predictive inner–outer model

Marusic et al. (2010a) and Mathis et al. (2011) proposed a quantitative model to reconstruct the fluctuating streamwise velocity field, $u_p^+(z^+, t)$, in the near-wall region, based on a single point observation of the large-scales in the log-region, $u_{OL}^+(t)$:

$$u_p^+(z^+, t) = u^*(z^+, t)\left[1 + \beta(z^+)\, u_{OL}^+(t)\right] + \alpha(z^+)\, u_{OL}^+(t), \tag{4.1}$$

where u_p^+ is the predictive time-series at z^+. The time-series u^* represents a statistically "universal" signal of the small-scales at z^+ that would exist in the absence of any inner–outer interactions. The quantities $\alpha(z^+)$ and $\beta(z^+)$ are, respectively, the superposition and modulation coefficients. The parameters u^*, α and β are determined experimentally during the calibration of the model, and are hypothesized to be Reynolds number independent. Note that the model in equation (4.1) consists of two parts. The first part of the equation models the amplitude modulation effect of the small-scales (u^*) by the large-scale motions (u_{OL}^+). The second term models the linear superposition of the large-scale events felt at a given wall-normal position z^+. In order to apply (4.1), u_τ must be known.

The only required input signal to the model is the large-scale fluctuating velocity signal from the log-region, $u_{OL}^+(t)$, taken at the normalized wall-normal position where the calibration experiment was conducted, which is $z_O^+ = \sqrt{15\, Re_\tau}$, the approximate geometric center of the log-region (Mathis et al. 2009). The large-scales signal is obtained by filtering first the raw signal to retain only length scales greater than a streamwise wavelength $\lambda_x^+ > 7000$ (using Taylor's hypothesis). Then, a spatial shift is applied to account for the mean inclination angle of the large-scale structures. The final step is to retain the Fourier phase information of the large-scale component used during the calibration of the model. For further details about the model, see Mathis et al. (2011).

Here the distance from the wall, z, and the streamwise velocity component, u, are normalized by inner-scale variables so that $z^+ \equiv z\, u_\tau/\nu$ and $u^+ \equiv u/u_\tau$. Also, u^* is normalized against u_τ.

4.3 Simulation details

Presently, we use the LES of the zero-pressure gradient, smooth-wall, flat plate, turbulent boundary layer, described in Chapter 3, to provide a rake of velocity time series obtained at $z^+ \approx z_O^+$ as the raw signal input u_O^+ to the PIO wall model, that is, the signal from which $u_{OL}^+(t)$ is obtained. Equation (4.1) then supplies a time series $u_p^+(z^+, t)$ at each z^+ from which both wall-normal variation of several moments of the probability-density function of the streamwise fluctuating velocity can be obtained as well as longitudinal spectra (using a local Taylor hypothesis) within a region that is inaccessible to the LES.

Case	N_x	N_y	N_z	Re_θ	$Re_{\tau,99}$	δ_{99}	u_τ	ν	Δ_y^+	dt	T^+
7.3k-θ	768	64	128	1.97e4	6.89e3	1.67	0.0338	8.18e-6	1.29e2	0.08	1.44e6
13.6k-θ	768	64	128	3.60e4	1.25e4	1.63	0.0321	4.20e-6	2.38e2	0.08	2.07e6
19k-θL	768	64	128	4.73e4	1.62e4	1.61	0.0313	3.12e-6	3.14e2	0.08	2.08e6
19k-θH	1152	96	192	4.73e4	1.60e4	1.60	0.0313	3.14e-6	2.08e2	0.06	1.41e6
62k-τ	1728	144	288	1.71e5	5.44e4	1.31	0.0283	6.84e-7	5.75e2	0.04	8.72e5
100k-τ	2304	192	384	3.22e5	9.96e4	1.47	0.0271	3.99e-7	7.08e2	0.03	1.21e6
200k-τ	3072	256	512	6.65e5	2.00e5	1.49	0.0257	1.92e-7	1.05e3	0.015	1.00e6

Table 4.1. Simulation parameters and integral quantities. Inflow velocity is a rescaled velocity field taken from $x_{\text{ref}} = 0.8L_x$. $(L_x/\delta_0, L_y/\delta_0, L_z/\delta_0) = (72, 6, 4)$. $x_{\text{stat}} = 0.75L_x$. Case 62k-$\tau$, the velocity signal was taken from $x_{\text{stat}} = 0.45L_x$. $Re_\theta = U_\infty \theta/\nu$ and θ is the momentum thickness. $Re_{\tau,99} = u_\tau \delta_{99}/\nu$ and δ_{99} is the 99% boundary layer thickness. δ_c is the boundary layer thickness defined in Perry et al. (2002). dt is a time step size; $T^+ \equiv T\, u_\tau^2/\nu$ is the normalized time interval over which the velocity signal was obtained.

Case	Re_θ	S	$Re_{\tau,c}$	$Re_{\tau,99}$	$\overline{\mathcal{K}_1}$	B
7.3k-θ	1.97e4	29.6	7.19e3	6.89e3	0.397	4.38
EXP	1.96e4	29.3	7.34e3			
13.6k-θ	3.60e4	31.2	1.34e4	1.25e4	0.389	4.25
EXP	3.60e4	30.6	1.36e4			
19k-θL	4.73e4	31.9	1.77e4	1.62e4	0.386	4.21
19k-θH	4.73e4	31.9	1.85e4	1.60e4	0.389	4.25
EXP	4.72e4	31.4	1.88e4			
62k-τ	1.71e5	35.3	6.43e4	5.44e4	0.382	4.15
EXP*	1.56e5	35.8	6.20e4			
100k-τ	3.22e5	36.9	1.20e5	9.96e4	0.381	4.12
200k-τ	6.65e5	38.9	2.42e5	2.00e5	0.386	4.21

Table 4.2. Reynolds number and S-factor for each LES and corresponding experiments (Mathis et al. 2009, 2011, Oweis et al. 2010, Winkel et al. 2012). S-factor; $S \equiv U_\infty/u_\tau$. $Re_{\tau,c} = u_\tau \delta_c/\nu$ is a Reynolds number based in boundary layer thickness δ_c. Kármán constant $\overline{\mathcal{K}_1}$ from (3.13) and an additive constant B from (3.15)

4.3.1 LES performed

The present LES, summarized in Table 4.2, were designed to match experimental conditions reported (Mathis et al. 2009, 2011) based on $Re_\theta = \theta U_\infty/\nu$, where θ is the local momentum thickness and U_∞ is the free-stream velocity. The grid is uniform, $\Delta_x = \Delta_y = 3\Delta_z$, throughout the simulation domain. The raised wall is at $h_0 = 0.18\,\Delta_z$ for all LES independent of resolution. To capture the physics of long large-scale structures, we use long streamwise domains with $L_x/\delta_0 = 72$, where δ_0 is the inlet boundary-layer thickness. LES were performed in a domain $(L_x/\delta_0, L_y/\delta_0, L_z/\delta_0) = (72, 6, 4)$. The LES provided a set of N_y velocity-time signals $u^+_{OL}(t)$, each at $z^+ = z^+_O$, across the spanwise extent of the LES domain. Since z^+_O did not fall on a grid point, fourth-order interpolation was used.

It should be noted that grid resolutions here are chosen such that z^+_O will be located at approximately $z_O \approx 5\,\Delta z/2$ (third wall-normal grid point) so as to minimize the effect of the underresolved region close to the virtual wall where the LES wall-model provides a slip velocity as a boundary condition. An exception is case 19k-θL whose results show some effect of resolution (see Figure 4.8). Since z^+_O is fixed in inner scaling, then with the present uniform-grid LES and with a maximum of order 400 grid-points in the wall-normal direction this requirement limits presently attainable values of Re_τ, for the application of the current LES combined with the PIO wall model, to $Re_\tau = 2.0\times10^5$. We will subsequently refer to two sets of LES as intermediate (7.3k-θ, 13.6k-θ, 19k-θL,H of Table 4.1) and large (62k-τ, 100k-τ, 200k-τ) Reynolds number, respectively.

Each LES was run for 3–4 free-stream particle transit times through the domain, until statistical steady state was achieved, prior to the commencement of data sampling to calculate both time-averaged quantities and also the required velocity time series. Values of the LES sampling time period, $T^+ \equiv T\,u_\tau^2/\nu$, normalized on the wall-unit time ν/u_τ^2 are shown in Table 4.1, which also lists some integral quantities. We note that the LES does not resolve the viscous, wall-time scale ν/u_τ^2.

The time series as input to the PIO model were obtained by sampling at every LES time step, Δt. Since for the present LES, $\Delta x = 3\,\Delta z$, then taking $\lambda_x^+ \equiv \Delta x\,u_\tau/\nu$ and $\Delta z = \delta/N_\delta$, where N_δ is the number of grid points across the boundary layer, then gives, for the present LES, $\lambda_x^+ = 3\,Re_\tau/N_\delta$. Typically $N_\delta \approx N_z/3$ and the values displayed in Table 4.1 then show that $\lambda_x^+ \leq 7000$ for the present LES as required by the PIO model. It should also be noted that the inflow generation scheme of Lund et al. (1998) combined with the mirroring method proposed by Jewkes et al. (2011) was used for all LES. The other boundary conditions follow §3.3.

4.3.2 Skin friction and mean velocity profiles

In Chapter 3 we used the notation $U_e^+ = U_\infty/u_\tau$. Presently and subsequently we will change to the S-factor notation, $S = U_\infty/u_\tau$ in order to be consistent with Mathis et al. (2009, 2011) and other papers of the University of Melbourne high-Reynolds-number group. The S-factor variation versus

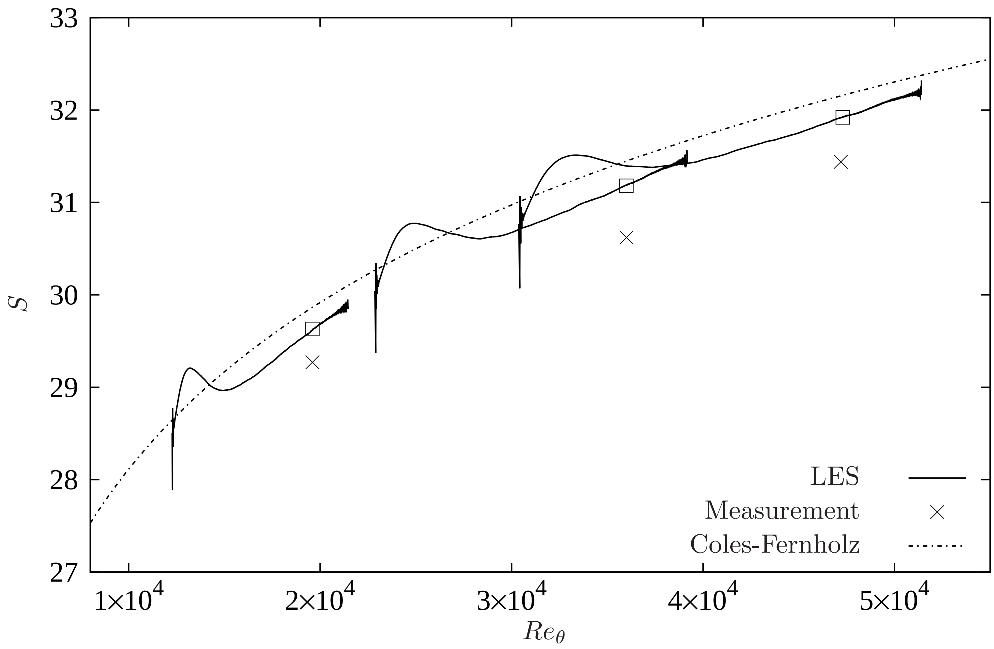

Figure 4.2. Reynolds number dependency of the S-factor for cases 7.3k-θ, 13.6k-θ, and 19k-θH. Solid lines; LES results, each line corresponds to each simulation case. □: locations where the velocity time series is taken. ×: corresponding experimental measurements (Mathis et al. 2011). Dot-dashed line: Coles-Fernholz relation (Nagib et al. 2007)

Re_θ along the streamwise direction for intermediate Reynolds number are shown in Figure 4.2. Also shown are experimental measurements (Mathis et al. 2011) and the semi-empirical Coles-Fernholz relation (Nagib et al. 2007). The wall-friction velocity u_τ and therefore the wall shear stress are provided directly from the ODE incorporated in the LES wall model. The S-factor profiles show a hill or bump after the inlet, also seen in DNS studies (Simens et al. 2009), which is perhaps the effect of nonequilibrium following inlet as a result of the recycling procedure. Note that the rake of velocity time series is taken well downstream of the hill where the effect of the inflow generation method is not visible. Our results overestimate the S-factor of the experimental measurements by about 1.5%. Meanwhile the Coles-Fernholz gives a reasonable representation of the LES variation of $S(Re_\theta)$ across those sections of our Re_θ range, where the boundary layer appears to be in equilibrium.

It is evident from Table 4.1 that there are small but systematic discrepancies in Re_τ between the present LES and experiment at matched Re_θ. It is well known that the boundary layer thickness, δ_{99}, is a poorly conditioned quantity as it depends on the measurement of a small velocity difference. As an alternative, a Reynolds number $Re_{\tau,c} \equiv \delta_c\, u_\tau/\nu$ based on another definition of boundary layer thickness, δ_c, is also shown. A method for determining δ_c can be found in Perry et al. (2002). It is assumed that the mean velocity profile is described by the law of the wall and law of the wake given by equation (4.6) of Perry et al. (2002). Values of $Re_{\tau,c} \equiv \delta_c\, u_\tau/\nu$ obtained independently

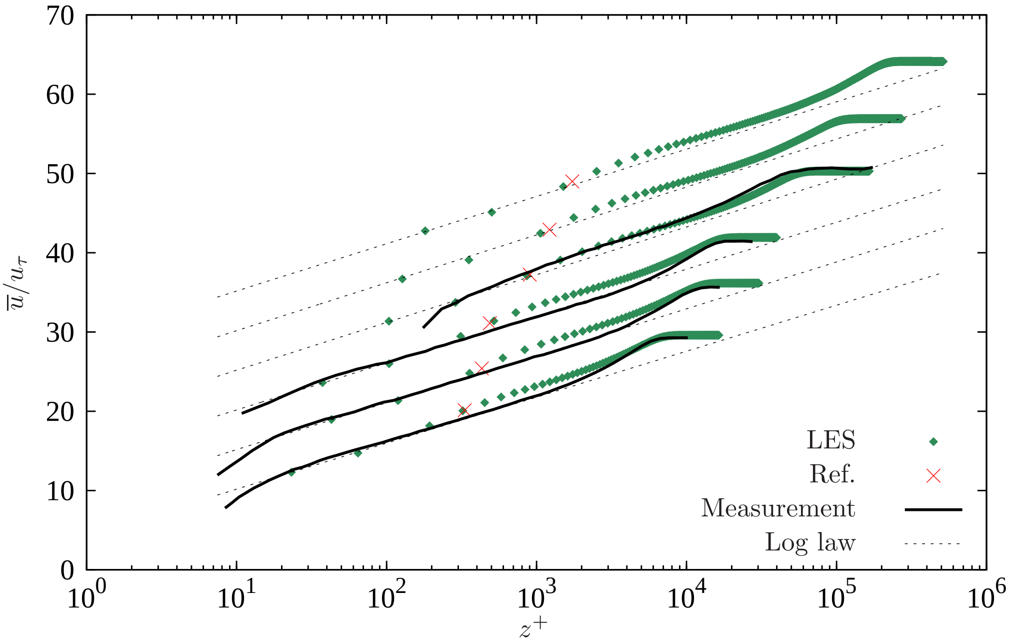

Figure 4.3. Mean velocity profile for cases 7.3k-θ, 13.6k-θ, 19k-θH, 62k-τ, 100k-τ, and 200k-τ (from bottom to top). The experimental measurements at $Re_\tau = 7,300$, $13,600$, and $19,000$ are from Mathis et al. (2011), and those at $Re_\tau = 62,000$ are from Oweis et al. (2010). The symbol "$\times$" marks the location of where the large-scale component is measured. Profiles are displaced 5 units of $\overline{u}/u_\tau$ for clarity. Dashed-lines are log law using $\overline{\mathcal{K}_1}$ from (3.13) and an additive constant B from (3.15). Also see table 4.2.

from both LES and experiment are reasonably closely matched. See Table 4.2 for integral quantities of each simulation case and its corresponding experimental measurements.

Figure 4.3 shows LES mean velocity profiles in inner-scaling, $\overline{u^+} = \overline{u}/u_\tau$, for all Reynolds numbers compared with experimental measurements where available. LES captures the mean velocity profile reasonably accurately. We remark that the mismatch seen in the case 62k-τ is affected by the difference in Re_θ between the LES result (1.71×10^5) and corresponding measurements (1.56×10^5). The symbol "$\times$" indicates the wall-normal location ($z_O^+ \approx \sqrt{15\, Re_\tau}$) where the large-scale velocity signal, $u_{OL}^+(t)$, is measured in LES. Although small, there seems to be a drop off in $\overline{u^+}$ towards the virtual wall. We interpret this as the influence of a logarithmic-layer mismatch (Brasseur and Wei 2010).

4.4 Results at intermediate Reynolds numbers

The velocity signals recorded in LES are now filtered to extract the large scale fluctuating velocity $u_{OL}^+(t)$, an input to the predictive inner–outer model. In the following sections, we discuss our observations of the predicted statistics, including spectra and some higher-order moments within the inner region. The effects of resolution and the length of velocity time series are also discussed. We will refer to three distinct type of results: direct experimental measurements (Exp), inner-layer predictions obtained using the PIO model with $u_{OL}^+(t)$ provided by experiment (Exp-PIO) and inner-layer predictions obtained using the PIO model with $u_{OL}^+(t)$ provided by LES (LES-PIO).

4.4.1 Streamwise turbulent intensity

Figure 4.4 shows a comparison of the predicted streamwise turbulent intensity profile, LES-PIO, against experimental measurement (Exp) and prediction (Exp-PIO). Also included in Figure 4.4 is the turbulent intensity profile from LES over $z^+ > h_0^+$ containing SGS corrections to the resolved-flow calculated as $\overline{u'^2} = \overline{\widetilde{u}'\widetilde{u}'} + \overline{T_{xx}}$. The predicted LES-PIO $u'_{\mathrm{rms}}/u_\tau = \sqrt{\overline{u'^2}/u_\tau^2}$ profiles capture the essential features of the energy, including the slight increase of the near-wall peak with increasing Re_τ. The LES is seen to underestimate the intensity in the outer-region. This comes from the fact that not all scales are resolved with LES, which led to a slight underestimation of the turbulent intensity due to the missing small-scale energy content by the SGS model in the outer-region (which has a small, but noticeable, contribution). However, since only the large-scale component is needed for the PIO model, this does not affect the prediction. Furthermore, the good agreement between LES-PIO and Exp-PIO results demonstrates the capabilities of LES to capture accurately the large-scales required as input to the PIO model.

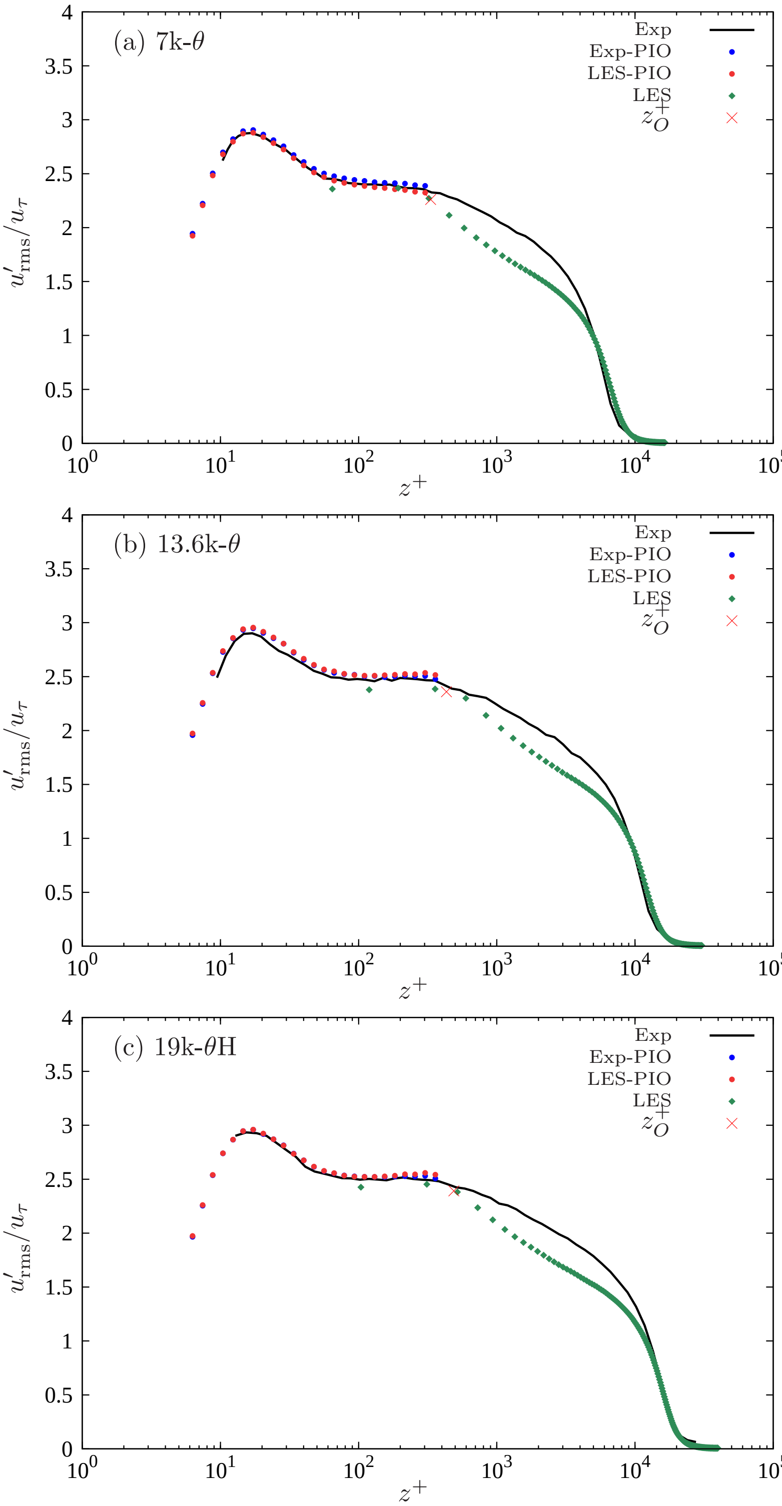

Figure 4.4. Prediction of streamwise turbulence intensity u'_{rms}/u_τ as compared to measurements. Shown are direct experiment, direct LES and predictions of inner-layer intensities obtained using velocity signals from both experiment (Exp-PIO) and LES (LES-PIO). The symbol "$\times$" marks the location where the time series $u^+_{OL}(t)$ is measured. (a) Case 7k-θ; (b) Case 13.6k-θ; (c) Case 19k-θH

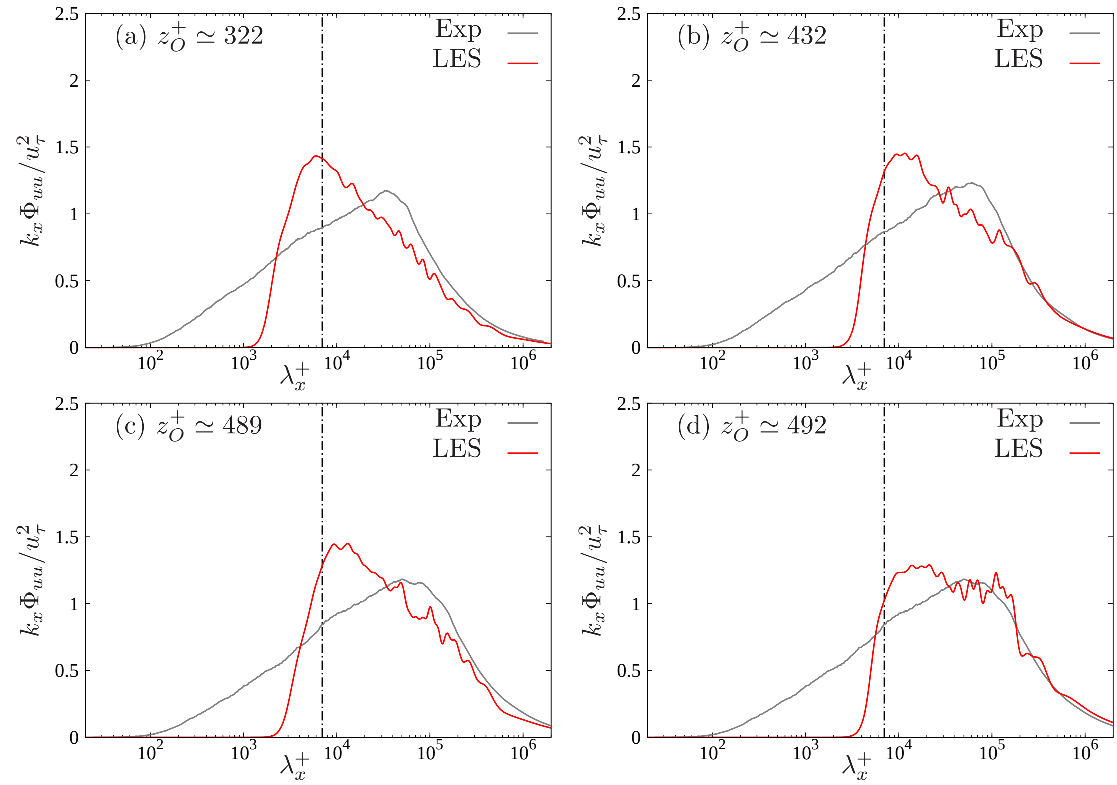

Figure 4.5. Premultiplied energy spectra of the streamwise velocity fluctuations $k_x \Phi_{uu}/u_\tau^2$ at $z_O^+ \simeq \sqrt{15 Re_\tau}$ as compared to measurements; thick (red) lines: LES; thin (grey) solid lines: measurements (Mathis et al. 2011). (a) Case 7k-θ; (b) Case 13.6k-θ; (c) Case 19k-θH; (d) Case 19k-θL. The vertical dot-dashed line shows the location of the cutoff wavelength, $\lambda_x^+ = 7000$.

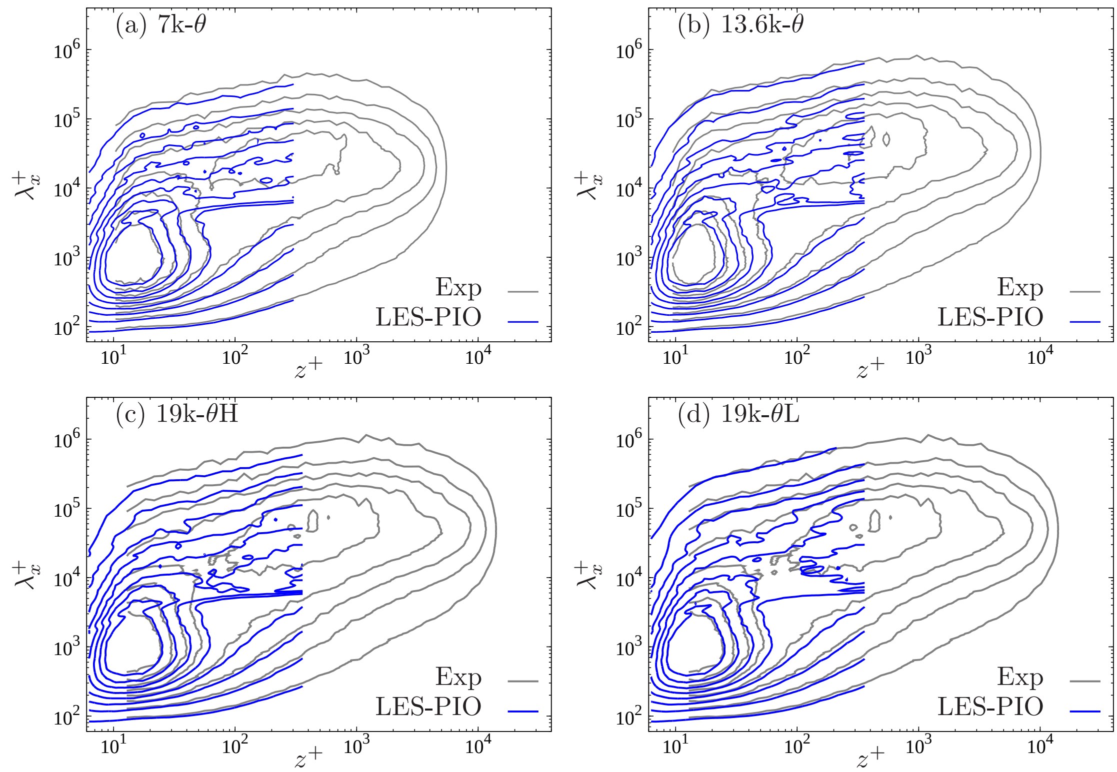

Figure 4.6. Predicted pre-multiplied energy spectra map of the streamwise velocity fluctuations $k_x\Phi_{uu}/U_\tau^2$; thick (blue) lines: prediction from LES-resolved velocity signal; thin (grey) solid lines: measurements (Mathis et al. 2011). (a) Case 7k-θ; (b) Case 13.6k-θ; (c) Case 19k-θH; (d) Case 19k-θL. Contours levels show $k_x\Phi_{uu}/U_\tau^2$ from 0.2 to 1.6 in steps of 0.2.

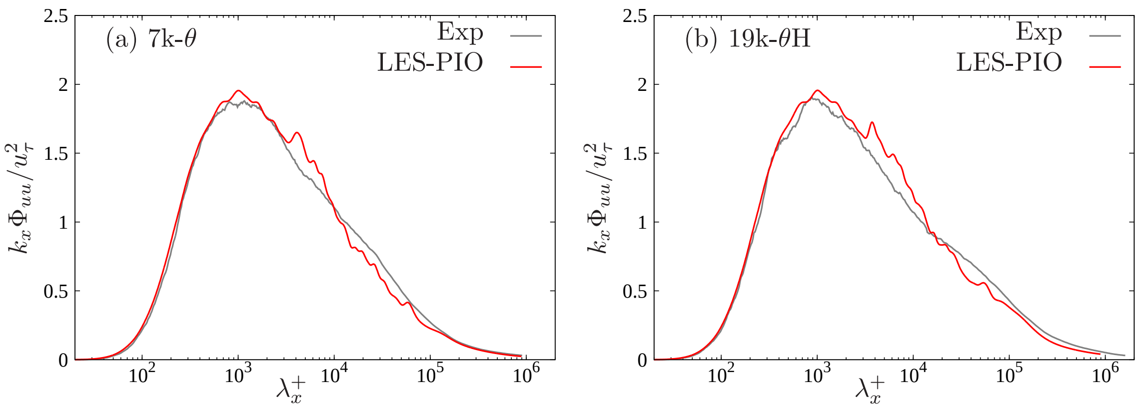

Figure 4.7. Example of predicted premultiplied energy spectra $k_x\Phi_{uu}/u_\tau^2$ at the inner-peak location ($z^+ \simeq 15$) as compared to measurements; thick (red) lines: prediction from LES-resolved velocity signal; thin (grey) solid lines: measurements (Mathis et al. 2011). (a) Case 7k-θ; (b) Case 19k-θH

4.4.2 Longitudinal spectra of streamwise velocity

Figure 4.5 shows the premultiplied energy spectra of the streamwise velocity fluctuations, $k_x\Phi_{uu}/u_\tau^2$, for the resolved velocity signal (u_O^+, i.e., not filtered) from LES and experiment at $Re_\tau \approx 7,300, 13,600$ and $19,000$, all at $z^+ \approx z_O^+$. It is clear that the experimental time series covers a substantially wider domain at the small scales than the LES. This is the effect of the LES cutoff at the local grid scale. Case 19k-θH covers a wider range of scales than case 19k-θL (see Figure 4.5(c–d)) because of the smaller time step size dt. Although the position of the spectra maximum tends to be shifted toward smaller scales for the LES, the peak magnitude of LES and experiment are comparable. Importantly, the turbulent energy of the large-scale signal u_{OL}^+ — the areas under the curve on the right-hand side of the cutoff wavelength $\lambda_x^+ \geq 7,000$ — remains close, only differing by a slight energy re-distribution. We recall that to extract u_{OL}^+ from the velocity signal taken from LES, the velocity signal u_O^+ is filtered to retain only large scales above streamwise wavelengths of $\lambda_x^+ = 7,000$. This constitutes another limiting factor for higher Reynolds number application of the current LES as it is necessary to take smaller dt as Reynolds number increases to fulfil this requirement.

The contour maps of predicted premultiplied energy spectra, $k_x\Phi_{uu}/u_\tau^2$, shown in Figure 4.6, indicate that the Reynolds number effects are well captured by the LES-PIO model. Particularly, the increasing large-scale energy content with increasing Re_τ. A closer view of the premultiplied energy spectra is given in Figure 4.7, at the inner-peak location $z^+ \simeq 15$ and for two Reynolds numbers, $Re_\tau = 7,300$ and $19,000$. Again, excellent agreement is observed. However, in Figures 4.6 and 4.7 a distinct discontinuity or a hump is observed around $\lambda_x^+ \simeq 4,000$–$7,000$. This discontinuity is attributed to the fact that the model in equation (4.1) combines signals from two different data sources, LES and experiments, which are not synchronized together (even if the purpose of Fourier phase shift is to attempt to resolve this issue). Therefore, there is an overlap in the spectral domain between the universal signal u^* and the large-scale input component u_{OL}^+, which induces this discontinuity. There are also nonlinear effects in equation (4.1) arising from multiplying two time series with different spectral support. Nevertheless, this does not propagate nor does it contaminate other statistics due to the fact the discontinuity has a very low energy.

4.4.3 Signal length and resolution effects

To ensure that results are not sensitive to the signal length provided by LES, sensitivity tests were performed for all the cases using elongated velocity signals constructed from concatenation of signals from different spanwise locations. Spanwise locations were at least $2\delta_0$ apart to obtain uncorrelated signals. The results (not shown) do not make noticeable changes to the predictions. This is because the largest scales are already captured and converged in the time series obtained at a single location, allowed by the large computational domain used by the LES, $(L_x, L_y, L_z) = (72\delta_0, 6\delta_0, 4\delta_0)$.

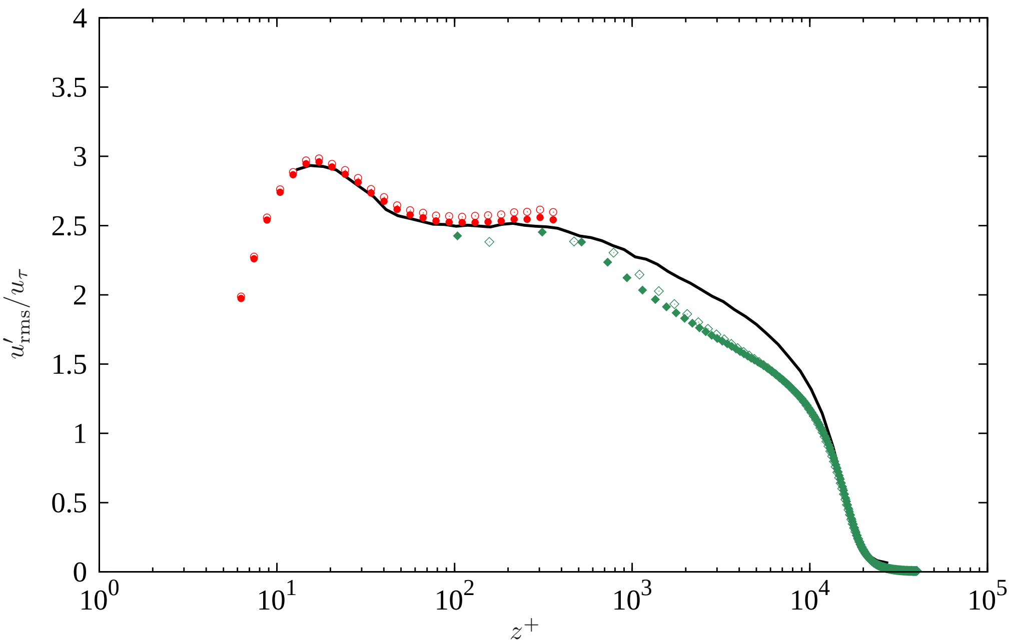

Figure 4.8. The effect of resolution in LES-PIO predictions of streamwise turbulence intensity u'_{rms}/u_τ as compared to measurements. Also shown are intensities obtained directly from the LES. Solid: case 19k-θH; open: case 19k-θL

Figure 4.8 shows the effect of the LES grid's resolution on the predicted turbulent intensity profile at $Re_\tau = 19\,000$, for the low resolution case (19k-θL) and the high resolution case (19k-θH). The slightly larger prediction observed on the low resolution case is probably attributed to the LES containing more energy in the very long scales, compared to case 19k-θH as seen in Figure 4.5(c–d). Overall, the prediction from the higher resolution case 19k-θH agrees better with the experimental data. Recall that the grid position of z_O^+ is chosen to avoid the underresolved region close to the virtual wall. The argument that numerical and modeling errors are unavoidable in the first few grid points was discussed in Cabot and Moin (2000).

4.5 Results at larger Reynolds number

4.5.1 Turbulence intensity and spectra

The combined LES-PIO model has been shown to fairly accurately reconstruct the near-wall field at intermediate Reynolds numbers. Particularly, a good agreement has been found with experiments and Exp-PIO predictions. Now we test the model at higher Reynolds numbers, $Re_\tau = 62,000$, $100,000$ and $200,000$, filling the gap between laboratory and atmospheric surface layer data. It should be noted that at such high-Re_τ there is no experimental data available in the near-wall region for comparison, and outer-region data are only available for $Re_\tau = 62,000$. Figure 4.9 de-

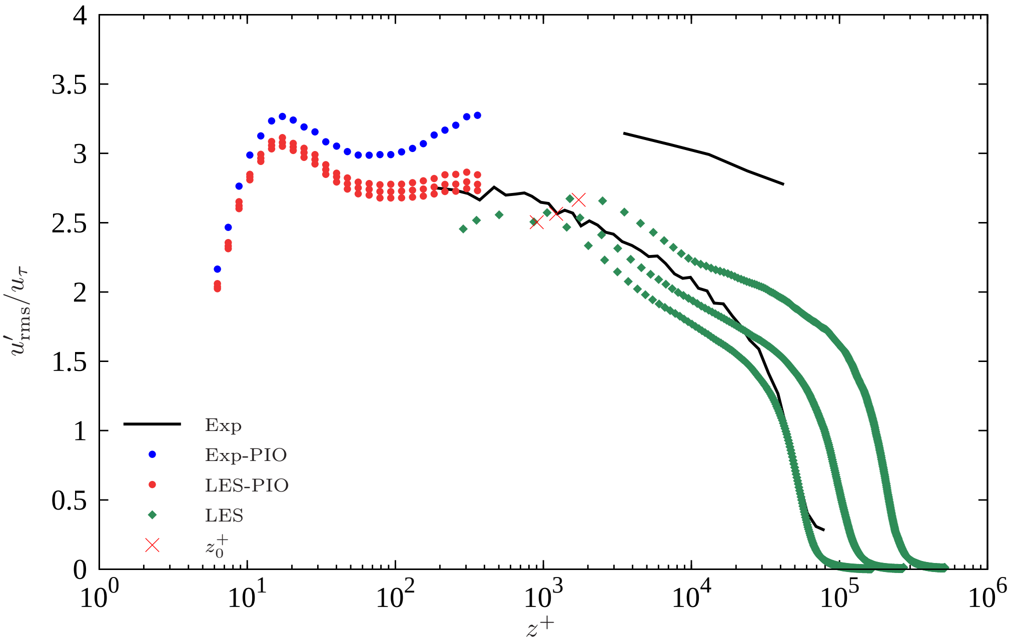

Figure 4.9. Prediction of streamwise turbulence intensity u'_{rms}/u_τ for cases 62k-τ, 100k-τ, and 200k-τ. Also shown are measurements at $Re_\tau = 62,000$ (courtesy of D. Dowling) and at $Re_\tau = 1.4 \times 10^6$ from SLTEST. The symbol "$\times$" marks the location where the large-scale component is measured.

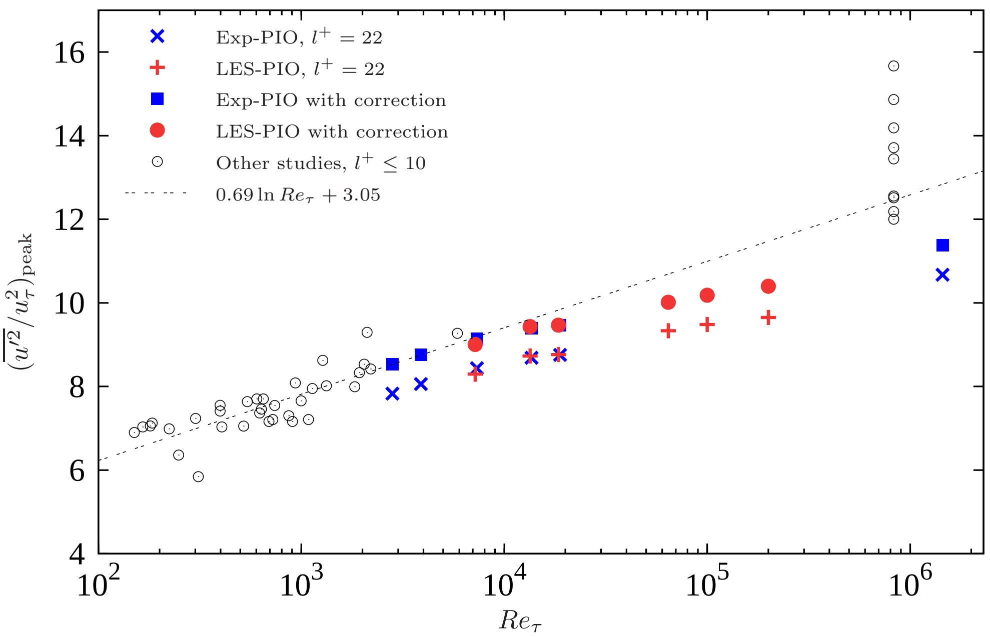

Figure 4.10. Reynolds number dependency of the inner-peak intensity $\overline{u'^2}/u_\tau^2$ (around $z^+ = 15$) for Exp-PIO, LES-PIO and those with correction taking into account the hot-wire spatial resolution effect (Chin et al. 2009) to an assumed wire length of $l^+ = 3.8$; The open-circle symbols ($\bigcirc$) are a compilation of results from where $l^+ \leq 10$, including DNS and experimental measurements from channel flow, boundary layer and atmospheric surface layer (see Hutchins and Marusic (2007a) for details).

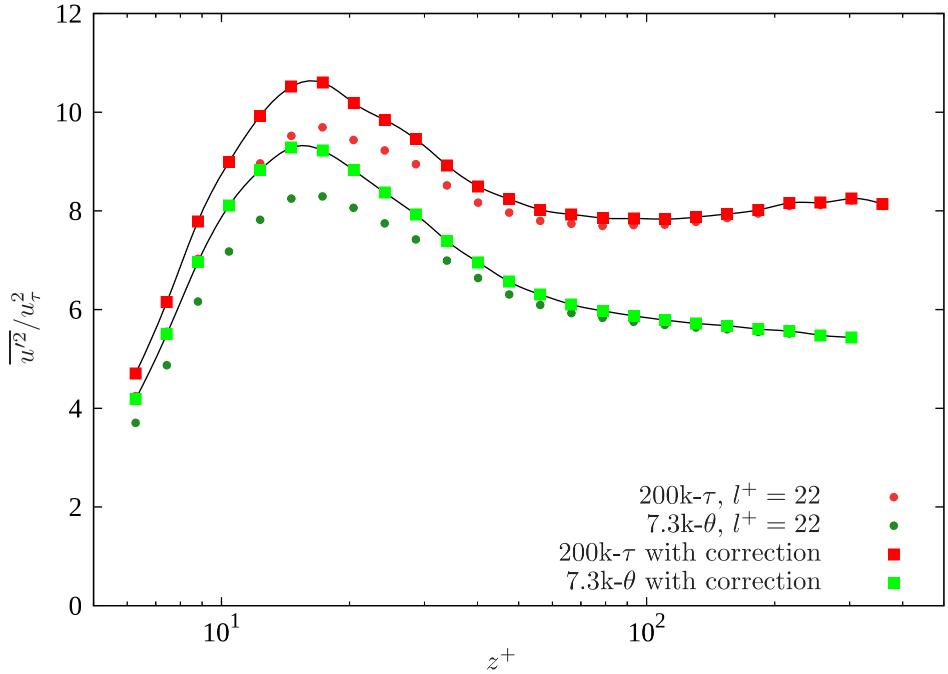

Figure 4.11. Prediction of streamwise turbulence intensity $\overline{u'^2}/u_\tau^2$ corrected using method of Smits et al. (2011) to a hypothetical infinitesimally small sensor ($l^+ = 0$) for cases 7.3k-θ, 200k-τ

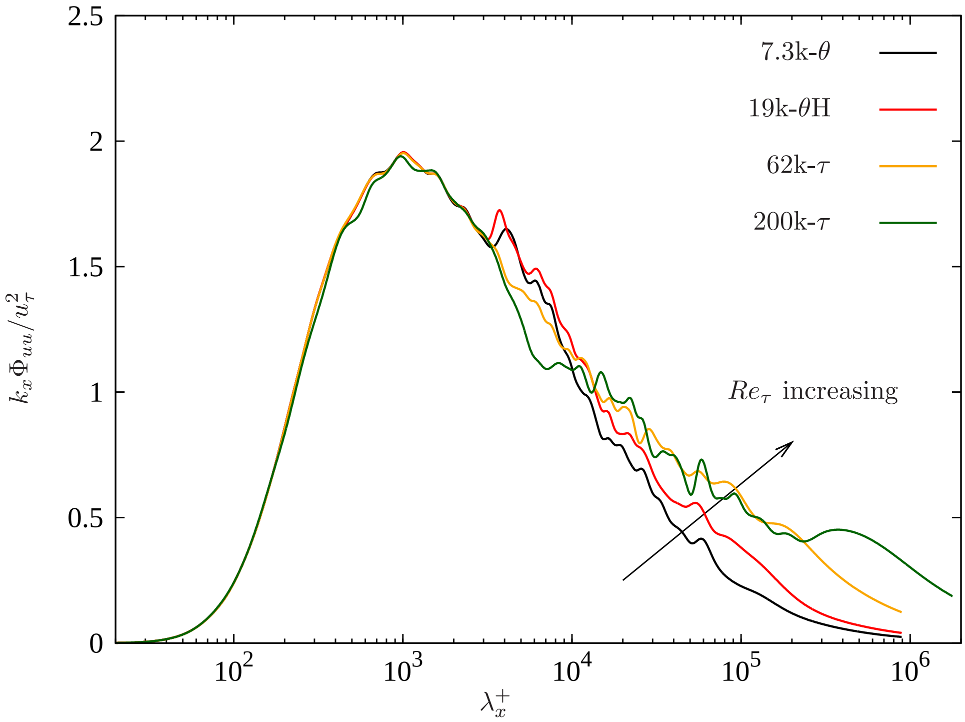

Figure 4.12. Reynolds number evolution of the predicted premultiplied energy spectra $k_x\Phi_{uu}/u_\tau^2$ at the inner-peak location ($z^+ \simeq 15$) for cases 7.3k-θ, 19k-θH, 62k-τ, and 200k-τ

picts the predicted streamwise turbulent intensity profiles along with LES and experimental results. SLTEST data and corresponding Exp-PIO results have been included as an indicator of the predicted trends of turbulence intensity obtained from experiment. As discussed previously, the LES tends to underestimate the intensities in the outer part of the boundary layer, due to the missing small-scale energy content, but the essential Re_τ dependency feature is well captured. The magnitude of the LES-PIO intensity results at $Re_\tau = 62,000$ are in good agreement with experiment, at least where the measurements and the prediction intersects. The SLTEST prediction, at $Re_\tau = 1.4 \times 10^6$ suggests that at high-Re_τ a second peak in the streamwise turbulent intensity profile emerges, and the LES-PIO results appear to support this. However, it should be recalled that the PIO model has been built using hot-wire measurements where a normalized sensor length, $l^+ = lu_\tau/\nu = 22$, was used. Therefore, u^* and u_p^+ in equation (4.1) have the same spatial resolution characteristic, and the emergence of the second peak might be a result of spatial resolution issues (Hutchins et al. 2009, Marusic et al. 2010b). Figure 4.11 shows prediction of the streamwise turbulence intensity $\overline{u'^2}/u_\tau^2$ corrected using the method of Smits et al. (2011) to a hypothetical infinitesimally small sensor ($l^+ = 0$). The method, based on eddy scaling, takes into account the attenuation of small scale contributions due to the relatively large sensor length. Hypothetically, the corrected prediction represents the "true" profiles which can be seen to show some indication of a second peak at high-Re_τ.

Nevertheless, the existence of an outer peak remains an open question. Based on the diagnostic plot (Alfredsson and Örlü 2010), Alfredsson et al. (2011) suggested that an outer peak does exist at $z^+ = 0.81Re_\tau^{0.56}$ if the Reynolds number is sufficiently large. For pipe flow, McKeon and Sharma (2010) use a linear model to identify a dominant VLSM-like mode whose propagation velocity matches the local mean velocity at $z^+ \sim Re_\tau^{2/3}$. They argue that at this "critical layer", the exchange of energy between the mean flow and the forced mode is enhanced resulting in a peak in turbulence intensity. It should be noted that LES-PIO results shown in the present paper are up to $z^+ \approx 360$, and do not reach the proposed outer-peak location for cases 62k-τ to 200k-τ (respectively, $z^+ = 970$ and $z^+ = 1230$).

Figure 4.10 shows the Reynolds number dependency of the near-wall peak in $\overline{u'^2}/u_\tau^2$, for Exp-PIO and all LES-PIO results, along with available data from the literature. Also included are the spatially corrected Exp-PIO and LES-PIO results using the correction scheme proposed by Chin et al. (2009) to take into account the spatial resolution effects of the PIO model ($l^+ = 22$), where the missing energy is modeled using two-dimensional spectra from DNS of turbulent channel flow. Overall, the LES-PIO follows the general trends of both direct measurement and Exp-PIO and support log-like increase in $\overline{u'^2}/u_\tau^2$ with increasing Re_τ. In particular the three high-Reynolds-number LES-PIO results are seen to fall within a large gap between laboratory and SLTEST estimates.

The energy content of all LES-PIO prediction, for cases 7.3k-θ, 19k-θH, 62k-τ and 200k-τ, are given in Figure 4.12 for the inner-peak location, $z^+ \simeq 15$. Again, it can be observed that the

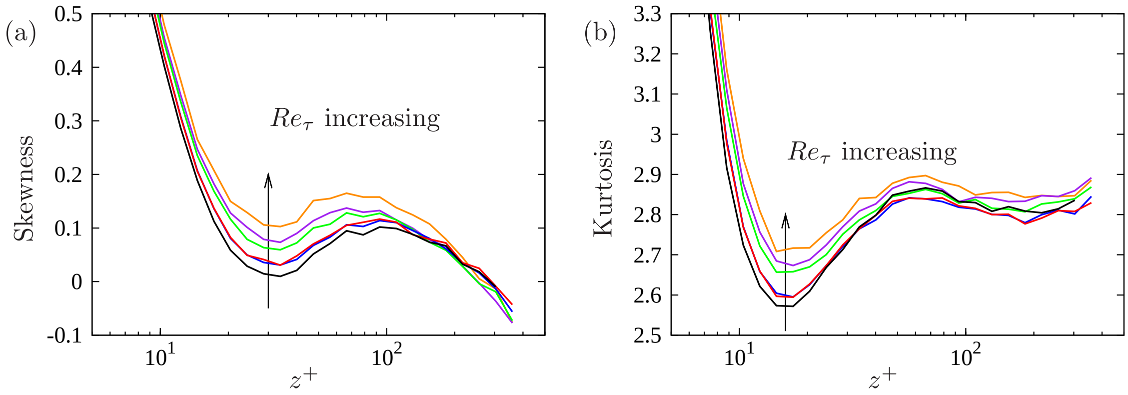

Figure 4.13. Reynolds number dependency of predicted (a) skewness and (b) kurtosis using the LES-PIO model, for cases 7.3k-θ, 13.6k-θ, 19k-θH, 62k-τ, 100k-τ, and 200k-τ.

increasing large-scale energy with increasing Re_τ is well captured by the LES-PIO, identically to the Exp-PIO model shown in Mathis et al. (2011).

4.5.2 Higher-order statistics

Figure 4.13 shows the predicted LES-PIO skewness and kurtosis for all present Reynolds numbers. The small but definite Reynolds number dependency is clear.

Direct LES and LES-PIO results for skewness and kurtosis are shown compared with direct experimental measurement and also Exp-PIO results in Figure 4.14. The LES-PIO results show excellent agreement with experiment in the inner layer while Exp-PIO and the LES-PIO results are indistinguishable. The results of direct LES in the outer layer are overall good up to the edge of boundary layer, except for a few grid points near the virtual wall. As in turbulent intensity prediction, a discontinuity can be seen between the inner-layer LES-PIO results and the direct outer-layer LES results (see Figures 4.4 and 4.9.) It should be noted that the PIO model does not guarantee that the predicted value should exactly match the actual value that the velocity signal itself has at $z^+ = z_O^+$. The velocity signal used as an input only contains the fluctuations of the larger scale components. In an LES context, the input signal is a resolved scale signal without a subgrid contribution, while the numerical values shown as outer-layer LES calculation in each figure contain a sum of resolved and estimated subgrid contributions ($\overline{u'^2} = \overline{\widetilde{u}'\widetilde{u}'} + \overline{T_{xx}}$, for example).

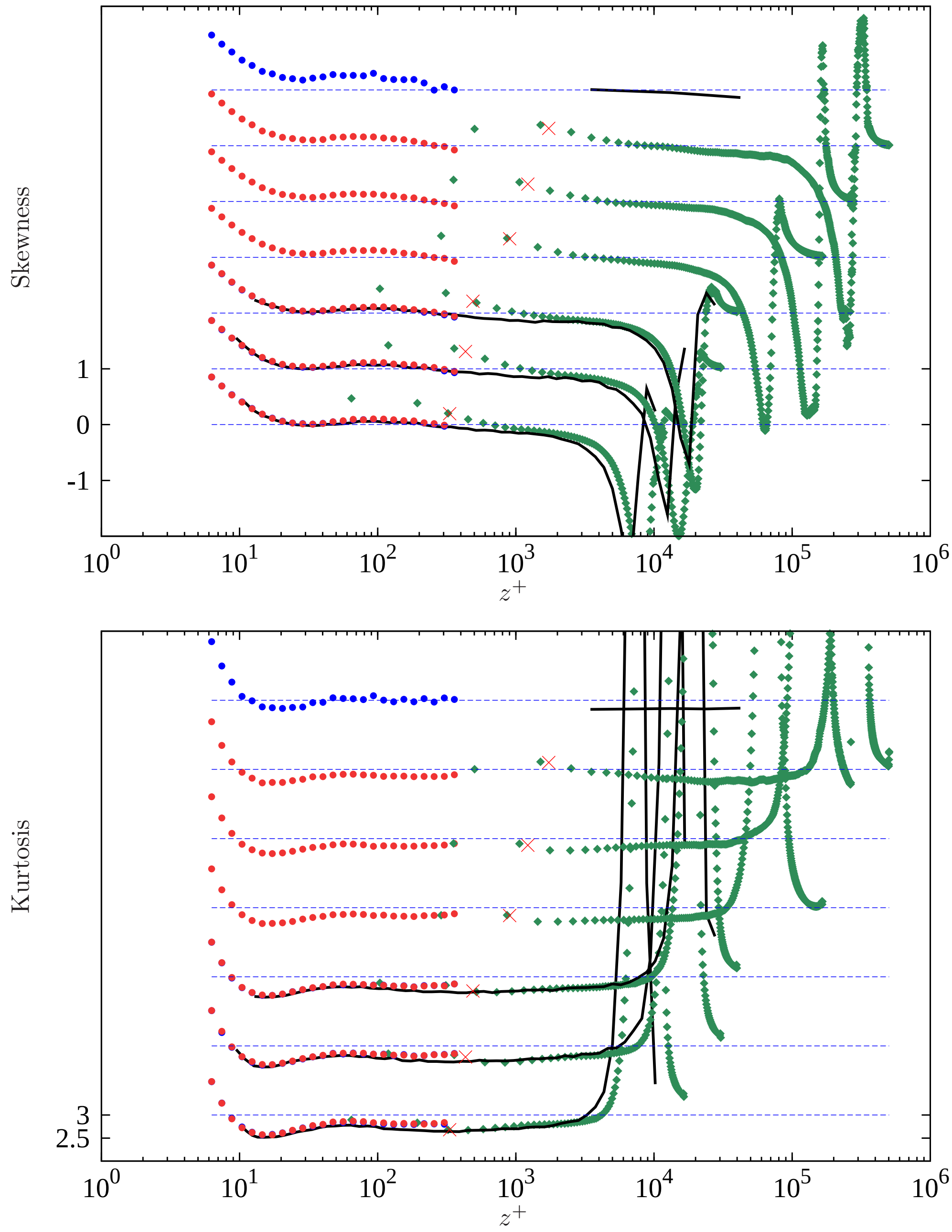

Figure 4.14. Skewness $\overline{u'^3}/(\overline{u'^2})^{3/2}$ and kurtosis $\overline{u'^4}/(\overline{u'^2})^2$ profile for cases 7.3k-θ, 13.6k-θ, 19k-θH, 62k-τ, 100k-τ, and 200k-τ (from bottom to top). The experimental measurements at $Re_\tau = 7,300$, $13,600$ and $19,000$ are from Mathis et al. (2011). The highest Reynolds number case corresponds to SLTEST data. The symbol "$\times$" marks the location of where the large-scale component is measured. For key, see Figure 4.9.

Chapter 5

LES of the adverse-pressure gradient turbulent boundary layer

5.1 Background

There is a growing need for reliable, accurate LES models suitable for real-world flows. The behavior of the boundary layer over aerospace vehicles, for both the inner flow or outer flow, usually exhibits complex behavior of high Reynolds number. In spite of recent advances in computational capabilities, highly accurate simulations, for example, of separated flow on the wings of airplanes or for flow through turbine blades in jet engines has not been achieved. When such simulations become possible at reasonable computational cost, engineers in industry will be able to investigate other critical problems that are at the moment accessible only by costly physical experiments. As a step toward this, we presently consider the LES of the adverse-pressure gradient flat-plate turbulent boundary layer. The implementation of our wall model and the interior SGS model, which is entirely local in character including its incorporation of local pressure gradients, should be applicable to adverse-pressure-gradient turbulent boundary layers (APGTBL).

Although there are some established features in APGTBL such as the amplified wake of the mean velocity profile and the increasing turbulence intensity in the outer region, the difficulty in APGTBL research is the wide range of parameters that have to be considered such as the upstream history, the local pressure gradient, and if the flow should be in some defined form of equilibrium. Commonly, a constant nondimensional pressure gradient parameter (Clauser 1956),

$$\beta = \frac{\delta^*}{\tau_w}\frac{dP}{dx}, \tag{5.1}$$

where δ^* is the displacement thickness, τ_w is the wall shear stress and dP/dx is the pressure gradient, has been taken as a condition for “equilibrium” layers whose velocity profiles, Clauser (1956) proposed, are identical when plotted in a velocity defect form at each cross section. Mellor and Gibson

(1966) and Bradshaw (1967) have suggested that an approximate equilibrium flow is obtained when the variation of free-stream velocity has the form of a power-law relation in the streamwise direction. That is to say, a practically constant β results if the outer-edge velocity is chosen as $U_\infty \sim (x - x_0)^m$ (where x_0 is a virtual origin, and m is a constant power).

Skote et al. (1998) summarized previous theoretical and experimental work on selfsimilar turbulent boundary layer flows under adverse-pressure gradients. Those works seem to reach a consensus that separation occurs for $-0.25 < m < -0.20$ with a shape factor of about 2. Also Schofield (1981) concluded that no selfsimilar solution can be achieved for $m < -0.3$ and only one selfsimilar solution exists for $m > -0.23$. Skote et al. (1998) reviewed relations between m and β using the assumption of infinite Reynolds number and the use of specific velocity and length scales. Including the works mentioned above, this class of equilibrium APGTBL have been studied by both numerical simulations (e.g., Henkes et al. 1997, Skote et al. 1998, Lee and Sung 2008, Lee et al. 2010) and experiments (e.g., Skåre and Krogstad 1994, Nagano et al. 1998).

There are several other parameters that characterize APGTBL as discussed by Perry and Marusic (1995), Marusic and Perry (1995), Perry et al. (2002), such as a skin friction parameter (or S-factor), the Coles' wake factor Π and a nonequilibrium parameter ξ, which is a function of a streamwise derivative of Π, the S-factor and the boundary layer thickness. Yet another class of "quasi-equilibrium" layers were postulated by Perry et al. (1994), which has selfsimilarity in both velocity and shear stress profiles, with Π being constant or allowed to vary in the streamwise direction but this variation is sufficiently slow. Under this condition, we have a selfsimilar velocity defect distribution implying a selfsimilar shear stress distribution. It should be noted that the above discussion, however, is based on the assumption that a universal logarithmic law exists. Monty et al. (2011) argued that this may not be suitable for the APGTBL since it has been observed by several researchers that the value of Kármán constant κ shows some sensitivity to the pressure gradient and that there seems to be a shift of the mean velocity profile from the log-law (e.g., Nagano et al. 1998, Nickels 2004, Lee and Sung 2008). As a result, depending on the log-law chosen, the wake factor Π can vary.

Monty et al. (2011) performed a parametric study of the behavior of the APGTBL and suggested that β is useful for characterizing the flow observing the good collapse in flow statistics with constant β. The effect of three parameters were investigated: a friction Reynolds number Re_τ, pressure gradient parameter β and an acceleration parameter

$$K = \frac{\nu}{U_\infty^2} \frac{dU_\infty}{dx}, \tag{5.2}$$

where U_∞ is the local free-stream velocity and ν is the kinematic viscosity.

Many important features of the APGTBL are well understood through extensive studies on

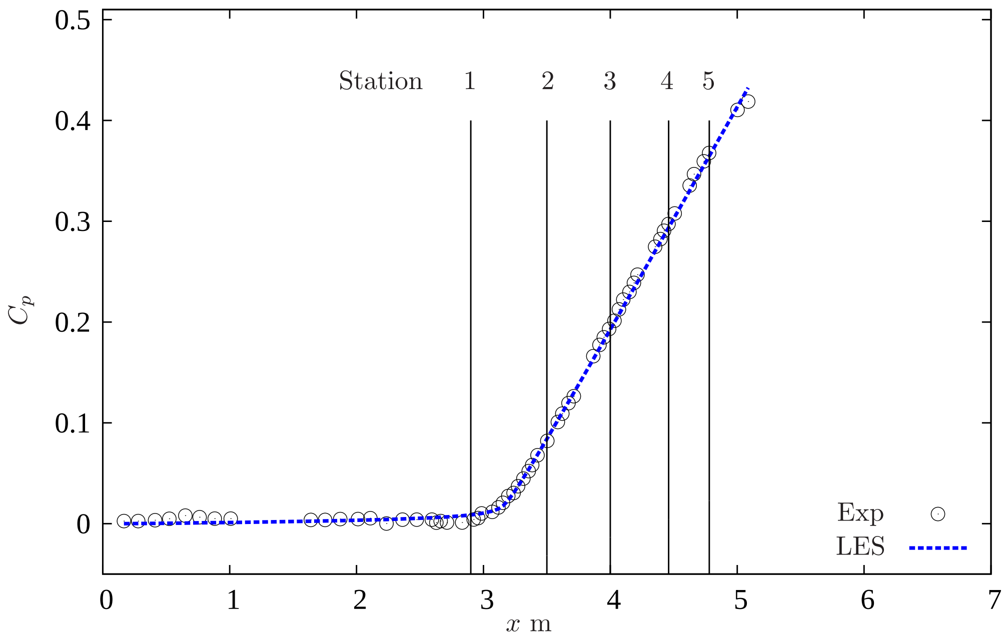

Figure 5.1. Profile of coefficient of pressure C_p: a smoothed profile used in LES and experimental measurements: Z. Harun & I. Marusic (Private Communication)

"equilibrium" flows over the past decades. Compared with other canonical turbulence flows; pipe, channel and ZPGTBL, however, the present state knowledge of the APGTBL is very sparse (Marusic and Perry 1995) and perhaps insufficient to draw conclusions on their general behaviors including the probably broad class of nonequilibrium APGTBLs. The latter remain to be investigated. Here we aim to reproduce an experimental setting with a constant pressure gradient, the simplest class of pressure distributions also seen in other canonical flows. We intend to extend the discussion towards higher Reynolds numbers. In §5.2, an account is given of the problem setting including matching a pressure distribution in an experiment. The numerical implementation of the experimental setting and the present LES on the APGTBL over a range of Reynolds numbers are presented in §5.3, followed by results and discussion in §5.4.

5.2 Problem setting

We attempt to reproduce the experimental setup of an open-return blower wind tunnel, whose details can be found in Marusic and Perry (1995), Harun et al. (2010), Monty et al. (2011). All of the experimental data used and cited presently were kindly supplied by Z. Harun and I. Marusic (private communication). The pressure gradient was adjusted by the height of the flexible test section ceiling. The area of the tunnel cross-section increases nominally exponentially to maintain a constant pressure gradient. The flexible ceiling was configured so that a zero-pressure gradient is

Station	x [m]	U_∞ [m/s]	Re_τ	Re_θ	δ [m]	θ [m]
1	2.90	15.68	2330	6560	0.061	0.0064
2	3.50	15.12	2670	8120	0.076	0.0085
3	4.00	14.43	2380	8590	0.076	0.0095
4	4.46	13.43	2500	10500	0.090	0.0122
5	4.78	12.89	2500	11630	0.102	0.0143

Table 5.1. Experimental parameters for hot-wire anemometry at five measurement locations. The free-stream velocity at the inlet ($x = 0$ m) is $U_{\text{inlet}} = 15.9$ m/s. All data from private communication with Z. Harun and I. Marusic.

maintained until $x = 3$ m followed by an constant adverse-pressure gradient section thereafter until $x = 6.7$ m. Figure 5.1 shows the coefficient of pressure C_p,

$$C_p = \frac{p - p_{\text{inlet}}}{\frac{1}{2}\rho U_\infty^2} = 1 - \left(\frac{U_\infty}{U_{\text{inlet}}}\right)^2, \tag{5.3}$$

along the streamwise direction in the tunnel and indicates five locations where streamwise velocities were measured by hot-wire anemometry, $x_1 = 2.90$ m, $x_2 = 3.50$ m, $x_3 = 4.00$ m, $x_4 = 4.46$ m and $x_5 = 4.78$ m. When applying the pressure boundary condition at the top in LES, a smooth function representation of C_p is used to avoid discontinuities. Table 5.1 shows experimental results at each location.

5.3 LES performed

In total the results of five different LES are reported in detail presently. The wall-model LES are summarized in Table 5.2. Case D1 was designed to match experimental conditions reported in §5.2 based on $Re_\theta = \theta U_\infty/\nu = 6560$ at $x_{1,\text{exp}} = 2.90$ m in the experimental setting, where θ is the momentum thickness and U_∞ is the free-stream velocity. Then the same pressure distribution is used for the other cases. The LES equations are normalized by using the free-stream velocity and the boundary layer thickness at the inflow plane, U_0 and δ_0, respectively. Typically an individual LES is done by fixing a nominal Reynolds number $Re_0 = U_0\delta_0/\nu$, so that the resulting Re_θ at $x_{1,\text{LES}}$ is close to the expected value. LES have been performed at resolutions $(N_x, N_y, N_z) = (768, 64, 128)$, the grid is uniform and $\Delta_x = \Delta_y = 3\Delta_z$ throughout the simulation domain without stretching in the wall-normal direction. The raised wall is at $h_0 = 0.18\,\Delta_z$ for all LES.

LES were performed in a domain $(L_x/\delta_0, L_y/\delta_0, L_z/\delta_0) = (72, 6, 4)$, where δ_0 is the inlet boundary-layer thickness. The domain size in the streamwise direction is designed to be sufficiently long to cover the range between x_1 and x_5. Also the adverse-pressure gradient starts at $x_{1,\text{LES}} = 0.35\,L_x$ in the computational domain in order to allow a sufficiently long streamwise length from the inlet to obtain an equilibrium ZPGTBL on which the inflow generation scheme of Lund et al. (1998) is based.

Case	Re_0	L_x/δ_0	L_y/δ_0	L_z/δ_0	N_x	N_y	N_z	h_0/δ_0	x_{ref}/L_x
D1	4.58×10^4	72	6	4	768	64	128	5.6e-3	20%
D2	1.54×10^5	72	6	4	768	64	128	5.6e-3	20%
D3	5.61×10^5	72	6	4	768	64	128	5.6e-3	20%
D4	1.86×10^6	72	6	4	768	64	128	5.6e-3	20%
D5	6.51×10^6	72	6	4	768	64	128	5.6e-3	20%

Table 5.2. Simulation parameters: $Re_0 = U_0\delta_0/\nu$; U_0 and δ_0 is the free-stream velocity and the 99% boundary layer thickness at the inlet of the domain, respectively. $\Delta_x = \Delta_y = 3\Delta_z$. $h_0 = 0.18\Delta_z$. x_{ref}/L_x is the location where a velocity data is taken and rescaled for inflow velocities. The mirroring method (Jewkes et al. 2011) is employed in addition to the inflow generation scheme of Lund et al. (1998).

The location of the recycling plane is set at $x_{\text{ref,LES}} = 0.2\,L_x$ to avoid the effect of adverse-pressure gradient. The mirroring method proposed by Jewkes et al. (2011) was used for all the cases. At the top of the domain, the pressure boundary condition is employed (see §2.4) to reproduce the experimental pressure distribution $f(x)$,

$$P_\infty(x) = f(x) \text{ and } \frac{\partial u}{\partial z} = \frac{\partial v}{\partial z} = 0. \tag{5.4}$$

In case D1, our lowest Reynolds number case, the height of the raised "virtual" wall, where the wall-model provides the slip streamwise velocity, resides below the log-region, typically $h_0^+ < 10$. Therefore the the log-like relationship (see equation 3.13) is replaced with a linear profile

$$\widetilde{u^+}|_{h_0} = u_\tau h_0^+, \tag{5.5}$$

assuming the instantaneous streamwise velocity follows the linear relationship with inner-scaling within the viscous sublayer. This does not effect the ODE for wall-shear stress and the other boundary conditions follow §3.3.

5.4 Results and discussion

All results shown presently are obtained as spanwise/time averages. Figure 5.2 shows profiles of the pressure coefficient C_p and the pressure gradient dp/dx in case D1. It is observed that the LES reproduces the C_p profile from the measurement at corresponding streamwise locations. The length scale is matched using the momentum thickness θ at station 1. Two pressure-gradient profiles are shown: one is the pressure gradient at the top of the domain ($z = L_z$) and the other is at the first grid point from the virtual wall ($z = h_0 + \Delta_z/2$). The pressure gradient at the top is essentially prescribed by the pressure boundary condition. The profile at $z = h_0 + \Delta_z/2$, from a solution of

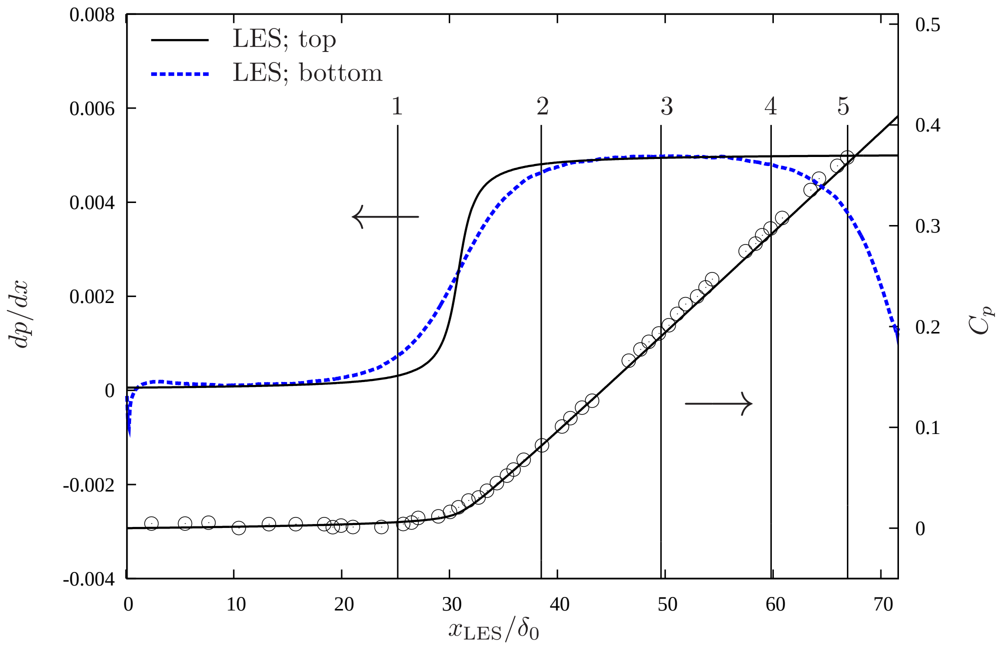

Figure 5.2. Profile of coefficient of pressure C_p and the pressure gradient distribution dp/dx. Solid linel; at top of the domain, dashed-line; at the first grid point from the virtual wall. ○: Experimental measurements of C_p at corresponding streamwise locations (Z. Harun & I. Marusic (private communication))

equation (2.13), indicates the pressure gradient decreases at the end of the domain because of the implicitly imposed condition: $dp/dx = 0$ at the boundary where Dirichlet boundary conditions are used for the boundary-normal velocity, u in this case. The increase in the pressure gradient at $x_{\mathrm{LES}} \approx 30\delta_0$ is not as sharp as that at the top boundary. Similar profiles were observed for all the other LES cases (not shown). It is observed that the effect of non-zero-pressure gradient propagates upstream as far as 10 boundary layer thickness at the bottom of the domain. It should be noted that the recycling plane is located at $x_{\mathrm{ref,LES}} \approx 14.4\delta_0$ where the pressure gradient is sufficiently small.

5.4.1 APG parameters

Figures 5.3 show profiles of the pressure gradient constant β, the acceleration parameter K and the normalized pressure gradient $(dp/dx)^+ \equiv \nu(dp/dx)/(u_\tau^3)$ along the streamwise direction in cases D1, D3, and D5. Results of case D2 and D4 follow the trend shown here but are omitted for clarity. Values of β, K and S at five measurement locations are also presented by Table 5.3. Albeit a slight difference up to 10%, the nondimensional pressure gradient, indicated by β shows a reasonably good collapse between three LES cases. This indicates the ratio of the pressure gradient acts across effective face area of the layer δ^* to the wall shear stress τ_w was kept almost constant over the range

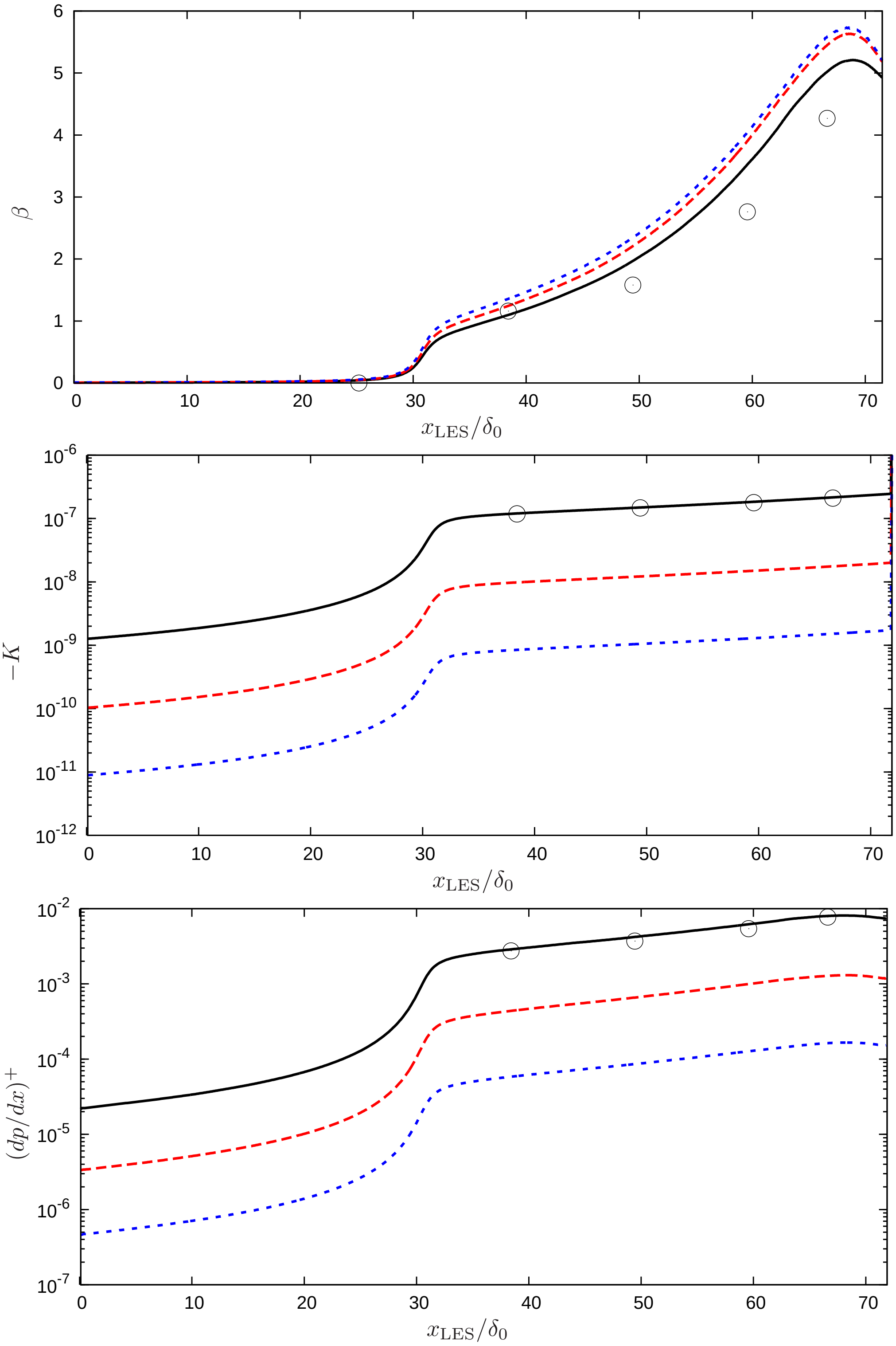

Figure 5.3. LES results; the pressure gradient parameter β, the acceleration parameter K, and the normalized pressure gradient $(dp/dx)^+ \equiv \nu(dp/dx)/(u_\tau^3)$. Solid; D1, dashed; D3, dotted; D5. $\circ$: Experimental measurements, see Table 5.4 for values.

Station	$x_{\rm LES}/\delta_0$	Re_θ	Re_τ	β	K	S
D1: 1	25.2	6.56×10^3	2.41×10^3	0.04	-0.07×10^{-7}	26.8
D1: 2	38.4	8.12×10^3	2.57×10^3	1.10	-0.20×10^{-7}	28.6
D1: 3	49.4	1.02×10^4	2.75×10^3	1.97	-1.49×10^{-7}	30.0
D1: 4	59.5	1.26×10^4	2.91×10^3	3.52	-1.83×10^{-7}	31.8
D1: 5	66.7	1.39×10^4	2.93×10^3	5.03	-2.16×10^{-7}	33.1
D3: 1	25.2	6.56×10^4	2.25×10^4	0.05	-0.06×10^{-8}	32.8
D3: 2	38.4	7.90×10^4	2.35×10^4	1.24	-0.98×10^{-8}	35.2
D3: 3	49.4	9.70×10^4	2.46×10^4	2.20	-1.22×10^{-8}	37.4
D3: 4	59.5	1.18×10^5	2.53×10^4	3.90	-1.50×10^{-8}	39.9
D3: 5	66.7	1.29×10^5	2.61×10^4	5.46	-1.76×10^{-8}	41.3
D5: 1	25.2	6.52×10^5	2.14×10^5	0.06	-0.05×10^{-9}	38.2
D5: 2	38.4	7.74×10^5	2.21×10^5	1.36	-0.85×10^{-9}	40.7
D5: 3	49.4	9.41×10^5	2.30×10^5	2.34	-1.05×10^{-9}	42.9
D5: 4	59.5	1.14×10^6	2.37×10^5	4.04	-1.29×10^{-9}	45.5
D5: 5	66.7	1.23×10^6	2.50×10^5	5.59	-1.52×10^{-9}	47.0

Table 5.3. LES results; case D1, D3, and D5

	$x_{\rm LES}/\delta_0$	Re_θ		Re_τ		β		$K \times 10^{-7}$		$S = U_\infty/u_\tau$		$\frac{dp}{dx}^+ \times 10^{-3}$	
		Exp	LES	Exp	LES	Exp	LES	Exp	LES	Exp	LES	Exp	LES
1	25.2	6560	6560	2330	2410	ZPG	0.04	ZPG	-0.07	27.1	26.8	ZPG	0.13
2	38.4	8570	8120	2670	2570	1.16	1.10	-1.18	-1.20	28.5	28.6	2.75	2.90
3	49.4	8590	10150	2380	2750	1.58	1.97	-1.47	-1.49	29.3	30.0	3.71	4.30
4	59.5	10550	12550	2500	2910	2.76	3.52	-1.78	-1.83	31.2	31.8	5.42	6.39
5	66.7	11630	13900	2500	2930	4.27	5.03	-2.18	-2.16	33.3	33.1	7.72	8.09

Table 5.4. LES results; case D1 and corresponding experimental parameters for hot-wire measurements. All data from private communication with Z. Harun and I. Marusic.

of Reynolds number. The decrease in value at the end of the domain is caused by the decrease in pressure gradient close the wall as reported above in Figure 5.2. Note that the pressure distribution prescribed at the domain top is the same for all the cases, so is the resulting free-stream velocity. Therefore the profiles of K differs between cases are purely due to the difference in kinematic viscosity ν in each case. $S \equiv U_\infty/u_\tau$ shows a clear increase with Reynolds number and β.

Table 5.4 provides LES results of case D1 and their corresponding experimental results at five locations along the streamwise direction. The acceleration parameter K shows good agreement with the experiments, indicating the adverse-pressure gradient boundary conditions at the domain top results in the decreasing free-stream velocity sufficiently accurately. Note that the boundary condition for the streamwise velocity at the domain top is a Neumann type, see equation (5.4). The results at station 1, where the ZPGTBL is expected, agree well with the measurements. The location where the pressure gradient starts to increase is sufficiently downstream from the recycling plane ($x_{\rm ref}$) minimizing the effect of the sudden increase in the pressure gradient on the inflow generation

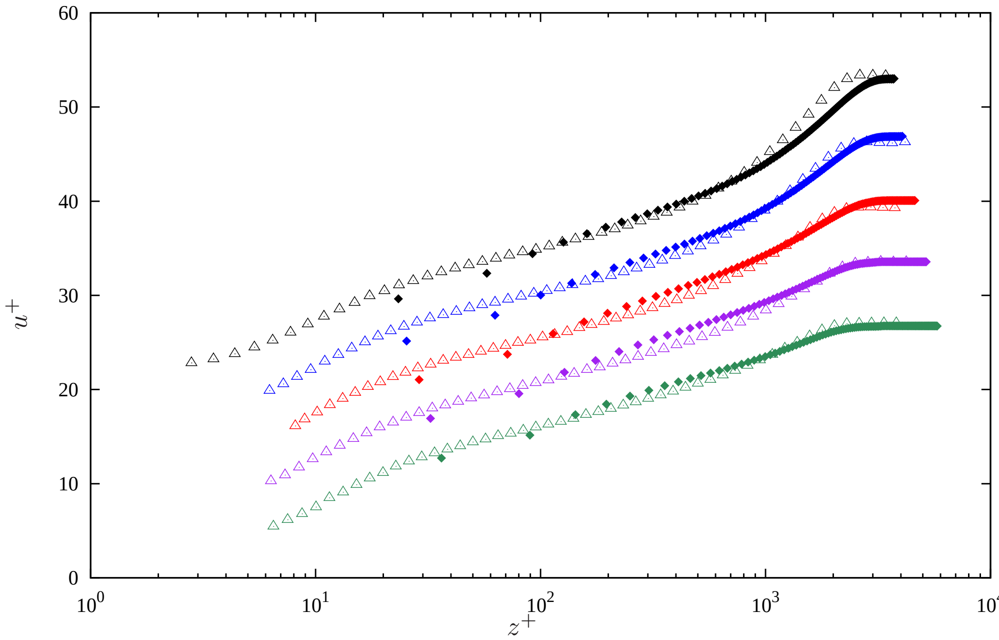

Figure 5.4. LES results; $\diamond$; case D1 and $\triangle$; corresponding experimental measurements (Z. harun & I. Marusic) of the mean velocity. Data are shifted up by 5 units for clarity. From the bottom, station 1 (green), 2 (purple), 3 (red), 4 (blue), and 5 (black)

scheme. Along the streamwise direction, however, the results indicate that the LES is experiencing the effect of adverse-pressure gradient a little too much compared to experiments, as shown by a steeper increase in a pressure gradient parameter β and S.

5.4.2 Mean velocity profiles

The effect discussed above can be seen in Figure 5.4, the mean streamwise velocity from case D1 normalized by the friction velocity u_τ at five locations along the streamwise direction. A reasonable agreement with the measurements was found. Qualitatively, our model reproduces the large wake region which is one of the most recognizable feature of an APGTBL (Monty et al. 2011). Similar trends are also found for the higher Reynolds-number cases; see Figure 5.5. It should be noted that the amount of amplified wake is somewhat similar at each measurement location irrespective of Reynolds number, which will be discussed in the following section.

Figure 5.6 show the velocity defect profiles at five locations from cases D1, D2, D3, D4, and D5 ($\diamond$) and experimental results ($\triangle$). The data are normalized by the friction velocity and defect thickness or the Rotta-Clauser parameter $\Delta \equiv \delta^* U_\infty^+$. Data are shifted by 5 units for clarity. From the bottom, station 1 ($\beta \approx 0$), station 2 ($\beta \approx 1.2$), station 3 ($\beta \approx 2.2$), station 4 ($\beta \approx 3.8$), and station 5 ($\beta \approx 5.4$). It is observed that the LES profiles for the flows with Reynolds number ranging from $\mathcal{O}(10^3)$ to $\mathcal{O}(10^5)$ almost coincide in the outer coordinates, indicating good collapse across the

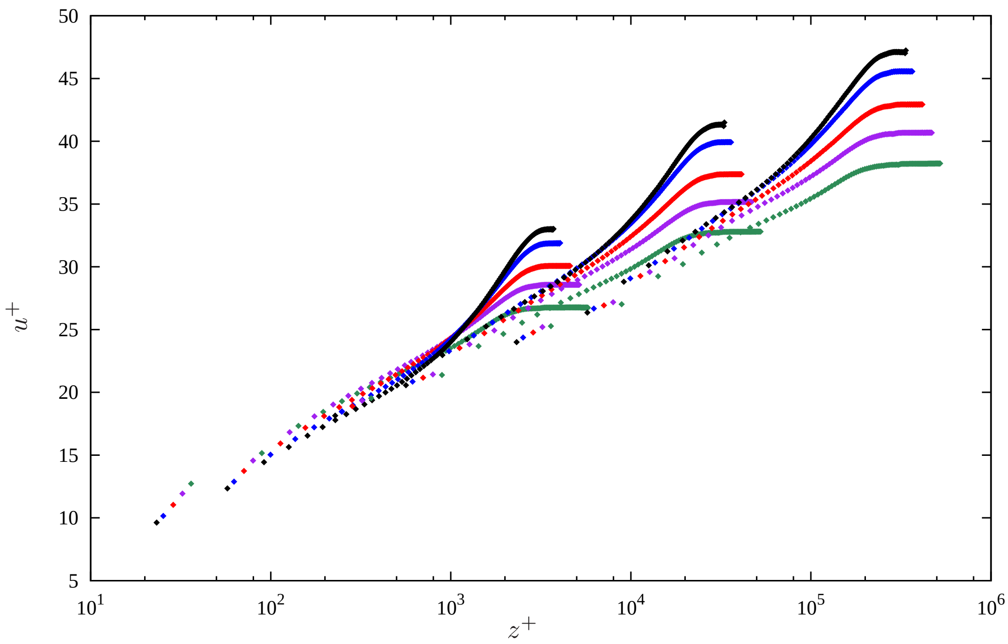

Figure 5.5. LES results; mean velocity from case D1, D3, D5. From the bottom, station 1 (green), 2 (purple), 3 (red), 4 (blue), and 5 (black).

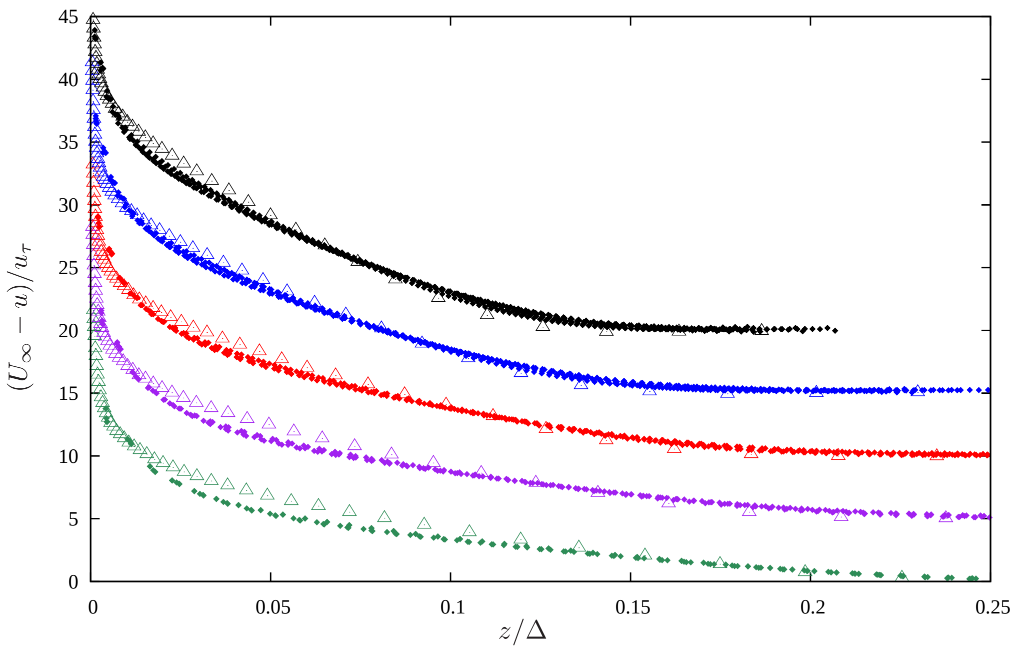

Figure 5.6. LES results; $\diamond$; LES and $\triangle$; corresponding experimental measurements of mean velocity defect profiles from case D1, D2, D3, D4, and D5. From the bottom, station 1 (green), 2 (purple), 3 (red), 4 (blue), and 5 (black). For clarity, data are shifted up by 5 units.

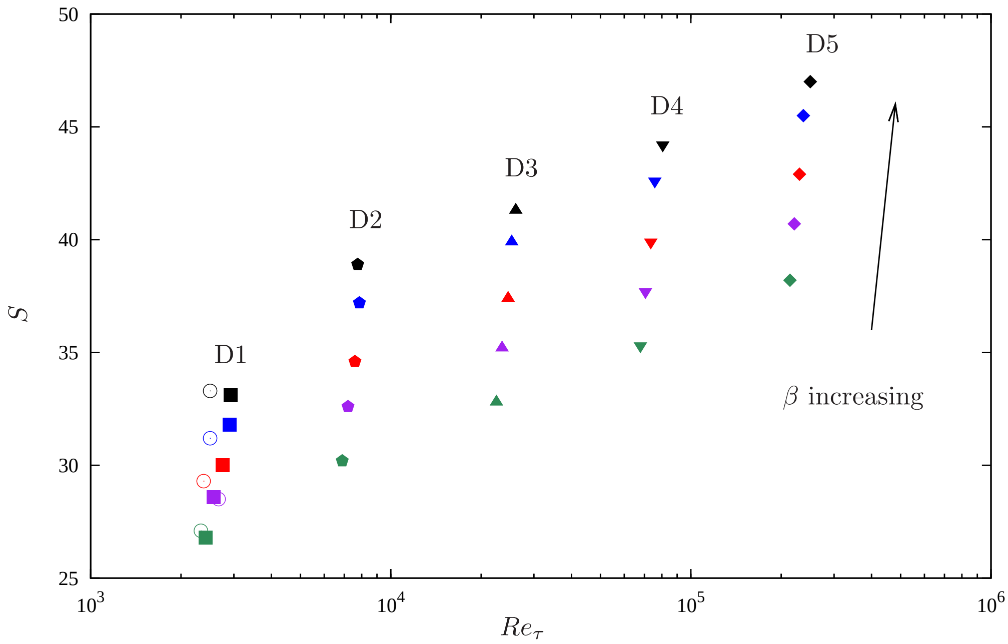

Figure 5.7. LES results; S-factor as a function of β at five locations from case D1, D2, D3, D4, and D5. From the bottom, station 1 ($\beta \approx 0$), station 2 ($\beta \approx 1.2$), station 3 ($\beta \approx 2.2$), station 4 ($\beta \approx 3.8$), and station5 ($\beta \approx 5.4$) in each case. Open circle: experiment, Z. Harun & I. Marusic (private communication)

outer part of boundary layer. Also the profiles are in good agreement with that of measurements.

5.4.3 S-factors

As mentioned in the earlier section, it was found that the amount of amplified wake was somewhat similar at each measurement location irrespective of Reynolds number. This can clearly be seen in Figure 5.7, showing S values at five locations from cases D1 to D5 with the experimental measurements as a function of local Re_τ. $S(\beta = 0)$ increases as $\log(Re_\tau)$ as found in ZPGTBL (see Chapter 3). The deviations of S from $S(\beta = 0)$ in each case are shown in Figure 5.8. Except for the lowest Reynolds number case: D1, the LES results appear to collapse well and lie on the empirical curve $S(Re_\tau, \beta) - S(Re_\tau, 0) = 4.1 \log(\beta) + 1.3$, which is a line of best fit. The solid line in Figure 5.8 is a relation for a flow in "quasi-equilibrium". This can be obtained as follows: Assuming that the mean velocity profile can be described by the Coles (1956) law of the wake, the Jones et al. (2001) formulation gives

$$S = U_\infty/u_\tau = \frac{1}{\kappa}\log Re_\tau + A - \frac{1}{3\kappa} + \frac{2\Pi}{\kappa}, \tag{5.6}$$

where A is the universal smooth-wall constant and κ is the Kármán constant. Here it is also assumed a constant $\kappa = 0.41$. For a "quasi-equilibrium" flow, defined to be an almost constant wake factor

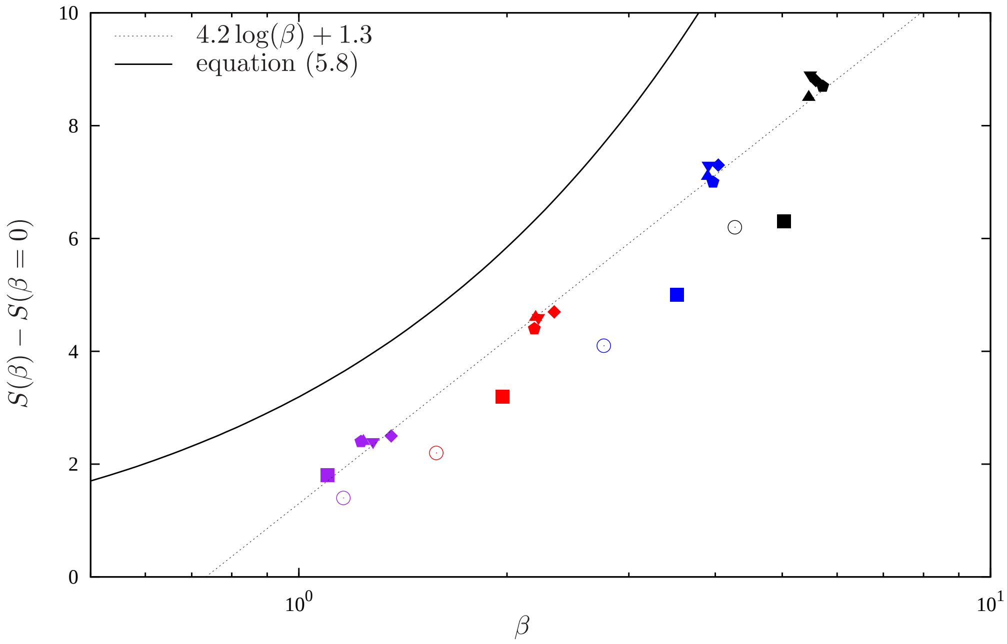

Figure 5.8. LES results; $S - S(\beta = 0)$ as a function of β. Notation follows Figure 5.7

Π, Perry et al. (2002) postulated the following functional relation between Π and β;

$$\beta = -1/2 + 1.21\Pi^{4/3} \quad \text{or} \quad \Pi = 0.86\,(\beta + 1/2)^{3/4}. \tag{5.7}$$

Then the deviation of S from $S(\beta = 0)$ can be evaluated as

$$S(\beta) - S(\beta = 0) = \frac{1.72}{\kappa}\left[(\beta + 1/2)^{3/4} - (1/2)^{3/4}\right], \tag{5.8}$$

which is shown in Figure 5.8. It should be noted again that the above discussion is for the APGTBL where the effect of variation in Π along the streamwise direction, represented by a parameter ξ (Perry et al. 2002) can be neglected. The present pressure-gradient distribution appears to produce a nonequilibrium APGTBL.

5.4.4 Turbulence intensities

Another feature of APG is the increase of turbulence intensity in the outer region when scaled with u_τ, resulting in a second peak, in addition to the peak in the near-wall region (e.g., Marusic and Perry 1995). Figure 5.9 plots the distributions of root-mean-square of streamwise velocity fluctuation for case D1 in comparison with the experimental measurements. Relatively large deviations close to the wall are due to the effect of the wall model. The LES appears to reproduce the general increase in turbulent intensities, in the outer region of the boundary layer, corresponding to increases in β in

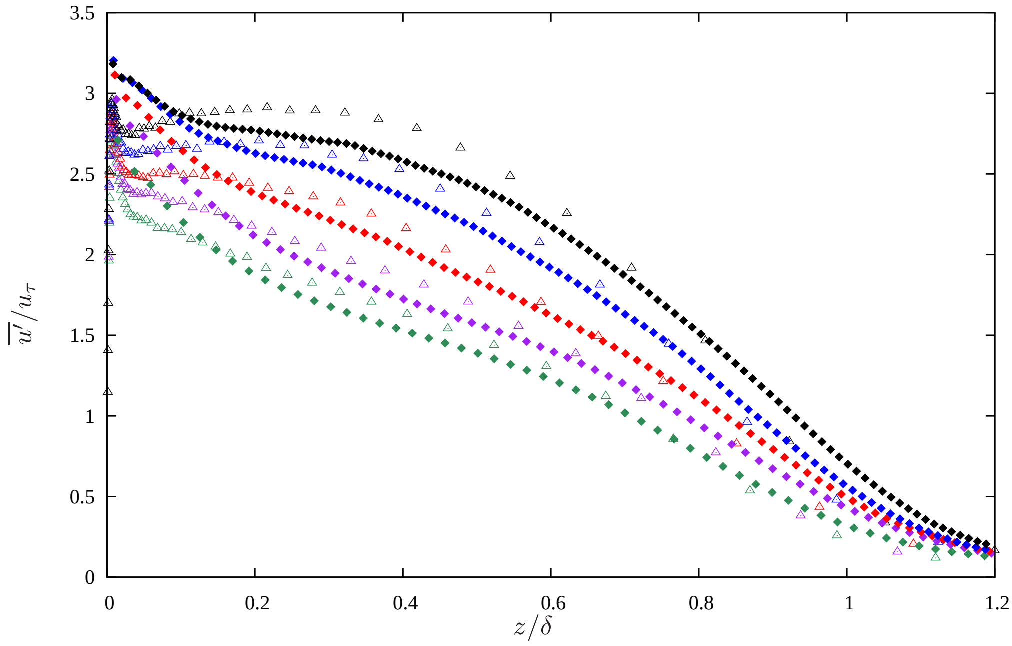

Figure 5.9. LES results; $\diamond$; case D1 and $\triangle$; corresponding experimental measurements of the streamwise turbulence intensity. δ is the local boundary layer thickness. From the bottom, station 1 (green), 2 (purple), 3 (red), 4 (blue), and 5 (black)

the streamwise direction. But the LES somewhat underestimates the experimental values and does not capture the turbulent intensity peak at the most downstream station.

Figures 5.10 show the root-mean-square of streamwise velocity fluctuation and the Reynolds shear stress at five locations from cases D1 to D5. Notations follow Figure 5.6. The streamwise velocity fluctuation profiles are in good agreement with that of measurements with small deviations, especially in the region close to the wall. Data are shifted by 1 unit for clarity. No data is available for the Reynolds shear stress. Reynolds number similarity is observed in the mean velocity defect, the turbulent intensity and the Reynolds shear stress profiles over two orders of magnitude in Reynolds number when β is held constant.

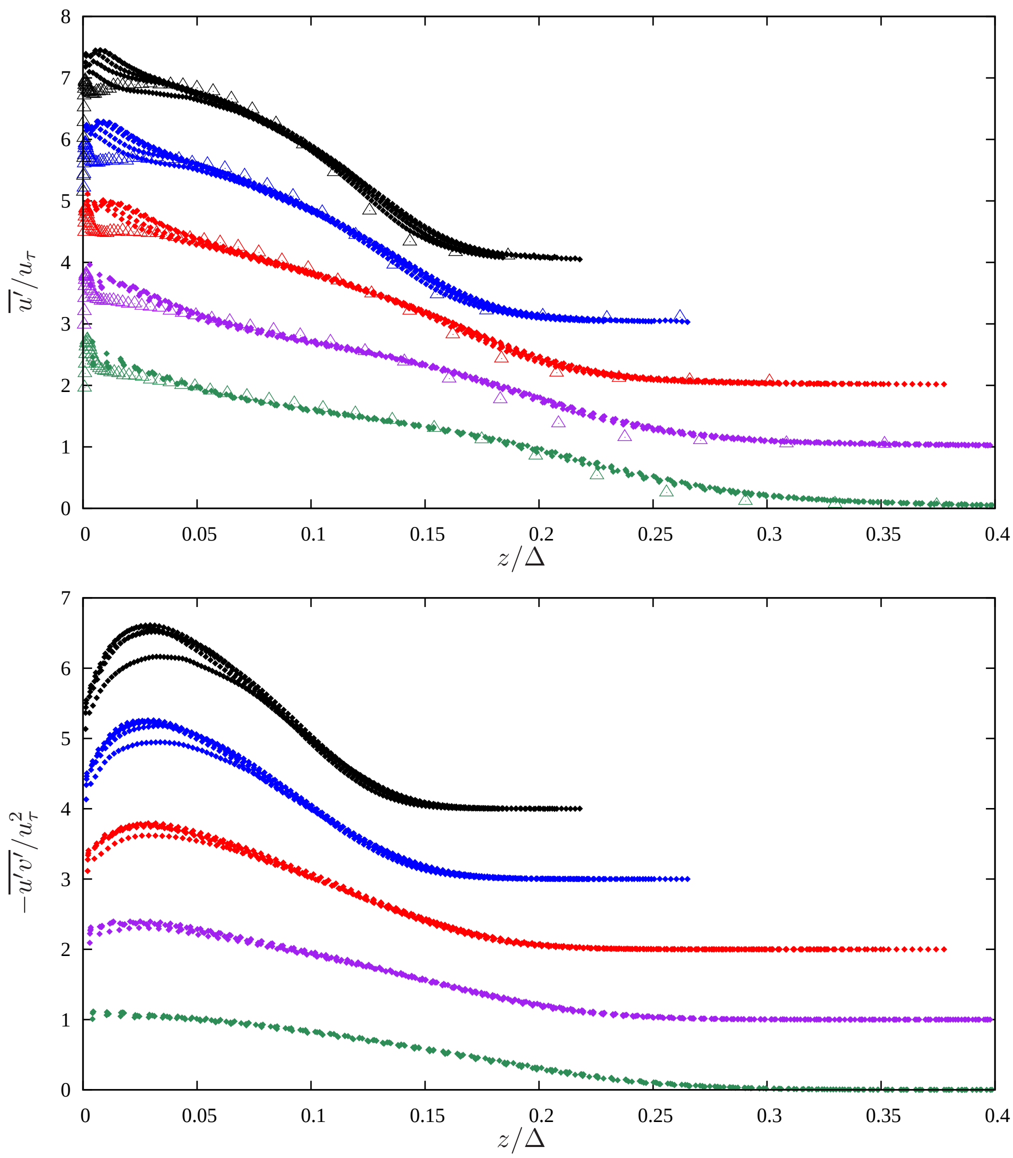

Figure 5.10. LES results; ◇; LES and △; corresponding experimental measurements of streamwise turbulence intensity and Reynolds shear stress from case D1, D2, D3, D4, and D5. From the bottom, station 1 (green), 2 (purple), 3 (red), 4 (blue), and 5 (black). For clarity, data are shifted up by 1 unit.

Chapter 6

Conclusions

The near-wall SGS model (Chung and Pullin 2009) is extended to perform LES of the spatially developing turbulent boundary layer over a flat and smooth wall. Chapter 2 is dedicated to presenting a numerical algorithm to solve the incompressible Navier-Stokes equations, which is suitable for simulating such a flow. In Chapter 3, LES of the ZPGTBL at very high Reynolds number were successfully performed and some possible scenarios on its behavior at infinite Reynolds number limit were explored. One intrinsic disadvantage of the current wall-model methodology is that it cannot probe the near-wall behavior of turbulent boundary layer. This has been presently addressed by the use of a predictive inner–outer wall model (Marusic et al. 2010a). The detailed statistics of the streamwise velocity in the inner-region of the ZPGTBL, as obtained from the combination of the LES and the predictive innter-outer model, were presented in Chapter 4. Finally, it has been shown in Chapter 5 that our wall-model is capable of reproducing some of the representative features of the turbulent boundary layer under an adverse-pressure gradient. In the following, we summarize the contributions of each of the chapters.

6.1 LES of the zero-pressure gradient turbulent boundary layer

The present near-wall approach utilizes an integration across the wall-adjacent layer coupled to an analytical model for the LES slip velocity at a raised virtual wall, derived from the basic stretched-vortex SGS model. The model parameters are h_ν^+, obtained empirically, and h_0. The “log law” (3.13) is obtained from the near-wall SGS ansatz with an assumption that attached, SGS structures have sizes that scale with linear distance from the wall. At the scale of the boundary layer thickness, the wall model can be interpreted as essentially a variable-strength vortex sheet attached to the wall. The wall model describes the internal sheet structure in a way that provides its strength, or velocity jump, given by (3.13), which couples this structure to the outer-flow LES. We note that some parts of the composite wall-model LES are independent of the stretched-vortex SGS model, for example, equation (3.11) describing the wall-normal velocity gradient. This could be used combined with other SGS closures. (3.13), however is particular to the stretched-vortex model. The present LES ansatz follows that of Chung and Pullin (2009) for unidirectional flow. Vector versions of the wall model on a surface where the flow direction changes can easily be formulated starting from an integration across the two components of the wall-parallel momentum equation.

Our LES indicates that a moderately complex wall model is capable of capturing the principal features, including Reynolds number effects, of the smooth-wall, zero-pressure gradient flat-plate turbulent boundary layer at essentially arbitrarily large Reynolds numbers and at cost independent of the Reynolds numbers. These LES are not perfect and display some near-wall effects associated with finite resolution and wall modeling. LES at even larger Reynolds numbers appear viable but could need higher precision arithmetic, at least for solving the auxiliary equation obtained from the wall-normal averaged, streamwise momentum equation. A useful feature of the model is that detailed resolution of the near-wall boundary layer is apparently not required to capture interesting flow properties such as the skin friction and the main features of the mean velocity profile in their dependence on Re_θ. The other side of the coin is that a possible disadvantage of our approach is that it provides no direct quantitative information on the near-wall region.

An interesting result of the LES over a range of Reynolds number inaccessible to both current DNS and experiment, is that, within the outer part of the turbulent boundary layer, the streamwise turbulence intensity scales with the wall friction velocity u_τ and with neither the free-stream velocity U_∞ nor a mixed-scaling combination of u_τ and U_∞. While it cannot be ruled out that this is an artifact of the wall model, the agreement with surface layer data over the small region of overlap lends some support to this conclusion. The main parameters of the LES are reasonably well described by well-known asymptotic models of the smooth-wall flat plate boundary layer.

6.2 Inner-layer predictions for the flat-plate turbulent boundary layer combining a predictive wall-model with LES

We have combined the present LES/wall-model with an inner–outer predictive model (Marusic et al. 2010a, Mathis et al. 2011) to calculate the statistics of the fluctuating streamwise velocity in the inner region of the zero-pressure gradient turbulent boundary layer. The LES provides a time series of the streamwise velocity signal within the logarithmic region, which is then filtered and used as an input for the inner–outer predictive model to provide a streamwise fluctuating velocity within a region which is inaccessible to both the present LES (with a wall model) at all Reynolds numbers and present experimental measurements at very high Reynolds numbers.

We first tested the effectiveness of this approach at intermediate Reynolds number, $Re_\tau \sim 7,300$,

$13,600$, and $19,000$. This reproduced velocity fluctuations within the near-wall region, approximately $0 \leq z^+ < 360$, with reasonable agreement with direct experimental measurements for the streamwise turbulent intensities. Although small discontinuities are observed in the predicted premultiplied energy spectra map, the composite model captures the general trend of its energy distribution including the inner peak and a suggestion of the existence of outer peak in the wall-normal profile of turbulent intensities. It has also been shown that the deviations of the predictions from experiments are of the same order as those obtained using the velocity signal taken from experiments as input to the inner–outer predictive model. Time series obtained from the LES used as input to the inner–outer predictive model then provided predictions at the substantially larger Reynolds numbers of $Re_\tau = 62,000, 100,000$, and $200,000$. Further, higher-order statistics comprising the skewness and kurtosis of the streamwise velocity fluctuations up to $Re_\tau \sim \mathcal{O}(10^5)$ were also obtained and shown to give good agreement with experimental measurements at intermediate Reynolds numbers.

The LES-predictive inner–outer results support a log-like increase in the inner peak of the streamwise turbulence intensity with increasing Re_τ and provide prediction within a gap in $\log(Re_\tau)$ space between present laboratory measurements and surface-layer, atmospheric experiments. Overall, the LES appears to successfully capture the very-large-scale motions that are hypothesized to drive this increase within the predictive inner–outer model.

Two principal advances of the present work can be summarized as follows: First, velocity time series obtained from LES and used as input to the inner–outer predictive model can be used to extend the wall-normal range of the LES well into the near-wall region. This has been demonstrated for the zero-pressure gradient, smooth-wall turbulent boundary layer, but the methodology appears sufficiently robust to be applicable to other wall-bounded turbulent flows such as pipe and channel flows and boundary layers in the presence of pressure gradients. Second, the results have provided predictions of the dependence of the near-wall peak in streamwise turbulent intensities that are beyond the range of current laboratory experimental facilities.

6.3 LES of the adverse-pressure gradient turbulent boundary layer

Owing to the local nature of our wall model and the interior SGS model, the present wall-model LES is applicable to the adverse-pressure gradient turbulent boundary layer. The pressure gradient reported in the experimental studies (e.g., Marusic and Perry 1995, Harun et al. 2010, Monty et al. 2011) were successfully reproduced in simulation by directly applying pressure as a boundary condition on the upper surface of the domain. We first compared results at $Re_\tau \approx 2 \times 10^3$ with experimental measurements using a relatively long domain, $L_x = 72\delta_0$. Except for the region close to the wall, the mean velocity profiles and turbulent intensity were found to be in reasonable agreement with experiments, including the pressure gradient parameters, β, K, and $(dp/dx)^+$. The recognizable features of the APGTBL, such as an amplified wake in the mean velocity profile and an increase in turbulent intensity in the outer region were reproduced. Most importantly, it was found that our wall ODE was capable of simulating the correct distribution of the wall shear stress along the streamwise direction under an adverse-pressure gradient.

We also computed the "nonequilibrium" APGTBL at Reynolds number up to $Re_\tau \approx 2\times 10^5$ using the same profile of pressure-gradient distribution, so that the flow experienced the same upstream history of the pressure gradient. The resulting distribution of β was found not to be very sensitive to the Reynolds number itself and showed similar profiles for the various LES performed. The mean velocity defect and the turbulent intensity profiles, when normalized by the friction velocity u_τ and Rotta-Clauser parameter Δ, shows good collapse in the outer part of boundary layer over a wide range of Reynolds number at each measurement station, where almost matched β is achieved.

Finally we remark that our LES approach to wall-bounded turbulent flows is not limited to either boundary layers over flat surfaces or even to attached flow and can, with further development, be applied to three-dimensional boundary layers over curved surfaces and to flow with separation. These applications are left for future work.

Appendix A

Numerical Details

A.1 SGS model implementation

As discussed previously in §3.2, our subgrid-scale model takes the velocity u_i and velocity gradient tensor $\partial u_i/\partial x_j$ as a part of inputs. With respect to implementation, some complexity is caused by the staggered-grid formulation of variables (see Figure 2.3). As a result, the derivatives of velocity components naturally obtained in the process of computing nonlinear terms in the Navier-Stokes equation locate at several different positions on the grid. Our choice is to interpolate values of necessary variables into one location for each computational cell. The sub-grid stresses, provided by the SGS model, will then be interpolated into various locations necessary to provide $\partial T_{ij}/\partial x_i$ in the generically filtered Navier–Stokes equation (3.1). Our scheme is described in Figure A.1. There are two choices for the location where the SGS model can be defined, either at the cell center or at the cell corner. The cell corner is used for all the results presented in this thesis owing to the boundary issues. The other choice (defining at the cell center), however, has one possible advantage that the continuity constraint is assured to the machine precision from the Poisson-pressure equation, which is originally defined at the cell center. It might improve the numerical stability but it is not pursued presently.

A.2 Morinishi's schemes

The first derivative at midpoints, the second derivative with standard collocated formulas and the interpolations are evaluated with fourth-order accuracy as

$$\left(\frac{df}{dx}\right)_{i-1/2} = \frac{-f_{i+1}+27f_i-27f_{i-1}+f_{i-2}}{24\Delta x}+\mathcal{O}(\Delta x^4), \tag{A.1}$$

$$\left(\frac{d^2f}{dx^2}\right)_{i} = \frac{-f_{i+2}+16f_{i+1}-30f_i+16f_{i+1}-f_{i-2}}{12\Delta x^2}+\mathcal{O}(\Delta x^4), \tag{A.2}$$

$$f_{i-1/2} = \frac{-f_{i+1}+9f_i+9f_{i-1}-f_{i-2}}{16}+\mathcal{O}(\Delta x^4), \tag{A.3}$$

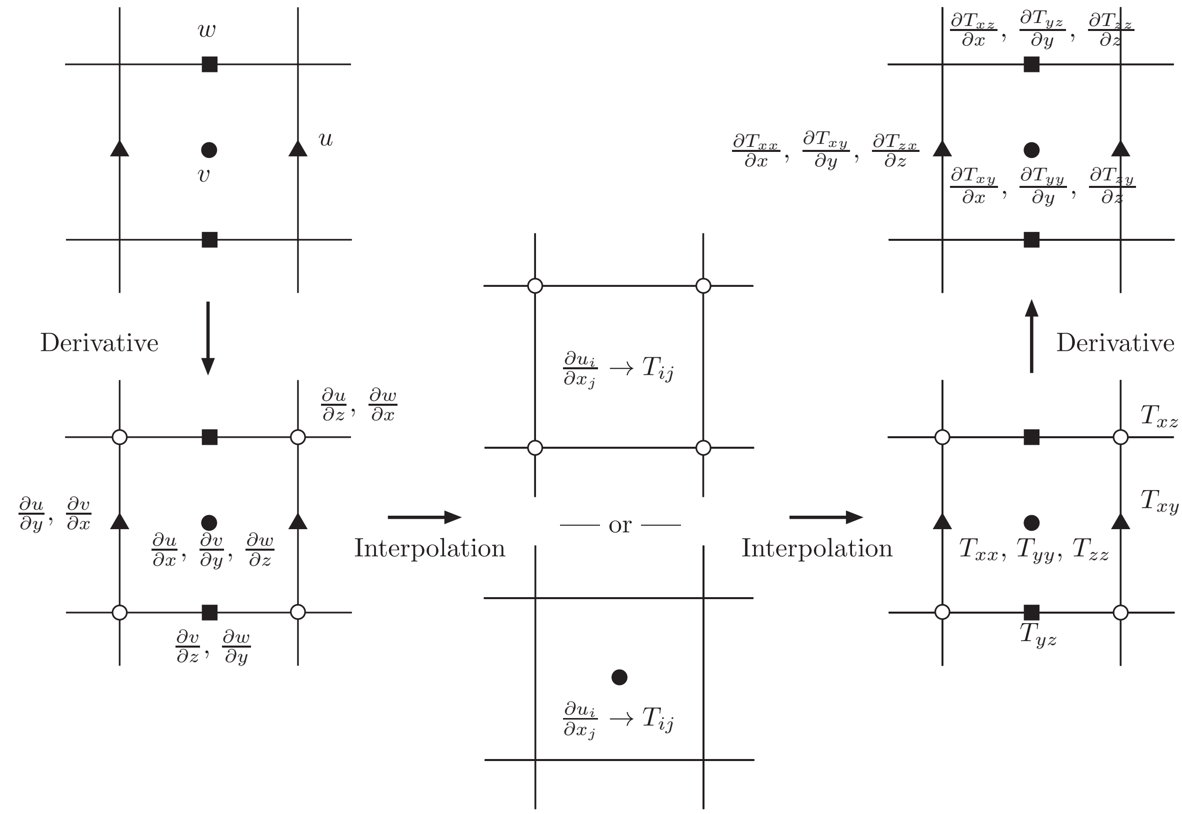

Figure A.1. Staggered-grid formulation for the subgrid-scale model. At each stage, each marker represents the same kind of variables described.

respectively. Following the notations of Morinishi et al. (1998), x represents the streamwise direction, y, the wall-normal and z, the spanwise direction. The finite-difference operator and the interpolation operator with stencil n acting on f with respect to x_1 are denoted as

$$\left.\frac{\delta_n f}{\delta_n x_1}\right|_{x_1,x_2,x_3} \equiv \frac{f(x_1 + n\Delta x_1/2, x_2, x_3) - f(x_1 - n\Delta x_1/2, x_2, x_3)}{n\Delta x_1}, \tag{A.4}$$

and

$$\left.\overline{f}^{(nx_1)}\right|_{x_1,x_2,x_3} \equiv \frac{f(x_1 + n\Delta x_1/2, x_2, x_3) + f(x_1 - n\Delta x_1/2, x_2, x_3)}{2}, \tag{A.5}$$

respectively. Using these notations, Morinishi et al. (1998) presented fully conservative, fourth-order-accurate convective schemes for a staggered-grid system as follows

$$(\mathrm{Div}-\mathrm{S4})_i \equiv \frac{9}{8}\frac{\delta_1}{\delta_1 x_j}\left[\left(\frac{9}{8}\overline{u_j}^{(1x_i)}-\frac{1}{8}\overline{u_j}^{(3x_i)}\right)\overline{u_i}^{(1x_j)}\right]-\frac{1}{8}\frac{\delta_3}{\delta_3 x_j}\left[\left(\frac{9}{8}\overline{u_j}^{(1x_i)}-\frac{1}{8}\overline{u_j}^{(3x_i)}\right)\overline{u_i}^{(3x_j)}\right],$$

$$(\mathrm{Adv}-\mathrm{S4})_i \equiv \frac{9}{8}\overline{\left(\frac{9}{8}\overline{u_j}^{(1x_i)}-\frac{1}{8}\overline{u_j}^{(3x_i)}\right)\frac{\delta_1 u_i}{\delta_1 x_j}}^{(1x_j)}-\frac{1}{8}\overline{\left(\frac{9}{8}\overline{u_j}^{(1x_i)}-\frac{1}{8}\overline{u_j}^{(3x_i)}\right)\frac{\delta_3 u_i}{\delta_3 x_j}}^{(3x_j)},$$

$$(\mathrm{Skew}-\mathrm{S4}) \equiv \frac{1}{2}(\mathrm{Div}-\mathrm{S4})+\frac{1}{2}(\mathrm{Adv}-\mathrm{S4}),$$

where (Div-S4), (Adv-S4), and (Skew-S4) denote the divergence form, advective form, and skew-symmetric form of convective term of the fourth-order-accurate staggered-grid system, respectively.

A.3 Staggered-grid system in two directions and FFT in the other

Note that in our numerical scheme, a staggered arrangement is used in the x-z plane only and that no staggering is used in the y-direction. The y-direction is assumed periodic and all the velocity components and the pressure are expanded in Fourier series along this direction. Let $\partial/\partial y_F$ denotes the derivative in Fourier space. Then both the divergence and advection forms of the convective schemes are written as

$$(\mathrm{Div}-\mathrm{S4})_x = \frac{9}{8}\frac{\delta_1}{\delta_1 x}\left[\left(\frac{9}{8}\overline{u}^{(1x)}-\frac{1}{8}\overline{u}^{(3x)}\right)\overline{u}^{(1x)}\right]-\frac{1}{8}\frac{\delta_3}{\delta_3 x}\left[\left(\frac{9}{8}\overline{u}^{(1x)}-\frac{1}{8}\overline{u}^{(3x)}\right)\overline{u}^{(3x)}\right]$$
$$+\frac{9}{8}\frac{\delta_1}{\delta_1 y}\left[\left(\frac{9}{8}\overline{v}^{(1x)}-\frac{1}{8}\overline{v}^{(3x)}\right)\overline{u}^{(1y)}\right]-\frac{1}{8}\frac{\delta_3}{\delta_3 y}\left[\left(\frac{9}{8}\overline{v}^{(1x)}-\frac{1}{8}\overline{v}^{(3x)}\right)\overline{u}^{(3y)}\right]+\frac{\partial}{\partial z_{\mathrm{F}}}\left(\frac{9}{8}\overline{w}^{(1x)}-\frac{1}{8}\overline{w}^{(3x)}\right)u,$$

$$(\mathrm{Div}-\mathrm{S4})_y = \frac{9}{8}\frac{\delta_1}{\delta_1 x}\left[\left(\frac{9}{8}\overline{u}^{(1y)}-\frac{1}{8}\overline{u}^{(3y)}\right)\overline{v}^{(1x)}\right]-\frac{1}{8}\frac{\delta_3}{\delta_3 x}\left[\left(\frac{9}{8}\overline{u}^{(1y)}-\frac{1}{8}\overline{u}^{(3y)}\right)\overline{v}^{(3x)}\right]$$
$$+\frac{9}{8}\frac{\delta_1}{\delta_1 y}\left[\left(\frac{9}{8}\overline{v}^{(1y)}-\frac{1}{8}\overline{v}^{(3y)}\right)\overline{v}^{(1y)}\right]-\frac{1}{8}\frac{\delta_3}{\delta_3 y}\left[\left(\frac{9}{8}\overline{v}^{(1y)}-\frac{1}{8}\overline{v}^{(3y)}\right)\overline{v}^{(3y)}\right]+\frac{\partial}{\partial z_{\mathrm{F}}}\left(\frac{9}{8}\overline{w}^{(1y)}-\frac{1}{8}\overline{w}^{(3y)}\right)v,$$

$$(\mathrm{Div}-\mathrm{S4})_z = \frac{9}{8}\frac{\delta_1}{\delta_1 x}\left[u\overline{w}^{(1x)}\right]-\frac{1}{8}\frac{\delta_3}{\delta_3 x}\left[u\overline{w}^{(3x)}\right]+\frac{9}{8}\frac{\delta_1}{\delta_1 y}\left[v\overline{w}^{(1y)}\right]-\frac{1}{8}\frac{\delta_3}{\delta_3 y}\left[v\overline{w}^{(3y)}\right]+\frac{\partial}{\partial z_{\mathrm{F}}}ww,$$

$$(\mathrm{Adv-S4})_x = \frac{9}{8}\overline{\left(\frac{9}{8}\overline{u}^{(1x)} - \frac{1}{8}\overline{u}^{(3x)}\right)\frac{\delta_1 u}{\delta_1 x}}^{(1x)} - \frac{1}{8}\overline{\left(\frac{9}{8}\overline{u}^{(1x)} - \frac{1}{8}\overline{u}^{(3x)}\right)\frac{\delta_3 u}{\delta_3 x}}^{(3x)}$$
$$+\frac{9}{8}\overline{\left(\frac{9}{8}\overline{v}^{(1x)} - \frac{1}{8}\overline{v}^{(3x)}\right)\frac{\delta_1 u}{\delta_1 y}}^{(1y)} - \frac{1}{8}\overline{\left(\frac{9}{8}\overline{v}^{(1x)} - \frac{1}{8}\overline{v}^{(3x)}\right)\frac{\delta_3 u}{\delta_3 y}}^{(3y)} + \left(\frac{9}{8}\overline{w}^{(1x)} - \frac{1}{8}\overline{w}^{(3x)}\right)\frac{\partial}{\partial z_{\mathrm{F}}}u,$$

$$(\mathrm{Adv-S4})_y = \frac{9}{8}\overline{\left(\frac{9}{8}\overline{u}^{(1y)} - \frac{1}{8}\overline{u}^{(3y)}\right)\frac{\delta_1 v}{\delta_1 x}}^{(1x)} - \frac{1}{8}\overline{\left(\frac{9}{8}\overline{u}^{(1y)} - \frac{1}{8}\overline{u}^{(3y)}\right)\frac{\delta_3 v}{\delta_3 x}}^{(3x)}$$
$$+\frac{9}{8}\overline{\left(\frac{9}{8}\overline{v}^{(1y)} - \frac{1}{8}\overline{v}^{(3y)}\right)\frac{\delta_1 v}{\delta_1 y}}^{(1y)} - \frac{1}{8}\overline{\left(\frac{9}{8}\overline{v}^{(1y)} - \frac{1}{8}\overline{v}^{(3y)}\right)\frac{\delta_3 v}{\delta_3 y}}^{(3y)} + \left(\frac{9}{8}\overline{w}^{(1y)} - \frac{1}{8}\overline{w}^{(3y)}\right)\frac{\partial}{\partial z_{\mathrm{F}}}v,$$

$$(\mathrm{Adv-S4})_z = \frac{9}{8}\overline{u\frac{\delta_1 w}{\delta_1 x}}^{(1x)} - \frac{1}{8}\overline{u\frac{\delta_3 w}{\delta_3 x}}^{(3x)} + \frac{9}{8}\overline{v\frac{\delta_1 w}{\delta_1 y}}^{(1y)} - \frac{1}{8}\overline{v\frac{\delta_3 w}{\delta_3 y}}^{(3y)} + w\frac{\partial}{\partial z_{\mathrm{F}}}w.$$

A.4 Discrete conservations and boundary conditions for the channel flow case

The ghost-point scheme is employed for the fourth-order-accurate scheme. The points are extended beyond the boundaries so that a consistent stencil can be used as in the interior. The scheme is summarized in Figure A.2.

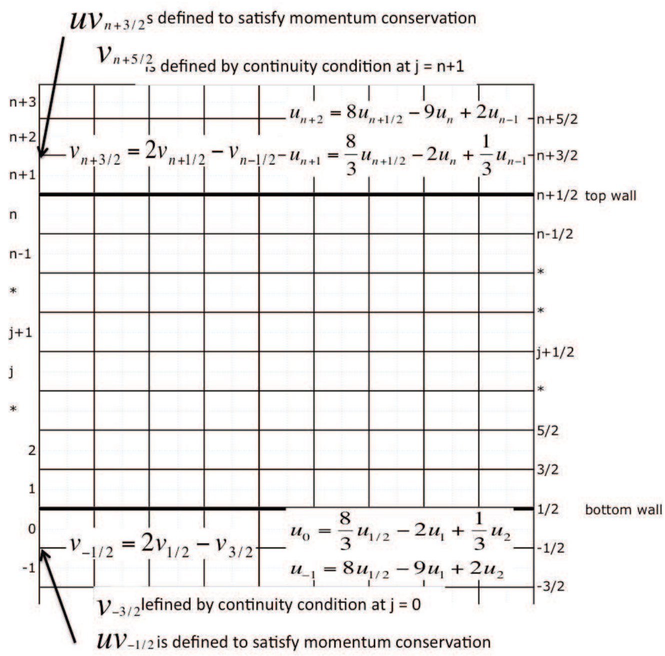

Figure A.2. The ghost-cell values for the fourth-order scheme

The boundary conditions (values at ghost points) are designed to ensure global conservation in the nonperiodic directions, i.e., so that the following discrete relation holds, (equi-spaced grids are assumed for simplicity)

$$\sum_{j=1}^{N} \Delta y \frac{\delta \phi}{\delta y}\Big|_j = \phi_{N+1/2} - \phi_{1/2}, \tag{A.6}$$

where $\delta\phi/\delta y$ is an arbitrary finite-difference operator. $j = 1/2$ and $j = N + 1/2$ denote the lower and upper walls, respectively. Its continuous equivalent is

$$\int_{\text{lowerwall}}^{\text{upperwall}} \frac{\partial \phi}{\partial y} dy = [\phi]_{\text{lowerwall}}^{\text{upperwall}}. \tag{A.7}$$

Owing to the spatial periodicity in the other directions in the channel-flow setting, only the nonperiodic direction needs to be considered.

A.4.1 Discrete conservation of mass

The wall-normal derivative seen in the continuity equation is integrated over the computational domain Ω.

A.4.1.1 Second-order-accurate scheme

$$\begin{aligned} \int_\Omega \left(\frac{\delta_1 v}{\delta_1 y}\right) dV &= \iint_{z\,x} \sum_{j=1}^{N} \Delta y \left(\frac{v_{j+1/2} - v_{j-1/2}}{\Delta y}\right) dxdz \\ &= \iint_{z\,x} \left(v_{N+1/2} - v_{1/2}\right) dxdz. \end{aligned} \tag{A.8}$$

Mass is conserved without any ghost points.

A.4.1.2 Fourth-order-accurate scheme

$$\begin{aligned} \int_\Omega \left(\frac{9}{8}\frac{\delta_1 v}{\delta_1 y} - \frac{1}{8}\frac{\delta_3 v}{\delta_3 y}\right) dV &= \iint_{z\,x} \sum_{j=1}^{N} \Delta y \left(\frac{-v_{j+3/2} + 27 v_{j+1/2} - 27 v_{j-1/2} + v_{j-3/2}}{24 \Delta y}\right) dxdz \\ &= \iint_{z\,x} \frac{1}{24} \left(-v_{N+3/2} + 26 v_{N+1/2} - v_{N-1/2}\right. \\ &+ \left. v_{3/2} - 26 v_{1/2} + v_{-1/2}\right) dxdz. \end{aligned} \tag{A.9}$$

For the above equation to satisfy (A.6) the following boundary values at ghost points $j = N + 3/2$ and $j = -1/2$ are obtained:

$$
\begin{aligned}
v_{3/2} - 26v_{1/2} + v_{-1/2} &= -24v_{1/2}, && \text{(A.10)}\\
-v_{N+3/2} + 26v_{N+1/2} - v_{N-1/2} &= -24v_{N+1/2}. && \text{(A.11)}
\end{aligned}
$$

Hence,

$$
\begin{aligned}
v_{-1/2} &= 2v_{1/2} - v_{3/2}, && \text{(A.12)}\\
v_{N+3/2} &= 2v_{N+1/2} - v_{N-1/2}. && \text{(A.13)}
\end{aligned}
$$

This is equivalent to approximating $\partial^2 v/\partial y^2 = 0$ with second-order-accurate central differences, which is reasonable for a solid wall (no-slip) condition

$$
\left.\frac{\delta^2 v}{\delta y^2}\right|_{wall} = 0 + \mathcal{O}(\Delta y^2). \tag{A.14}
$$

With the above relation, the scheme gives the first derivative with first-order accuracy close to the wall

$$
\left.\frac{\delta v}{\delta y}\right|_{3/2} = \frac{\partial v}{\partial y} - \frac{1}{48}\frac{\partial^2 v}{\partial y^2}\Delta y + \mathcal{O}(\Delta y^2). \tag{A.15}
$$

A.4.2 Discrete conservation of momentum

The convection term that contains the wall-normal derivative in the momentum equation in the y-direction is integrated over the computational domain.

A.4.2.1 Second-order-accurate scheme

$$
\begin{aligned}
\int_\Omega \left(\frac{\delta_1 \overline{u}^{(1y)}\overline{v}^{(1x)}}{\delta_1 y}\right) dV &= \int_z\int_x \sum_{j=1}^{N} \Delta y \left(\frac{(\overline{v}^{(1x)}u)_{j+1/2} - (\overline{v}^{(1x)}u)_{j-1/2}}{\Delta y}\right) dxdz\\
&= \int_z\int_x \sum_{j=1}^{N} \left((\overline{v}^{(1x)}u)_{j+1/2} - (\overline{v}^{(1x)}u)_{j-1/2}\right) dxdz\\
&= \int_z\int_x \left((\overline{v}^{(1x)}u)_{N+1/2} - (\overline{v}^{(1x)}u)_{1/2}\right) dxdz. && \text{(A.16)}
\end{aligned}
$$

Momentum is conserved without any ghost points.

A.4.2.2 Fourth-order-accurate scheme

$$
\begin{aligned}
&\int_\Omega \left(\frac{9}{8}\frac{\delta_1}{\delta_1 y}\left[\overline{v}^{(x)}\overline{u}^{(1y)}\right] - \frac{1}{8}\frac{\delta_3}{\delta_3 y}\left[\overline{v}^{(x)}\overline{u}^{(3y)}\right]\right) dV \\
= \;& \iint_{z\,x} \sum_{j=1}^{N} \Delta y \left(\frac{-(\overline{v}^{(x)}\overline{u}^{(3y)})_{j+3/2} + 27(\overline{v}^{(x)}\overline{u}^{(1y)})_{j+1/2} - 27(\overline{v}^{(x)}\overline{u}^{(1y)})_{j-1/2} + (\overline{v}^{(x)}\overline{u}^{(3y)})_{j-3/2}}{24\Delta y} \right) dxdz \\
= \;& \iint_{z\,x} \sum_{j=1}^{N} \frac{1}{24} \left((uv)_j\right) dxdz, \qquad \text{(A.17)}
\end{aligned}
$$

where, $\overline{v}^{(x)} = \frac{9}{8}\overline{v}^{(1x)} - \frac{1}{8}\overline{v}^{(3x)}$ and

$$
\begin{aligned}
(uv)_1 &= \frac{1}{24}\left(-(\overline{v}^{(x)}\overline{u}^{(3y)})_{5/2} + 27(\overline{v}^{(x)}\overline{u}^{(1y)})_{3/2} - 27(\overline{v}^{(x)}\overline{u}^{(1y)})_{1/2} + (\overline{v}^{(x)}\overline{u}^{(3y)})_{-1/2}\right), \\
(uv)_2 &= \frac{1}{24}\left(-(\overline{v}^{(x)}\overline{u}^{(3y)})_{7/2} + 27(\overline{v}^{(x)}\overline{u}^{(1y)})_{5/2} - 27(\overline{v}^{(x)}\overline{u}^{(1y)})_{3/2} + (\overline{v}^{(x)}\overline{u}^{(3y)})_{1/2}\right), \\
(uv)_3 &= \frac{1}{24}\left(-(\overline{v}^{(x)}\overline{u}^{(3y)})_{9/2} + 27(\overline{v}^{(x)}\overline{u}^{(1y)})_{7/2} - 27(\overline{v}^{(x)}\overline{u}^{(1y)})_{5/2} + (\overline{v}^{(x)}\overline{u}^{(3y)})_{3/2}\right), \\
&\vdots \\
(uv)_N &= \frac{1}{24}\left(-(\overline{v}^{(x)}\overline{u}^{(3y)})_{N+5/2} + 27(\overline{v}^{(x)}\overline{u}^{(1y)})_{N+3/2} - 27(\overline{v}^{(x)}\overline{u}^{(1y)})_{N+1/2} + (\overline{v}^{(x)}\overline{u}^{(3y)})_{N-1/2}\right).
\end{aligned}
$$

Thus for the equation (A.17) to satisfy (A.6), i.e.,

$$
\iint_{z\,x} \sum_{j=1}^{N} \frac{1}{24}(uv)_j dxdz = \iint_{z\,x} \frac{1}{24}\left((uv)_{N+1/2} - (uv)_{1/2}\right), \qquad \text{(A.18)}
$$

the following boundary conditions are required:

$$
\begin{aligned}
(\overline{v}^{(x)}\overline{u}^{(3y)})_{-1/2} &= 27(\overline{v}^{(x)}\overline{u}^{(1y)})_{1/2} - (\overline{v}^{(x)}\overline{u}^{(3y)})_{3/2} - (\overline{v}^{(x)}\overline{u}^{(3y)})_{1/2} - 24(uv)_{1/2}, \qquad \text{(A.19)} \\
(\overline{v}^{(x)}\overline{u}^{(3y)})_{N+3/2} &= 27(\overline{v}^{(x)}\overline{u}^{(1y)})_{N+1/2} - (\overline{v}^{(x)}\overline{u}^{(3y)})_{N-1/2} - (\overline{v}^{(x)}\overline{u}^{(3y)})_{N+1/2} - 24(uv)_{N+1/2}. \qquad \text{(A.20)}
\end{aligned}
$$

Similar analysis should be applied to $(v\overline{w}^{(3y)})_{-1/2}$ and $(v\overline{w}^{(3y)})_{N+3/2}$.

A.4.3 Other conditions for fourth-order-accurate schemes

The values of u_0, u_{-1}, u_{N+1}, and u_{N+2} will be obtained as a solution of the following equations:

$$\frac{9}{8}\overline{u}^{(1y)} - \frac{1}{8}\overline{u}^{(3y)}\Big|_{1/2} = u_{1/2}, \tag{A.21}$$

$$\frac{\delta^3 u}{\delta y^3}\Big|_{1/2} = 0 \quad \text{(at bottom wall)}. \tag{A.22}$$

With this condition the viscous terms satisfies the desecrate conservation in the wall-normal direction with fourth-order accuracy. The viscous term that contains a wall-normal derivative in the x-momentum equation is integrated over the computational domain

$$\begin{aligned}\int_\Omega \left(\frac{\delta}{\delta y}\frac{\delta u}{\delta y}\right) dV &= \iint_{z\,x} \frac{1}{24}\left(-\frac{\delta u}{\delta y}\Big|_{N+3/2} + 26\frac{\delta u}{\delta y}\Big|_{N+1/2} - \frac{\delta u}{\delta y}\Big|_{N-1/2}\right. \\ &+ \left.\frac{\delta u}{\delta y}\Big|_{3/2} - 26\frac{\delta u}{\delta y}\Big|_{1/2} + \frac{\delta u}{\delta y}\Big|_{-1/2}\right) dxdz. \end{aligned} \tag{A.23}$$

Hence we need the following

$$\frac{\delta u}{\delta y}\Big|_{-1/2} = 2\frac{\delta u}{\delta y}\Big|_{1/2} - \frac{\delta u}{\delta y}\Big|_{3/2}, \tag{A.24}$$

$$\frac{\delta u}{\delta y}\Big|_{N+3/2} = 2\frac{\delta u}{\delta y}\Big|_{N+1/2} - \frac{\delta u}{\delta y}\Big|_{N-1/2}. \tag{A.25}$$

With equation (A.14), we get the condition (A.22). Similarly with the upper wall, also with stream-wise velocity w, solving the equation gives,

$$u_0 = \frac{8}{3}u_{1/2} - 2u_1 + \frac{1}{3}u_2, \tag{A.26}$$

$$u_{-1} = 8u_{1/2} - 9u_1 + 2u_2, \tag{A.27}$$

$$u_{N+1} = \frac{8}{3}u_{N+1/2} - 2u_N + \frac{1}{3}u_{N-1}, \tag{A.28}$$

$$u_{N+2} = 8u_{N+1/2} - 9u_N + 2u_{N-1}, \tag{A.29}$$

$$w_0 = \frac{8}{3}w_{1/2} - 2w_1 + \frac{1}{3}w_2, \tag{A.30}$$

$$w_{-1} = 8w_{1/2} - 9w_1 + 2w_2, \tag{A.31}$$

$$w_{N+1} = \frac{8}{3}w_{N+1/2} - 2w_N + \frac{1}{3}w_{N-1}, \tag{A.32}$$

$$w_{N+2} = 8w_{N+1/2} - 9w_N + 2w_{N-1}. \tag{A.33}$$

With the above conditions, Taylor expansion analysis gives the order of accuracy of second derivatives as,

$$\left.\frac{\delta^2 u}{\delta y^2}\right|_1 = \frac{\partial^2 u}{\partial y^2} + \frac{7}{72}\frac{\partial^3 u}{\partial y^3}\Delta y + \mathcal{O}(\Delta y^2), \tag{A.34}$$

$$\left.\frac{\delta^2 u}{\delta y^2}\right|_2 = \frac{\partial^2 u}{\partial y^2} - \frac{1}{108}\frac{\partial^3 u}{\partial y^3}\Delta y + \mathcal{O}(\Delta y^2), \tag{A.35}$$

close to the wall for the general case. The continuity equation at points $j = 0$ and $j = N + 1$ gives the values for $v_{-3/2}$ and $v_{N+5/2}$ needed for calculating (Div.-S4)$_y$,

$$\begin{aligned} -\left(\frac{9}{8}\frac{\delta_1 u}{\delta_1 x} - \frac{1}{8}\frac{\delta_3 u}{\delta_3 x} + \frac{\partial}{\partial z_{\mathrm{F}}} w\right) &= \frac{9}{8}\frac{\delta_1 v}{\delta_1 y} - \frac{1}{8}\frac{\delta_3 v}{\delta_3 y} \\ &= \frac{-v_{3/2} + 27v_{1/2} - 27v_{-1/2} + v_{-3/2}}{24\Delta y}. \end{aligned} \tag{A.36}$$

Using equations (A.12) and (A.13),

$$v_{-3/2} = 27v_{1/2} - 26v_{3/2} - 24\Delta y\left[\frac{9}{8}\frac{\delta_1 u}{\delta_1 x} - \frac{1}{8}\frac{\delta_3 u}{\delta_3 x} + \frac{\partial}{\partial z_{\mathrm{F}}} w\right]_0, \tag{A.37}$$

$$v_{N+5/2} = 27v_{N+1/2} - 26v_{N-1/2} - 24\Delta y\left[\frac{9}{8}\frac{\delta_1 u}{\delta_1 x} - \frac{1}{8}\frac{\delta_3 u}{\delta_3 x} + \frac{\partial}{\partial z_{\mathrm{F}}} w\right]_{N+1}. \tag{A.38}$$

Unfortunately, these conditions for v at $j = -3/2$ and $N + 5/2$ have not been found to be successful. For example, in simulating the fully developed laminar flow between walls, coupling with u velocities results in an instability through v velocity and does not allow the flow to stay laminar. Instead, from the condition that the fourth-order-accurate interpolated velocity v at walls is the velocity at the wall, i.e.,

$$\frac{-v_{-3/2} + 4v_{-1/2} + 4v_{3/2} - v_{5/2}}{6} = v_{1/2} + \mathcal{O}(\Delta y^4), \tag{A.39}$$

$$\frac{-v_{N+5/2} + 4v_{N+3/2} + 4v_{N-1/2} - v_{N-3/2}}{6} = v_{N+1/2} + \mathcal{O}(\Delta y^4). \tag{A.40}$$

Together with (A.12) and (A.13), the following conditions are obtained,

$$\begin{aligned}
v_{-3/2} &= -6v_{1/2} + 4v_{-1/2} + 4v_{3/2} - v_{5/2} \\
&= 2v_{1/2} - 2v_{5/2}, \qquad \text{(A.41)} \\
v_{N+5/2} &= -6v_{N+1/2} + 4v_{N+3/2} + 4v_{N-1/2} - v_{N-3/2} \\
&= 2v_{N+1/2} - 2v_{N-5/2}. \qquad \text{(A.42)}
\end{aligned}$$

To compute the skew-symmetric form of the nonlinear terms, i.e., ((Div-S4)+(Adv-S4))/2, one needs $v\frac{\delta_3 w}{\delta_3 y}$ and $\overline{v}^{(x)}\frac{\delta_3 u}{\delta_3 y}$ at $j = -1/2$ and $j = N + 3/2$. Since $\overline{v}^{(x)}\overline{u}^{(3y)}$ and $v\overline{w}^{(3y)}$ are obtained as in (A.19) and (A.20), we also have

$$\begin{aligned}
\frac{u_{1/2} + u_{-5/2}}{2} &= \overline{u}^{(3y)}_{-1/2}, \qquad \text{(A.43)} \\
\frac{u_{1/2} - u_{-5/2}}{3\Delta y} &= \frac{\delta_3 u}{\delta_3 y}_{-1/2}. \qquad \text{(A.44)}
\end{aligned}$$

Therefore

$$\begin{aligned}
\overline{v}^{(x)}\frac{\delta_3 u}{\delta_3 y}_{-1/2} &= \overline{v}^{(x)}\frac{2u_{1/2} - 2\overline{u}^{(3y)}_{-1/2}}{3\Delta y}, \qquad \text{(A.45)} \\
\overline{v}^{(x)}\frac{\delta_3 u}{\delta_3 y}_{N+3/2} &= \overline{v}^{(x)}\frac{-2u_{N+1/2} + 2\overline{u}^{(3y)}_{N+3/2}}{3\Delta y}. \qquad \text{(A.46)}
\end{aligned}$$

Similarly for w,

$$\begin{aligned}
v\frac{\delta_3 w}{\delta_3 y}_{-1/2} &= v\frac{2w_{1/2} - 2\overline{w}^{(3y)}_{-1/2}}{3\Delta y}, \qquad \text{(A.47)} \\
v\frac{\delta_3 w}{\delta_3 y}_{N+3/2} &= v\frac{-2w_{N+1/2} + 2\overline{w}^{(3y)}_{N+3/2}}{3\Delta y}. \qquad \text{(A.48)}
\end{aligned}$$

A.5 Helmholtz solver using discrete Fourier cosine transform

In this section the fast Helmholtz solver using the discrete Fourier cosine transform will be reviewed and the method for handling the issue regarding the higher-order scheme will be presented. For simplicity, assume the variables are already transferred into Fourier space in the z-direction, i.e.,

$p = p(x_i, y_j, k_z)$. The inverse discrete cosine transform along the x-direction is defined as

$$p(x_i, y_j, k_z) = \frac{2}{N} \sum_{k_x=0}^{N-1} \tilde{p}(k_x, y_j, k_z) \cos\left(\frac{\pi k(i + 1/2)}{N}\right). \tag{A.49}$$

The Poisson-pressure equation requiring solution is

$$\mathbf{DG}p(x_i, y_j, k_z) = f(x_i, y_j, k_z), \tag{A.50}$$

for some right-hand side $f(x_i, y_j, k_z)$.

A.5.1 Second-order-accurate scheme

The equation

$$\mathbf{DG}p = \frac{\delta_1}{\delta_1 x_i}\left(\frac{\delta_1 p}{\delta_1 x_i}\right), \tag{A.51}$$

is the discretization for the second-order-accurate scheme. Substituting (A.49) into the y-derivative in (A.50) gives

$$\begin{aligned} &\frac{2}{N} \sum_{k_x=0}^{N-1} \left[\frac{1}{\Delta x^2}\lambda_i + \frac{\delta_1}{\delta_1 y}\left(\frac{\delta_1}{\delta_1 y}\right) - k_z^2\right] \tilde{p}(k_x, y_j, k_z) \cos\left(a(i + \frac{1}{2})\right) \\ &= \frac{2}{N} \sum_{k_x=0}^{N-1} \tilde{f}(k_x, y_j, k_z) \cos\left(a(i + \frac{1}{2})\right), \end{aligned} \tag{A.52}$$

where $a = \pi k_x/N$ and

$$\begin{aligned} \lambda_i &= \frac{\cos\left(a(i + \frac{3}{2})\right) - 2\cos\left(a(i + \frac{1}{2})\right) + \cos\left(a(i - \frac{1}{2})\right)}{\cos\left(a(i + \frac{1}{2})\right)}, \\ &= 2\left(\cos(a) - 1\right). \end{aligned} \tag{A.53}$$

Simplifying and equating coefficients of corresponding cosines gives

$$\left[\frac{1}{\Delta x^2}\lambda_i + \frac{\delta_1}{\delta_1 y}\left(\frac{\delta_1}{\delta_1 y}\right) - k_z^2\right] \tilde{p} = \tilde{f}, \tag{A.54}$$

where $\tilde{f} = \tilde{f}(k_x, y_j, k_z)$, $\tilde{p} = \tilde{p}(k_x, y_j, k_z)$. This is the method whereby the tri-diagonal $\frac{\delta_1}{\delta_1 x}\left(\frac{\delta_1}{\delta_1 x}\right)$ elements of the operator $\mathbf{DG}$ are diagonalized. For the second-order scheme, the tri-diagonal matrix diagonalized by the discrete cosine transform has automatically the same structure of the tri-diagonal matrix that needs to be solved. But as pointed out earlier, for the higher-order scheme this is not the case.

A.5.2 Fourth-order-accurate scheme

Similarly with the second-order-accurate method, using

$$\mathbf{DG}p = \frac{\delta_1}{\delta_1 x_i}\left[\frac{9}{8}\frac{\delta_1}{\delta_1 x_i}\left(\frac{9}{8}\frac{\delta_1 p}{\delta_1 x_i} - \frac{1}{8}\frac{\delta_3 p}{\delta_3 x_i}\right) - \frac{1}{8}\frac{\delta_3}{\delta_3 p}\left(\frac{9}{8}\frac{\delta_1 p}{\delta_1 x_i} - \frac{1}{8}\frac{\delta_3 p}{\delta_3 x_i}\right)\right], \tag{A.55}$$

for the discretization, we obtain for the fourth-order case,

$$\frac{2}{N}\sum_{k_x=0}^{N-1}\left[\frac{1}{576\Delta x^2}\lambda_i + \frac{\delta^2}{\delta y^2} - k_z^2\right]\tilde{p}\cos(a(i+\frac{1}{2})) = \frac{2}{N}\sum_{k_x=0}^{N-1}\tilde{f}\cos(a(i+\frac{1}{2})), \tag{A.56}$$

where

$$\frac{\delta^2}{\delta y^2} = \frac{\delta_1}{\delta_1 y}\left[\frac{9}{8}\frac{\delta_1}{\delta_1 y}\left(\frac{9}{8}\frac{\delta_1}{\delta_1 y} - \frac{1}{8}\frac{\delta_3}{\delta_3 y}\right) - \frac{1}{8}\frac{\delta_3}{\delta_3 y}\left(\frac{9}{8}\frac{\delta_1}{\delta_1 y} - \frac{1}{8}\frac{\delta_3}{\delta_3 y}\right)\right], \tag{A.57}$$

$$\begin{aligned}
\lambda_i &= \Big[\cos(a(i+\frac{7}{2})) - 54\cos(a(i+\frac{5}{2})) + 783\cos(a(i+\frac{3}{2})) - 1460\cos(a(i+\frac{1}{2})) \\
&+ 783\cos(a(i-\frac{1}{2})) - 54\cos(a(i-\frac{3}{2})) + \cos(a(i-\frac{5}{2}))\Big] / \cos(a(i+\frac{1}{2})) \\
&= 2\left(\cos(3a) - 54\cos(2a) + 783\cos(a) - 730\right).
\end{aligned} \tag{A.58}$$

Simplifying to get the discrete Helmholtz equation as follows,

$$\left[\frac{1}{576\Delta x^2}\lambda_i + \frac{\delta^2}{\delta y^2} - k_z^2\right]\tilde{p} = \tilde{f}. \tag{A.59}$$

As in the second-order scheme, now the septa-diagonal matrix $\delta^2/\delta x^2$ elements of operator **DG** is diagonalized and the actual matrix that will be solved using this method is

$$\frac{1}{576\Delta y^2}\begin{pmatrix}
-677 & 729 & -53 & 1 & 0 & 0 & 0 \\
729 & -1459 & 783 & -54 & 1 & 0 & 0 \\
-53 & 783 & -1460 & 783 & -54 & 1 & 0 \\
1 & -54 & 783 & -1460 & 783 & -54 & 1 \\
0 & 1 & -54 & 783 & -1460 & 783 & -53 \\
0 & 0 & 1 & -54 & 783 & -1459 & 729 \\
0 & 0 & 0 & 1 & -53 & 729 & -677
\end{pmatrix}.$$

This is the one-dimensional, fourth-order finite difference matrix for $\delta^2/\delta y^2$ with seven grid points, when the data is even around the boundaries.

Appendix B

Parallelization; scaling performance

Scalability tests in the following sections show that the data transpose method scales reasonably well up to 64 cores. When the problem size gets bigger, the scalability is degraded but is still good. See Tables B.4 and B.6. This degrading comes from the communication-free subroutines. The computation is performed using the Millikan Cluster, where each node has two quad-core processors. Millikan consists of

- 7 Dell Poweredge 1950 nodes
- 8 Dell Poweredge R410 nodes
- Gigabit ethernet interconnect
- Rocks 5.2 Provisioning
- Maui/Torque scheduling and resource management.

B.1 Poisson-pressure solver

In solving the primitive-variable incompressible Navier-Stokes equation by a finite-difference method, there is a need to solve a three-dimensional Poisson equation for pressure at each time step. Owing to the numerical method discussed in §2.3, this reduces to a set of one-dimensional Helmholtz equations in the z-direction. This section describes two methods and their performance to solve the Poisson-pressure problem itself, which is typically the most expensive part of the numerical solution. As a test case, the computational domain is divided by y-z slices. A Fourier-transform is performed in the z-direction and a cosine transform in the y-direction. Then the problem reduces to $\mathbf{Ax} = \mathbf{b}$ at each grid point in the y-z plane. Two methods were used:

- Method 1: Solve $\mathbf{Ax} = \mathbf{b}$ using parallel matrix solver.

- Method 2: First transpose data and redistributed in x-z sliced domain and solve $\mathbf{Ax} = \mathbf{b}$ using serial matrix solver.

SCALAPACK is used in Method 1, and LAPACK in Method 2.

B.1.1 Observations

For example, when we discretized the domain by a fourth-order central difference scheme with the grid points shown in Table B.1, $\mathbf{A}$ is a 384×384 septa-diagonal matrix, $\mathbf{x}$ and $\mathbf{b}$ are vectors with 384 elements. $\mathbf{Ax} = \mathbf{b}$ needs to be solved 128×64 times and $\mathbf{A}$ is different each time.

Results are shown in Table B.2. Although the whole data transposition requires additional data communication (all-to-all), once the data is transposed, the speedup gained from running a matrix solver from LAPACK in a parallel fashion is much bigger than the loss from the all-to-all data transpose communication. Although solving a system of equations in SCALAPACK requires communication between neighboring processes only, the matrix solver is implemented in a way that all the processes are synchronized after each computation of $\mathbf{Ax} = \mathbf{b}$.

	N_x	N_y	N_z
Case 1	384	64	128
Case 2	1024	256	256

Table B.1. The number of grid points in each direction. Case 1: $\mathbf{A}$ is 384×384 matrix. $\mathbf{Ax} = \mathbf{b}$ has to be solved 128×64 times. Case 2: $\mathbf{A}$ is 1024×1024 matrix. $\mathbf{Ax} = \mathbf{b}$ has to be solved 256×256 times.

	# of process	method 1	method 2
Case 1	2	1.738971	0.560757
Case 1	4	1.676841	0.326388
Case 1	8	1.950304	0.182092
Case 1	16	29.781431	0.380158
Case 1	32	29.682436	0.305485
Case 1	64	60.344768	0.291269
Case 2	4		4.174672
Case 2	8		2.258038
Case 2	16		4.122218
Case 2	32		3.862215
Case 2	64		1.821601

Table B.2. Computational time required to solve $\mathbf{Ax} = \mathbf{b}$

B.2 Navier-Stokes solver

It has already been shown that, the current implementation of Scalapack (Method 1) is much slower than the data-transpose scheme (Method 2). Detailed profiles of the current three-dimensional Navier-Stokes solver with Method 2 are investigated in this section. The problem size is defined by the parameters shown in Table B.3. The time (in seconds) required at each subroutine at the slowest process are shown in Table B.4 for the case with LES-wall model, and in Table B.6 for the DNS case. Tables B.5 and B.7 show them in percentile.

	N_x	N_y	N_z
LES	384	64	128
DNS	256	256	256

Table B.3. Scaling test of Navier-Stokes solver, the number of grid points in each direction

B.2.1 LES case

The code scales reasonably well up to 64 processes, where speedup is 47.6. See Table B.4. It is observed from Table B.5 that the most time-consuming part is to get the nonlinear term in the governing equation (*get nonlinear term*), especially the subgrid-stress (*get Tijdxj*). Obviously, the fraction of the computational time required for data transpose increases as the number of processes increase, (*transpose data* in *Poisson solver*). However, this increase is not significant as a total over the range of the number of processors 1 to 64.

B.2.2 DNS case

The code scales reasonably well up to 16 processes, where speedup is 13.9, but its performance degrades when using more than 16 processes. See Table B.6. It seems that this is not due to the communication load between processes, because the time consumed in communication-oriented subroutines (*get neighboring data*, *Poisson solver*) did not increase much. The increase did occur in *get convective* and process independent basic operations, such as *get rhs* and *free memory*. This increase was rather attributed to the fact that the lower speck computer nodes in Millikan are involved in computation. Table B.8 shows how long the fastest process had to wait for the slowest process got its work done at each subroutines. 3.03s, 2.45s for 32 and 64 processes, respectively. They consist more than 50% of the total computational time. It should be noted, however, that even without this delay, the speedup is inferior to that of LES cases, 19.1 and 33.8 for 32 and 64 processes, respectively.

# of process	1	2	4	8	16	32	64
Navier-Stokes solver/3	49.0	26.4	11.4	5.77	3.01	2.25	1.03
get neighboring data	0.00	0.00	0.00	0.00	0.01	0.02	0.02
get nonlinear term	44.8	24.0	10.5	5.30	2.74	1.85	0.87
wall model	0.29	0.16	0.06	0.03	0.01	0.01	0.00
outflow	0.00	0.00	0.00	0.00	0.00	0.00	0.00
viscous term	0.40	0.23	0.10	0.05	0.03	0.03	0.01
free memory	0.05	0.04	0.01	0.01	0.01	0.07	0.02
get rhs	0.36	0.20	0.07	0.03	0.02	0.03	0.01
solve for vels	1.18	0.61	0.25	0.12	0.06	0.04	0.02
get rhs	0.28	0.16	0.06	0.03	0.02	0.04	0.03
solve for p	0.67	0.42	0.17	0.09	0.06	0.07	0.04
project	0.20	0.13	0.04	0.02	0.01	0.02	0.01
data update	0.53	0.31	0.10	0.05	0.03	0.04	0.01
get nonlinear term	44.8	24.0	10.5	5.30	2.74	1.85	0.87
get boundary data	0.00	0.00	0.00	0.00	0.00	0.00	0.00
interpolation	1.04	0.62	0.24	0.12	0.07	0.09	0.04
get convective	5.18	3.13	1.24	0.66	0.33	0.32	0.12
get Tijdxj	38.6	20.3	9.06	4.54	2.36	1.65	0.73
Poisson solver (e-1)	6.64	4.20	1.72	0.91	0.58	0.73	0.37
memory allocate (e-1)	0.00	0.00	0.00	0.00	0.00	0.00	0.00
arrange data (e-1)	0.32	0.18	0.06	0.03	0.02	0.02	0.00
cosine forward (e-1)	0.41	0.23	0.09	0.05	0.02	0.01	0.01
transpose data (e-1)	0.28	0.50	0.18	0.10	0.18	0.38	0.26
arrange data (e-1)	0.33	0.19	0.07	0.04	0.02	0.02	0.01
lapack in x (e-1)	4.14	2.08	0.98	0.48	0.24	0.13	0.07
arrange data (e-1)	0.29	0.18	0.05	0.03	0.02	0.01	0.00
transpose data (e-1)	0.18	0.48	0.18	0.10	0.08	0.23	0.25
cosine inverse (e-1)	0.34	0.18	0.07	0.04	0.02	0.01	0.00
arrange data (e-1)	0.27	0.17	0.05	0.04	0.01	0.01	0.00
free memory (e-1)	0.09	0.06	0.01	0.01	0.00	0.01	0.00

Table B.4. Computational time required (seconds) at each stage. LES $384 \times 128 \times 64$. The time spent by the slowest process

# of process	1	2	4	8	16	32	64
Navier-Stokes solver/3	100	100	100	100	100	100	100
get neighboring data	0.0	0.0	0.0	0.0	0.2	0.8	2.3
get nonlinear term	91.6	91.1	92.1	91.8	91.1	82.4	84.8
wall model	0.6	0.6	0.5	0.5	0.5	0.6	0.4
outflow	0.0	0.0	0.0	0.0	0.0	0.0	0.1
viscous term	0.8	0.9	0.9	0.9	0.9	1.5	1.0
free memory	0.1	0.1	0.1	0.2	0.2	3.1	0.2
get rhs	0.7	0.8	0.6	0.6	0.6	1.2	0.8
solve for vels	2.4	2.3	2.2	2.1	2.1	1.7	1.5
get rhs	0.6	0.6	0.5	0.6	0.7	1.8	3.1
solve for p	1.4	1.6	1.5	1.6	2.0	3.3	3.7
project	0.4	0.5	0.4	0.4	0.5	0.9	0.6
data update	1.1	1.2	0.9	0.9	1.0	2.0	1.2
get nonlinear term	100	100	100	100	100	100	100
get boundary data	0.0	0.0	0.0	0.0	0.0	0.0	0.1
interpolation	2.3	2.6	2.2	2.3	2.4	4.5	4.1
get convective	11.5	13.0	11.8	12.3	12.0	15.5	13.1
get Tijdxj	86.1	84.4	86.0	85.4	85.5	80.0	82.8
Poisson solver	100	100	100	100	100	100	100
memory allocate	0.0	0.0	0.0	0.0	0.0	0.1	0.1
arrange data	4.8	4.4	3.7	3.6	2.8	2.3	1.1
cosine forward	6.1	5.6	5.5	5.5	3.7	1.8	1.4
transpose data	4.1	11.8	10.3	10.9	30.5	52.7	69.0
arrange data	5.0	4.5	4.1	4.3	3.2	2.4	1.8
lapack in x	62.4	49.5	56.7	53.5	42.0	18.0	18.6
arrange data	4.4	4.2	2.8	3.3	2.7	1.1	0.5
transpose data	2.7	11.4	10.5	11.3	15.0	31.5	68.2
cosine inverse	5.1	4.2	4.3	4.2	2.9	1.3	1.1
arrange data	4.1	4.1	2.7	3.8	2.1	1.5	1.2
free memory	1.3	1.4	0.8	1.4	0.8	1.1	0.6

Table B.5. Computational time required (percentile) at each stage. LES $384 \times 128 \times 64$. The time spent by the slowest process

# of process	1	2	4	8	16	32	64
Navier-Stokes solver/3	53.8	29.9	11.2	7.15	3.86	5.84	4.04
get neighboring data	0.00	0.34	0.13	0.15	0.17	0.26	0.55
get nonlinear term	31.4	18.7	6.63	4.26	2.27	3.31	1.98
wall model	n/a	n/a	n/a	n/a	n/a	n/a	n/a
outflow	0.00	0.00	0.00	0.00	0.00	0.00	0.00
viscous term	2.04	1.15	0.55	0.40	0.17	0.24	0.12
free memory	0.23	0.17	0.05	0.05	0.03	0.46	0.29
get rhs	1.67	0.96	0.27	0.17	0.09	0.15	0.07
solve for vels	8.97	3.00	1.69	0.85	0.43	0.30	0.12
get rhs	1.35	0.76	0.25	0.20	0.15	0.40	0.49
solve for p	3.68	2.15	0.88	0.56	0.29	0.26	0.18
project	0.95	0.68	0.17	0.14	0.08	0.13	0.08
data update	2.81	1.63	0.39	0.29	0.16	0.24	0.12
get nonlinear term	31.4	18.7	6.63	4.26	2.27	3.31	1.98
get boundary data	0.01	0.01	0.00	0.01	0.01	0.01	0.01
interpolation	3.88	2.37	0.81	0.52	0.30	0.59	0.44
get convective	26.6	15.8	5.61	3.61	1.88	2.61	1.47
get Tijdxj	0.96	0.54	0.22	0.15	0.09	0.14	0.10
Poisson solver	3.68	2.15	0.88	0.56	0.29	0.26	0.18
memory allocate	0.00	0.00	0.00	0.00	0.00	0.00	0.00
arrange data	0.16	0.09	0.05	0.04	0.02	0.01	0.01
cosine forward	0.26	0.14	0.06	0.03	0.02	0.01	0.00
transpose data	0.13	0.24	0.07	0.07	0.04	0.07	0.07
arrange data	0.17	0.09	0.05	0.04	0.02	0.01	0.01
lapack in x	2.14	0.95	0.50	0.25	0.13	0.07	0.03
arrange data	0.22	0.13	0.02	0.02	0.01	0.02	0.01
transpose data	0.09	0.23	0.07	0.06	0.03	0.07	0.06
cosine inverse	0.22	0.11	0.05	0.03	0.01	0.01	0.00
arrange data	0.24	0.15	0.02	0.02	0.01	0.02	0.01
free memory	0.04	0.03	0.01	0.00	0.00	0.00	0.00

Table B.6. Computational time required (seconds) at each stage. DNS case 256^3. The time spent by the slowest process

# of process	1	2	4	8	16	32	64
Navier-Stokes solver/3	100	100	100	100	100	100	100
get neighboring data	0.0	1.1	1.2	2.1	4.3	4.5	13.7
get nonlinear term	58.4	62.6	59.4	59.5	58.7	56.7	49.1
wall model	n/a	n/a	n/a	n/a	n/a	n/a	n/a
outflow	0.0	0.0	0.0	0.0	0.1	0.1	0.1
viscous term	3.8	3.8	4.9	5.6	4.3	4.1	3.1
free memory	0.4	0.6	0.4	0.7	0.7	8.0	7.1
get rhs	3.1	3.2	2.5	2.4	2.4	2.6	1.8
solve for vels	16.7	10.0	15.2	11.8	11.1	5.2	2.9
get rhs	2.5	2.5	2.3	2.7	3.8	6.9	12.3
solve for p	6.8	7.2	7.9	7.8	7.4	4.5	4.4
project	1.8	2.3	1.6	2.0	2.2	2.3	2.1
data update	5.2	5.4	3.5	4.1	4.1	4.1	3.0
get nonlinear term	100	100	100	100	100	100	100
get boundary data	0.0	0.0	0.1	0.1	0.2	0.4	0.3
interpolation	12.3	12.7	12.1	12.1	13.4	17.5	22.1
get convective	84.6	84.4	84.5	84.4	82.3	78.0	72.9
get Tijdxj	3.1	2.9	3.3	3.4	4.1	4.0	4.8
Poisson solver	100	100	100	100	100	100	100
memory allocate	0.0	0.0	0.0	0.0	0.0	0.0	0.0
arrange data	4.5	4.4	5.2	7.0	6.9	5.1	3.6
cosine forward	7.0	6.4	6.3	5.8	5.8	5.7	2.1
transpose data	3.5	11.5	8.5	12.5	15.4	25.6	41.7
arrange data	4.5	4.3	5.3	7.0	7.2	5.5	3.3
lapack in x	58.4	44.4	57.0	45.1	44.1	27.1	19.5
arrange data	6.0	6.0	2.7	4.0	3.9	6.2	4.0
transpose data	2.5	10.6	8.0	11.1	11.3	28.0	33.8
cosine inverse	5.9	5.2	5.4	4.5	4.7	4.6	2.0
arrange data	6.6	7.0	2.8	3.7	3.4	6.9	3.2
free memory	1.1	1.3	0.7	1.0	0.7	1.4	1.6

Table B.7. Computational time required (percentile) at each stage. DNS case 256^3. The time spent by the slowest process

# of process	32	32	64	64
	slowest	fastest	slowest	fastest
Total waited time	n/a	3.03	n/a	2.45
get neighboring data	0.26	0.05	0.55	0.02
get nonlinear term	3.31	1.66	1.98	0.73
wall model	n/a	n/a	n/a	n/a
outflow	0.00	0.00	0.00	0.00
viscous term	0.24	0.10	0.12	0.04
free memory	0.46	0.05	0.29	0.02
get rhs	0.15	0.04	0.07	0.02
solve for vels	0.30	0.21	0.12	0.08
get rhs	0.40	0.34	0.49	0.45
solve for p	0.26	0.22	0.18	0.16
project	0.13	0.05	0.08	0.04
data update	0.24	0.06	0.12	0.03
get nonlinear term	3.31	1.66	1.98	0.73
get boundary data	0.01	0.01	0.01	0.00
interpolation	0.59	0.24	0.44	0.13
get convective	2.61	1.36	1.47	0.55
get Tijdxj	0.14	0.04	0.10	0.02

Table B.8. Computational time required (seconds) at each stage at the slowest process and the fastest process. DNS case 256^3

Bibliography

Abe, H., Kawamura, H. and Choi, H. 2004 Very large-scale structures and their effects on the wall shear-stress fluctuations in a turbulent channel flow up to $Re_\tau = 640$. *Journal of Fluids Engineering(Transactions of the ASME)* **126**, 835–843.

Akselvoll, K. and Moin, P. 1996 An efficient method for temporal integration of the Navier-Stokes equations in confined axisymmetric geometries. *Journal of Computational Physics* **125** (2), 454–463.

del Álamo, J.C. and Jiménez, J. 2003 Spectra of the very large anisotropic scales in turbulent channels. *Physics of Fluids* **15** (6), L41–L44.

Alfredsson, P.H. and Örlü, R. 2010 The diagnostic plot–a litmus test for wall bounded turbulence data. *European Journal of Mechanics-B/Fluids* **29** (6), 403–406.

Alfredsson, P.H., Segalini, A. and Örlü, R. 2011 A new scaling for the streamwise turbulence intensity in wall-bounded turbulent flows and what it tells us about the outer peak. *Physics of Fluids* **23**, 041702.

Anderson, A. and Meneveau, C. 2011 Dynamic roughness model for large-eddy simulation of turbulent flow over multiscale, fractal-like rough surfaces. *Journal of Fluid Mechanics* **679**, 288–314.

Araya, G., Castillo, L., Meneveau, C. and Jansen, K. 2011 A dynamic multi-scale approach for turbulent inflow boundary conditions in spatially developing flows . *Journal of Fluid Mechanics* **670**, 581–605.

Armfield, S. and Street, R. 1999 The fractional-step method for the Navier-Stokes equations on staggered grids - The accuracy of three variations. *Journal of Computational Physics* **153** (2), 660–665.

Boersma, B.J. 2011 A 6th order staggered compact finite difference method for the incompressible Navier-Stokes and scalar transport equations. *Journal of Computational Physics* **230**, 4940–4954.

Bradshaw, P. 1967 The turbulence structure of equilibrium boundary layers. *Journal of Fluid Mechanics* **29** (04), 625–645.

Brasseur, J.G. and Wei, T. 2010 Designing large-eddy simulation of the turbulent boundary layer to capture law-of-the-wall scaling. *Physics of Fluids* **22**, 021303.

Brown, D.L., Cortez, R. and Minion, M.L. 2001 Accurate projection methods for the incompressible Navier-Stokes equations. *Journal of Computational Physics* **168** (2), 464–499.

Cabot, W. and Moin, P. 2000 Approximate wall boundary conditions in the large-eddy simulation of high Reynolds number flow. *Flow, Turbulence and Combustion* **63** (1), 269–291.

Chin, C.C., Hutchins, N., Ooi, A.S.H. and Marusic, I. 2009 Use of direct numerical simulation (DNS) data to investigate spatial resolution issues in measurements of wall-bounded turbulence. *Measurement Science & Technology* **20** (11), 115401.

Chorin, A.J. 1968 Numerical solution of the Navier-Stokes equations. *Mathematics of Computation* **22** (104), 745–762.

Chow, F.K. and Moin, P. 2003 A further study of numerical errors in large-eddy simulations. *Journal of Computational Physics* **184** (2), 366–380.

Chung, D. and McKeon, B.J. 2010 Large-eddy simulation of large-scale structures in long chanel flow. *Journal of Fluid Mechanics* **661**, 341–364.

Chung, D. and Pullin, D.I. 2009 Large-eddy simulation and wall-modeling of turbulent channel flow. *Journal of Fluid Mechanics* **631**, 281–309.

Clauser, F.H. 1956 The turbulent boundary layer. *Advances in Applied Mechanics* **4** (1).

Coles, D. 1956 The law of the wake in the turbulent boundary layer. *Journal of Fluid Mechanics* **1** (2), 191–226.

DeGraaff, D.B. and Eaton, J.K. 2000 Reynolds-number scaling of the flat-plate turbulent boundary layer. *Journal of Fluid Mechanics* **422** (1), 319–346.

Erm, L.P. and Joubert, P.N. 1991 Low Reynolds number turbulent boundary layers. *Journal of Fluid Mechanics* **230**, 1–44.

Fasel, H. 1976 Investigation of the stability of boundary layers by a finite-difference model of the Navier-Stokes equations. *Journal of Fluid Mechanics* **78** (2), 355–383.

Ferrante, A. and Elghobashi, S.E. 2004 A robust method for generating inflow conditions for direct simulations of spatially-developing turbulent boundary layers. *Journal of Computational Physics* **198** (1), 372–387.

Ferrante, A. and Elghobashi, S.E. 2005 Reynolds number effect on drag reduction in a microbubble-laden spatially developing turbulent boundary layer. *Journal of Fluid Mechanics* **543**, 93–106.

Ganapathisubramani, B., Longmire, E.K. and Marusic, I. 2003 Characteristics of vortex packets in turbulent boundary layers. *Journal of Fluid Mechanics* **478**, 35–46.

Gottlieb, D. and Shu, C.W. 1997 On the Gibbs phenomenon and its resolution. *SIAM review* **39** (4), 644–668.

Gresho, P.M. and Sani, R.L. 1987 On pressure boundary conditions for the incompressible Navier-Stokes equations. *International Journal for Numerical Methods in Fluids* **7** (10), 1111–1145.

Gullbrand, J. and Chow, F.K. 2003 The effect of numerical errors and turbulence models in large-eddy simulations of channel flow, with and without explicit filtering. *Journal of Fluid Mechanics* **495** (1), 323–341.

Harun, Z., Monty, J.P. and Marusic, I. 2010 Constant adverse pressure gradient turbulent boundary layers. In *17th Australian Fluid Mechanics Conference, Auckland, New Zealand*.

Head, M.R. and Bandyopadhyay, P. 1981 New aspects of turbulent boundary-layer structure. *Journal of Fluid Mechanics* **107**, 297–338.

Henkes, R., Skote, M. and Henningson, D.S. 1997 Application of turbulence models to equilibrium boundary layers under adverse pressure gradient. In *11th Symposium on Turbulent Shear Flows, Grenoble, France*.

Henniger, R., Obrist, D. and Kleiser, L. 2010 High-order accurate solution of the incompressible Navier-Stokes equations on massively parallel computers. *Journal of Computational Physics* **229** (10), 3543–3572.

Hutchins, N. and Marusic, I. 2007a Evidence of very long meandering features in the logarithmic region of turbulent boundary layers. *Journal of Fluid Mechanics* **579**, 1–28.

Hutchins, N. and Marusic, I. 2007b Large-scale influences in near-wall turbulence. *Philosophical Transactions of the Royal Society A: Mathematical, Physical and Engineering Sciences* **365** (1852), 647–664.

Hutchins, N., Nickels, T.B., Marusic, I. and Chong, M.S. 2009 Hot-wire spatial resolution issues in wall-bounded turbulence. *Journal of Fluid Mechanics* **635**, 103–136.

Inoue, M. and Pullin, D.I. 2011 Large-eddy simulation of the zero pressure gradient turbulent boundary layer up to $Re_\theta = O(10^{12})$. *Journal of Fluid Mechanics* **686**, 507–533.

Jewkes, J.W., Chung, Y.M. and Carpenter, P.W. 2011 Modification to a turbulent inflow generation method for boundary-layer flows. *AIAA Journal* **49** (1), 247–250.

Jiménez, J. 2003 Computing high-Reynolds-number turbulence: will simulations ever replace experiments? *Journal of Turbulence* **4** (1), 022.

Jones, M.B., Marusic, I. and Perry, AE 2001 Evolution and structure of sink-flow turbulent boundary layers. *Journal of Fluid Mechanics* **428**, 1–27.

Keating, A., Piomelli, U., Balaras, E. and Kaltenbach, H.J. 2004 A priori and a posteriori tests of inflow conditions for large-eddy simulation. *Physics of Fluids* **16** (12), 4696–4712.

Kim, J. and Moin, P. 1985 Application of a fractional-step method to incompressible Navier-Stokes equations. *Journal of Computational Physics* **59** (2), 308–323.

Kim, K.C. and Adrian, R.J. 1999 Very large-scale motion in the outer layer. *Physics of Fluids* **11**, 417–422.

Klebanoff, P.S. 1954 Characteristics of turbulence in a boundary layer with zero pressure gradient. *NACA TN 3178* .

Knikker, R. 2009 Study of a staggered fourth-order compact scheme for unsteady incompressible viscous flows. *International journal for numerical methods in fluids* **59** (10), 1063–1092.

Lee, J., Lee, J.H., Lee, J.H. and Sung, H.J. 2010 Coherent structures in turbulent boundary layers with adverse pressure gradients. *Journal of Turbulence* **11** (28), 1–20.

Lee, J.H. and Sung, H.J. 2008 Effects of an adverse pressure gradient on a turbulent boundary layer. *International Journal of Heat and Fluid Flow* **29** (3), 568–578.

Lee, J.H. and Sung, H.J. 2011 Direct numerical simulation of a turbulent boundary layer up to $Re_\theta = 2500$). *International Journal of Heat and Fluid Flow* **32** (1), 1–10.

Lesieur, M. and Metais, O. 1996 New trends in large-eddy simulations of turbulence. *Annual Review of Fluid Mechanics* **28**, 45–82.

Liu, K. and Pletcher, R.H. 2006 Inflow conditions for the large-eddy simulation of turbulent boundary layers: A dynamic recycling procedure. *Journal of Computational Physics* **219** (1), 1–6.

Lu, H. and Porté-Agel, F. 2010 A modulated gradient model for large-eddy simulation: Application to a neutral atmospheric boundary layer. *Physics of fluids* **22** (1), 015109.

Luchini, P. and Quadrio, M. 2006 A low-cost parallel implementation of direct numerical simulation of wall turbulence. *Journal of Computational Physics* **211** (2), 551–571.

Lund, T.S., Wu, X. and Squires, K.D. 1998 Generation of turbulent inflow data for spatially-developing boundary layer simulations. *Journal of Computational Physics* **140** (2), 233–258.

Lundgren, T.S. 1982 Strained spiral vortex model for turbulent fine structure. *Physics of Fluids* **25**, 2193–2203.

Marusic, I. and Kunkel, G.J. 2003 Streamwise turbulence intensity formulation for flat-plate boundary layers. *Physics of Fluids* **15**, 2461–2464.

Marusic, I., Mathis, R. and Hutchins, N. 2010a Predictive model for wall-bounded turbulent flow. *Science* **329** (5988), 193–196.

Marusic, I., McKeon, B.J., Monkewitz, P.A., Nagib, H.M., Smits, A.J. and Sreenivasan, K.R. 2010b Wall-bounded turbulent flows at high Reynolds numbers: Recent advances and key issues. *Physics of Fluids* **22**, 065103.

Marusic, I. and Perry, A.E. 1995 A wall-wake model for the turbulence structure of boundary layers. Part 2. Further experimental support. *Journal of Fluid Mechanics* **298**, 389–407.

Marusic, I., Uddin, A.K.M. and Perry, A.E. 1997 Similarity law for the streamwise turbulence intensity in zero-pressure-gradient turbulent boundary layers. *Physics of Fluids* **9**, 3718.

Mathis, R., Hutchins, N. and Marusic, I. 2009 Large-scale amplitude modulation of the small-scale structures in turbulent boundary layers. *Journal of Fluid Mechanics* **628**, 311–337.

Mathis, R., Hutchins, N. and Marusic, I. 2011 A predictive inner-outer model for streamwise turbulence statistics in wall-bounded flows. *Journal of Fluid Mechanics* **681** (1), 537–566.

McKeon, B.J. and Sharma, A.S. 2010 A critical-layer framework for turbulent pipe flow. *Journal of Fluid Mechanics* **658**, 336–382.

Mellor, G.L. and Gibson, D.M. 1966 Equilibrium turbulent boundary layers. *Journal of Fluid Mechanics* **24** (2), 225–253.

Meneveau, C. and Katz, J. 2000 Scale-invariance and turbulence models for large-eddy simulation. *Annual Review of Fluid Mechanics* **32**, 1–32.

Metzger, M.M. and Klewicki, J.C. 2001 A comparative study of near-wall turbulence in high and low Reynolds number boundary layers. *Physics of Fluids* **13**, 692–701.

Metzger, M., McKeon, B.J. and Holmes, H. 2007 The near-neutral atmospheric surface layer: turbulence and non-stationarity. *Philosophical Transactions of the Royal Society A: Mathematical, Physical and Engineering Sciences* **365** (1852), 859–876.

Misra, A. and Pullin, D.I. 1997 A vortex-based subgrid stress model for large-eddy simulation. *Physics of Fluids* **9**, 2443–2454.

Monkewitz, P.A., Chauhan, K.A. and Nagib, H.M. 2007 Self-consistent high-Reynolds-number asymptotics for zero-pressure-gradient turbulent boundary layers. *Physics of Fluids* **19**, 115101.

Monty, J.P., Harun, Z. and Marusic, I. 2011 A parametric study of adverse pressure gradient turbulent boundary layers. *International Journal of Heat and Fluid Flow* **32** (3), 575–585.

Morinishi, Y., Lund, T.S., Vasilyev, O.V. and Moin, P. 1998 Fully conservative higher order finite difference schemes for incompressible flow. *Journal of Computational Physics* **143** (1), 90–124.

Morrison, J.F., McKeon, B.J., Jiang, W. and Smits, A.J. 2004 Scaling of the streamwise velocity component in turbulent pipe flow. *Journal of Fluid Mechanics* **508**, 99–131.

Na, Y. and Moin, P. 1998 Direct numerical simulation of a separated turbulent boundary layer. *Journal of Fluid Mechanics* **374**, 379–405.

Nagano, Y., Tsuji, T. and Houra, T. 1998 Structure of turbulent boundary layer subjected to adverse pressure gradient. *International Journal of Heat and Fluid Flow* **19** (5), 563–572.

Nagib, H.M., Chauhan, K.A. and Monkewitz, P.A. 2007 Approach to an asymptotic state for zero pressure gradient turbulent boundary layers. *Philosophical Transactions of the Royal Society A: Mathematical, Physical and Engineering Sciences* **365** (1852), 755.

Nickels, TB 2004 Inner scaling for wall-bounded flows subject to large pressure gradients. *Journal of Fluid Mechanics* **521** (1), 217–239.

Nickels, T.B., Marusic, I., Hafez, S., Hutchins, N. and Chong, M.S. 2007 Some predictions of the attached eddy model for a high Reynolds number boundary layer. *Philosophical Transactions of the Royal Society A: Mathematical, Physical and Engineering Sciences* **365** (1852), 807–822.

Nordström, J., Nordin, N. and Henningson, D. 1999 The fringe region technique and the fourier method used in the direct numerical simulation of spatially evolving viscous flows. *SIAM Journal on Scientific Computing* **20** (4), 1365–1393.

O'Gorman, P.A. and Pullin, D.I. 2003 The velocity-scalar cross spectrum of stretched spiral vortices. *Physics of Fluids* **15**, 280–291.

Österlund, J.M. 1999 Experimental studies of zero pressure-gradient turbulent boundary layer flow. PhD thesis, KTH, Mechanics.

Oweis, G.F., Winkel, E.S., Cutbrith, J.M., Ceccio, S.L., Perlin, M. and Dowling, D.R. 2010 The mean velocity profile of a smooth-flat-plate turbulent boundary layer at high Reynolds number. *Journal of Fluid Mechanics* **665**, 357–381.

Perot, J.B. 1993 An analysis of the fractional step method. *Journal of Computational Physics* **108** (1), 51–58.

Perry, A.E. and Chong, M.S. 1982 On the mechanism of wall turbulence. *Journal of Fluid Mechanics* **119**, 173–217.

Perry, A.E. and Marusic, I. 1995 A wall-wake model for the turbulence structure of boundary layers. Part 1. Extension of the attached eddy hypothesis. *Journal of Fluid Mechanics* **298**, 361–388.

Perry, A.E., Marusic, I. and Jones, M.B. 2002 On the streamwise evolution of turbulent boundary layers in arbitrary pressure gradients. *Journal of Fluid Mechanics* **461**, 61–91.

Perry, A.E., Marusic, I. and Li, J.D. 1994 Wall turbulence closure based on classical similarity laws and the attached eddy hypothesis. *Physics of Fluids* **6** (2), 1024–1035.

Piomelli, U. 2008 Wall-layer models for large-eddy simulations. *Progress in Aerospace Sciences* **44**, 437–446.

Piomelli, U. and Balaras, E. 2002 Wall-layer models for large-eddy simulations. *Annual Review of Fluid Mechanics* **34** (1), 349–374.

Pope, S.B. 2000 *Turbulent flows*. Cambridge University Press.

Pope, S.B. 2004 Ten questions concerning the large-eddy simulation of turbulent flows. *New Journal of Physics* **6**, 35.

Porté-Agel, F., Meneveau, C. and Parlange, M.C. 2000 A scale-dependent dynamic model for large-eddy simulation: application to a neutral atmospheric boundary layer. *Journal of Fluid Mechanics* **415**, 261–284.

Pullin, D.I. and Lundgren, T.S. 2001 Axial motion and scalar transport in stretched spiral vortices. *Physics of Fluids* **13**, 2553–2563.

Pullin, D. I. 2000 A vortex-based model for the subgrid flux of a passive scalar. *Physics of Fluids* **12**, 2311–2319.

Robinson, S.K. 1991 Coherent motions in the turbulent boundary layer. *Annual Review of Fluid Mechanics* **23**, 601–639.

Sagaut, P. 2006 *Large eddy simulation for incompressible flows: an introduction*. Springer Verlag.

Sani, R.L., Shen, J., Pironneau, O. and Gresho, P.M. 2006 Pressure boundary condition for the time-dependent incompressible Navier-Stokes equations. *International Journal for Numerical Methods in Fluids* **50** (6), 673–682.

Schlatter, P., Li, Q., Brethouwer, G., Johansson, A.V. and Henningson, D.S. 2010 Simulations of spatially evolving turbulent boundary layers up to $Re_\theta = 4300$. *International Journal of Heat and Fluid Flow* **31** (3), 251–261.

Schlatter, P. and Örlü, R. 2010 Assessment of direct numerical simulation data of turbulent boundary layers. *Journal of Fluid Mechanics* **659**, 116–126.

Schlatter, P., Örlü, R., Li, Q., Brethouwer, G., Fransson, J.H.M., Johansson, A.V., Alfredsson, P.H. and Henningson, D.S. 2009 Turbulent boundary layers up to $Re_\theta = 2500$ studied through simulation and experiment. *Physics of Fluids* **21**, 051702.

Schofield, W.H. 1981 Equilibrium boundary layers in moderate to strong adverse pressure gradients. *Journal of Fluid Mechanics* **113**, 91–122.

Simens, M.P. 2008 The study and control of wall-bounded flows. PhD thesis, Aeronautics, Universidad Politécnica, Madrid, Spain, http://oa.upm.es/1047.

Simens, M.P., Jiménez, J., Hoyas, S. and Mizuno, Y. 2009 A high-resolution code for turbulent boundary layers. *Journal of Computational Physics* **228** (11), 4218–4231.

Skåre, P.E. and Krogstad, P. 1994 A turbulent equilibrium boundary layer near separation. *Journal of Fluid Mechanics* **272** (1), 319–348.

Skote, M. and Henningson, D.S. 2002 Direct numerical simulation of a separated turbulent boundary layer. *Journal of Fluid Mechanics* **471**, 107–136.

Skote, M., Henningson, D.S. and Henkes, R.A.W.M. 1998 Direct numerical simulation of self-similar turbulent boundary layers in adverse pressure gradients. *Flow, Turbulence and Combustion* **60** (1), 47–85.

Smits, A.J., Monty, J., Hultmark, M., Bailey, S.C.C., Hutchins, N. and Marusic, I. 2011 Spatial resolution correction for wall-bounded turbulence measurements. *Journal of Fluid Mechanics* **676** (1), 41–53.

Spalart, P.R. 1988 Direct simulation of a turbulent boundary layer up to $Re_\theta = 1410$. *Journal of Fluid Mechanics* **187**, 61–98.

Spalart, P.R., Moser, R.D. and Rogers, M.M. 1991 Spectral methods for the Navier-Stokes equations with one infinite and two periodic directions. *Journal of Computational Physics* **96** (2), 297–324.

Strikwerda, J.C. 1997 High-order-accurate schemes for incompressible viscous flow. *International Journal for Numerical Methods in Fluids* **24** (7), 715–734.

Templeton, J.A., Medic, G. and Kalitzin, G. 2005 An eddy-viscosity based near-wall treatment for coarse grid large-eddy simulation. *Physics of fluids* **17**, 105101.

Templeton, J.A., Wang, M. and Moin, P. 2008 A predictive wall model for large-eddy simulation based on optimal control techniques. *Physics of fluids* **20**, 065104.

Tomkins, C.D. and Adrian, R.J. 2003 Spanwise structure and scale growth in turbulent boundary layers. *Journal of Fluid Mechanics* **490**, 37–74.

Townsend, A.A. 1976 *The structure of turbulent shear flow*, 2nd edition. Cambridge University Press.

Voelkl, T., Pullin, D.I. and Chan, D.C. 2000 A physical-space version of the stretched-vortex subgrid-stress model for large-eddy simulation. *Physics of Fluids* **12**, 1810–1825.

Wang, M. and Moin, P. 2002 Dynamic wall modeling for large-eddy simulation of complex turbulent flows. *Physics of Fluids* **14**, 2043–2051.

Winkel, E.S., Cutbirth, J.M., Ceccio, S.L., Perlin, M. and Dowling, D.R. 2012 Turbulence profiles from a smooth flat-plate turbulent boundary layer at high Reynolds number. *Experimental Thermal and Fluid Science* **40**, 140.

Wu, X. and Moin, P. 2009 Direct numerical simulation of turbulence in a nominally zero-pressure-gradient flat-plate boundary layer. *Journal of Fluid Mechanics* **630**, 5–41.